ABSTRACT

Title of Thesis:	SCALE MODELING OF THE TRANSIENT BEHAVIOR OF HEAT FLUX IN ENCLOSURE FIRES
	Peter Surendran Veloo, Master of Science, 2006
Directed By:	John L. Bryan Chair Professor James G. Quintiere Department of Fire Protection Engineering

A new scaling technique based on the hypothesis that flows in a compartment fire are buoyancy driven was introduced by Quintiere [4]. Based on this hypothesis, scaling relations for convective and radiative heat transfer within compartment fires is presented. A technique to measure and differentiate convective and radiative heat flux in compartment fires is presented which utilizes a newly developed metal plate sensor and Gardon heat flux gauge. Experiments conducted to test the scaling hypotheses were conducted at two scales. Wood cribs were used to model a fuel load. The repeatability of wood crib fires has been demonstrated. Experimental results indicate that radiation heat flux scales according to the thermally thick emissivity criteria. Convective heat flux was demonstrated to scale with advected enthalpy. The convective heat transfer coefficient has been correlated against temperature rise within the compartment for both the before and after extinction cases.

SCALE MODELING OF THE TRANSIENT BEHAVIOR OF HEAT FLUX IN ENCLOSURE FIRES

By

Peter Surendran Veloo

Thesis submitted to the Faculty of the Graduate School of the
University of Maryland, College Park, in partial fulfillment
of the requirements for the degree of
Master of Science
2006

Advisory Committee:
Professor James G. Quintiere, Chair
Professor Andre Marshall
Professor Peter Sunderland

To my mother, father and brother.

Acknowledgements

I would like to thank the National Science Foundation for their financial support of this research. The completion of this thesis would not have been possible without the guidance of my supervisor, mentor and friend Dr. James Quintiere. I am also greatly indebted to the support and constant encouragement I received from the Fire Protection Engineering faculty and staff. I would especially like to thank my committee members Dr. Peter Sunderland and Dr. Andre Marshall.

I would also like to thank my fellow graduate students and colleagues at the Potomac Lab who were always willing to lend their support to my experimental and laboratory work. None of the experiments in this thesis could have been successfully completed without their help. I am especially grateful for the guidance and mentoring I received from Jonathan Perricone. I am also grateful to Yunyong Utiskul (Pock) who was always willing to lend me a hand throughout my time at Maryland. I would also like to thank Ming Wang, Joe Panagiotou, Kyle Lehman and Tensei Mizukami for their support and help during the various stages of my research.

Finally I would like to thank my parents whose support and encouragement made it possible for me to pursue my graduate studies at Maryland.

Table of Contents

List of Tables

List of Figures

Nomenclature

A	Area
A_o	Compartment Vent Area
A_s	Surface Area of Crib
A_{sl}	Surface Area of Smoke Layer
A_w	Surface Area of Compartment Walls
b	Wood Crib Stick Thickness
C	Wood Species Burning Rate Constant
$C.V.$	Control Volume
$C.S.$	Control Volume Surface Area
c_p	Specific Heat
D	Compartment Depth
d	Wood Crib Stick Length
F	View Factor
g	Gravity
Gr	Grashof Number
H	Wood Crib Height
$\Delta H_c, \Delta h_c$	Heat of Combustion
h	Compartment Vent Height
h_c	Convective Heat Transfer Coefficient
$h_{c,plate}$	Metal Plate Sensor Calibration Convective Heat Transfer Coefficient
h^*	Dimensionless Convective Heat Transfer Coefficient
h_k	Metal Plate Sensor Conductive Heat Transfer Coefficient
h_{eff}	Combined Convective, Radiative and Conductive Heat Transfer Coefficients – Calibration
$h_{eff,fire}$	Combined Convective, Radiative and Conductive Heat Transfer Coefficients – Compartment Fire
$h_{fire,c}$	Compartment Wall Convective Heat Transfer Coefficient
k_w	Compartment Wall Material Conductivity
k_{air}	Conductivity Air
L	Metal Plate Sensor Calibration Mount Length
L_e	Mean Beam Length
l	Characteristic Length – Compartment Height
$\dot{m}$	Mass Flow Rate
$\dot{m}_f$	Mass Loss Rate / Burning Rate of Wood Crib
N	Number of Stick Layers in Wood Crib
n	Number of Sticks per Layer in Wood Crib
$\overline{n}$	Unit Normal

Nu	Nusselt Number
P	Porosity
Pr	Prandtl Number
p	Pressure
Q_{fire}	Fire Power
Q_{inc}	Incident Heat Flux
Q_m	Metal Plate Sensor Measured Heat Flux
Q_{crr}	Metal Plate Sensor Measured Heat Flux Corrected for Time Response
$Q*$	Dimensionless Fire Power, Zukoski Number
$\dot{q}_{losses}$	Total Heat Flux Losses from Compartment
$\dot{q}_o$	Heat Loss through Compartment Vent
$\dot{q}_c$	Convective Heat Flux
$\dot{q}_r$	Radiative Heat Flux
$\dot{q}_w$	Total Heat Loss through Compartment Walls
$\dot{q}_{w,r}$	Net Radiative Flux to Compartment Wall
$\dot{q}_{w,c}$	Net Convective Flux to Compartment Wall
$\dot{q}_{w,k}$	Net Radiative conductive flux through Compartment Wall
$\dot{q}_{cond}$	Conductive Losses from Metal Plate Sensor
$\dot{q}_{fire,r}$	Total Radiative Flux from Fire
$\dot{q}_{fire,c}$	Total Conductive Flux from Fire
$\dot{q}_{HFG}$	Heat Flux Gauge measured Heat Flux
$\dot{q}_{inc,r}$	Incident Panel Radiation during Metal Plate Sensor Calibration
$\dot{q}_{inc,fire}$	Incident Fire Heat Flux
$\dot{q}''$	Heat Flux per Unit Area
$\dot{q}''_{inc}$	Incident Heat Flux per Unit Area
$\dot{q}''_m$	Metal Plate Sensor Measured Heat Flux per Unit Area
$\dot{q}''_{m,crr}$	Metal Plate Sensor Measured Heat Flux Corrected for Time Response
Re	Reynolds Number
R_r	Effective Radiative Thermal Resistance
R_k	Effective Conductive Thermal Resistance
R_c	Effective Convective Thermal Resistance
r	Sensor Location Parameter
S	Control Volume Surface Area
s	Wood Crib Stick Spacing
T	Compartment Gas Temperature
T_w	Wall Temperature
T_{sl}	Smoke Layer Temperature

T_∞	Ambient or Room Temperature
T_{ss}	Steady State Temperature
T_m	Temperature Metal Plate Sensor
T_d	Vent Temperature
t	Time
$\widetilde{t}$	Characteristic Time
$\hat{t}$	Dimensionless Time
t_r	Time Response
$t_{r,m}$	Measured Time Response
Δt	Sampling Period
u	Flow Velocity
$\widetilde{u}$	Characteristic Velocity
$\hat{u}$	Dimensionless Velocity
u_a	Flow Velocity through Compartment Vent
V	Volume
W	Compartment Width
x	Linear Distance
Y_i	Compartment Species
y_i	Species Yield

Greek

α_w	Thermal Diffusivity Wall Material
α_m	Absorptivity Metal Plate Sensor
β	Volumetric Thermal Expansion Coefficient
μ	Dynamic Viscosity
υ	Kinematic Viscosity
Π_i, π_i	Dimensionless Pi Group
σ	Stephan-Boltzmann Constant
ε	Emissivity
ε_{sl}	Emissivity of Smoke Layer
ε_w	Compartment Wall Material Emissivity
ε_{HFG}	Heat Flux Gauge Emissivity
ρ	Density
ρ_∞	Ambient Density
Γ	Shear Stress
τ	Dimensionless Time
δ	Thickness
δ_w	Wall Material Thickness
δ_t	Thermal Penetration Depth

1. INTRODUCTION

From its use by the Wright brothers to model and test designs for their flying machines, scale modeling has long been an important tool in engineering design and analysis. To date scale modeling can be found commonly utilized in the testing of prototype aircraft, automobiles and structures. Scale modeling is especially appealing in its application to fire protection engineering due to the cost and space restrictions associated with laboratory based testing of full scale structures. There are a number of techniques currently used to scaling the fire problem including pressure modeling, Froude modeling and analog modeling. In pressure modeling π groups including the Reynolds number are preserved by varying the pressure of the ambient at each scale [1]. Froude modeling on the other hand is conducted in ambient conditions with the Froude number being the primary group preserved [2]. Analog modeling simulates the flow field through employing the use of different fluids to simulate buoyancy effects.

This thesis presents a novel technique of scaling the transient behavior of compartment fires through scaling time with flow time and velocity with flow velocity. The motivation in deriving this new technique to scale compartment fires is the deficiency in current scaling techniques to scale the transient behavior of compartment fire dynamics. This study is the second part of ongoing research using this novel scaling methodology which was started by Jonathan Perricone [3]. Perricone presented a compelling argument for the viability of this scaling methodology by demonstrating its ability to scale the transient behavior of the burning rate of a designed fuel load, vent and compartment temperatures and species concentrations in compartment fires. The focus of ongoing work using this scaling methodology has been on scaling the transient response of structures within compartment fires.

1.1 Objectives

Prior work conducted by Perricone [3], did not conclusively study how heat flux within the compartment fires was scaling. The objective of this study is to extend Perricone's work by investigating how heat flux has been scaled using the current scaling methodology. Specifically, data needs to be collected on the convective, radiative and conductive heat transfer within enclosure fires.

1.2 Thesis Outline

There are six chapters in this thesis. Chapter 2 presents the scaling theory including a complete derivation of the dimensionless π groups from the governing equations. Theory is also present on the scaling of wood cribs which were used as the fuel load. Chapter 3 introduces a novel metal plate sensor which will be used with a Gardon heat flux gauge and thermocouple to elucidate information about the convective and radiative heat fluxes in the compartment fires. A comprehensive theory of these metal plate sensors is presented along with their calibration procedure and results. In chapter 4 the experimental design and methodology is presented. The experimental design procedure includes the compartment wall material and fuel load design. Sensor placement is also presented along with the ignition methodology for the wood cribs. Chapter 5 presents the results, analysis and discussion of the results obtained from the experiments. The final chapter provides a conclusion to this study.

2. THEORY

Chapter 2 presents the theory underlying the scaling methodology used in this study. First, the characteristic velocity, characteristic time and π groups are derived. From these π groups the scaling relationships for convection, radiation and conduction within the compartment are derived. Finally the scaling theory is applied to wood cribs which are used to model a fuel load within an enclosure.

There are three methods generally adopted for the derivation of the dimensionless π groups necessary to perform the similitude scaling of a system [4]. The first is the Buckingham Pi theorem. The second involves deriving the complete partial differential governing equations pertaining to a system and making them dimensionless. The third technique identifies the governing physics of the problem in its simplest form. These simplified governing partial differential equations are then made dimensionless. The latter technique has been adopted in this chapter to derive the π groups necessary to scale compartment fires.

Quintiere [4] outlines the development of the complete set of π groups necessary for the scaling of compartment fires using this technique and should be referred as a comprehensive resource. Chapter 2 expands on this outline by providing a complete derivation of the π groups used in this study. A complete list of all notation used in this and all following chapters is listed in the nomenclature.

2.1 Dimensionless Groups from Conservation Equations

Consider a control volume located in the fluid flow field of a compartment fire, as shown in Fig 2.1.

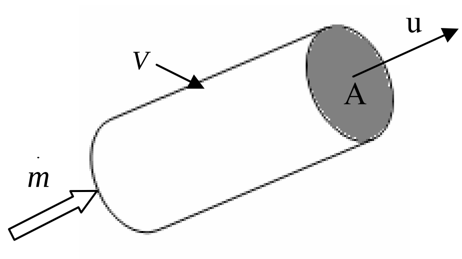

Figure 2.1: Control Volume for Conservation of Mass

The governing equation for the conservation of mass is derived from the above control volume. The integral expression for conservation of mass within the control volume is [4]:

$$\int_{C.S.} \rho(\bar{u} \cdot \bar{n})dA + \frac{d}{dt}\int_{C.V.} \rho dV = 0 \tag{2.1}$$

If the flow within the control volume is assumed to be steady, incompressible and one-dimensional the above governing equation for conservation of mass reduces to:

$$\dot{m} = \rho u A \tag{2.2}$$

A similar control volume in the fluid flow field is used to derive the governing equation for conservation of momentum, Fig. 2.2.

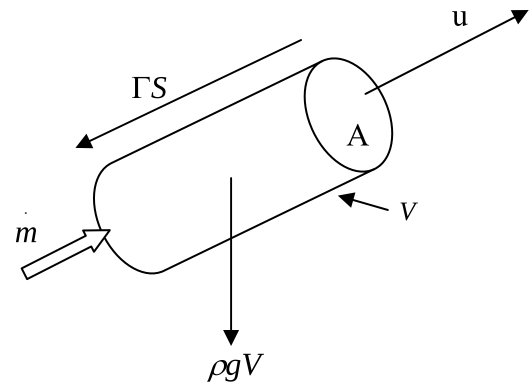

Figure 2.2: Control Volume for Conservation of Momentum

If an approximate form of the one-dimensional momentum equation in the vertical direction is considered the governing equation for momentum is [4]:

$$\rho V \frac{du}{dt} + \dot{m}u \approx (\rho_\infty - \rho) g V + pA + \Gamma S \qquad (2.3)$$

Eq. 2.3 describes the relationship between the unsteady momentum and momentum advection to the buoyancy, pressure and shear forces respectively.

Finally, for the derivation of the governing equation for the conservation of energy the same procedure is adopted. The control volume is shown below in Fig 2.3. The control volume is setup around the interior of the compartment in-between the compartment walls and the ambient. The compartment wall thickness is represented by δ_w. The control volume is outlined with dashed lines. Flows in and out of the vent are assumed to be constant and since mass flux from the burning fuel is considered negligible these flows are then equal. The temperature term T, is taken to be the gas temperature of the compartment.

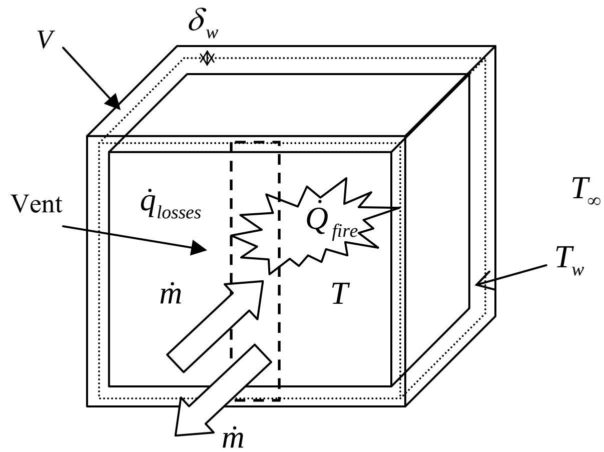

Figure 2.3: Control Volume for Conservation of Energy

The approximate one-dimensional governing equation for conservation of energy is:

$$\rho c_p V \frac{dT}{dt} + \dot{m} c_p \left(T - T_\infty\right) \approx \dot{Q}_{fire} - \dot{q}_{losses} \tag{2.4}$$

Eq. 2.4 equates the unsteady enthalpy term and enthalpy advection to the energy release from the fire and energy losses from the control volume respectively.

The approximate form of the governing for species concentration within the control volume in Fig 2.3 is:

$$\rho V \frac{dY_i}{dt} + \dot{m} Y_i = \frac{y_i \dot{Q}_{fire}}{\Delta h_c} \tag{2.5}$$

In Eq. 2.5, y_i is the chemical yield, the ratio between the mass of species i and the mass of the reacted fuel.

2.1.1 Defining a Characteristic Time and Velocity

From the governing equations it is apparent that both a reference or characteristic velocity and time are needed in order to make the governing equations dimensionless. They are derived by recognizing that the flows within the compartment are buoyancy driven flows. The proportionality of the momentum flux term to the buoyancy force term in Eq. 2.3 is examined giving:

$$\dot{m}u \sim (\rho_\infty - \rho)gV \tag{2.6}$$

Length scales, l, that will be adopted here and throughout the rest of this study refer to the characteristic length of the compartment, its height. Substituting Eq. 2.2 for the mass flow rate and revealing the length scales associated with each term in Eq. 2.6 gives:

$$\rho u^2 l^2 \sim (\rho_\infty - \rho)gl^3 \tag{2.7}$$

Rearranging the Eq. 2.7 gives:

$$\frac{u}{(gl)^{1/2}} \sim \left(\frac{\rho_\infty - \rho}{\rho}\right)^{1/2} \tag{2.8}$$

The characteristic velocity is defined as:

$$\tilde{u} = \left(\frac{\rho_\infty - \rho}{\rho} gl\right)^{1/2} \tag{2.9}$$

In this study normalized variables will be denoted using a '^' and characteristic variables with a '~'.

The ideal gas law gives the following relationship:

$$\frac{(\rho_\infty - \rho)}{\rho} = \frac{(T - T_\infty)}{T_\infty} \tag{2.10}$$

Substituting Eq. 2.10 into the definition of the characteristic velocity, Eq. 2.9:

$$\tilde{u} = \left(\frac{T - T_\infty}{T_\infty} gl \right)^{1/2} \tag{2.11}$$

An approximate form of the characteristic velocity is then:

$$\tilde{u} = (gl)^{1/2} \tag{2.12}$$

Examining now the proportionality of the unsteady momentum term and the buoyancy term from Eq. 2.3:

$$\rho V \frac{du}{dt} \sim (\rho_\infty - \rho) gV \tag{2.13}$$

Making Eq. 2.13 dimensionless using the characteristic velocity defined in Eq. 2.12 and revealing length scales associated with each term:

$$\frac{\rho (gl)^{1/2}}{\tilde{t}} \frac{d\hat{u}}{d\hat{t}} \sim (\rho_\infty - \rho) g \tag{2.14}$$

Rearranging Eq. 2.14 gives the definition for characteristic time. An approximate form of the characteristic time is then:

$$\tilde{t} = \left(\frac{l}{g} \right)^{1/2} \tag{2.15}$$

2.1.2 Dimensionless Groups from the Momentum Equation

In order to make the momentum equation dimensionless the length scales associated with each term must first be revealed. After which, each variable is normalized with its corresponding characteristic variable and the shear stress term is re-expressed as:

$$\Gamma = \mu \frac{du}{dx} \tag{2.16}$$

This results in the dimensionless governing equation for momentum:

$$\frac{d\hat{u}}{d\hat{t}} + \hat{u}^2 \approx \frac{(\rho_\infty - \rho)}{\rho} + \frac{p}{\rho l} + \frac{\mu}{\rho \tilde{u} l} \frac{d\hat{u}}{d\hat{x}} \tag{2.17}$$

The first π group is formed from the coefficient of the dimensionless stress term:

$$\Pi_1 \equiv \frac{\mu}{\rho \tilde{u} l} = \frac{1}{\mathrm{Re}} \tag{2.18}$$

This is the inverse of the familiar Reynolds number, Re, the ratio of inertial to viscous forces. If the exact form of the characteristic velocity is used as expressed in Eq. 2.11, this group can be rewritten in terms of the Grashof number, Gr:

$$\Pi_{1b} \equiv \frac{\nu}{\left(\frac{T - T_\infty}{T_\infty} g l^3 \right)^{1/2}} = \frac{1}{Gr^{1/2}} \tag{2.19}$$

2.1.3 Dimensionless Groups from the Energy Equation

The same procedure to make the momentum equation dimensionless is used to make the energy equation dimensionless. Temperature is normalized using ambient temperature, $\hat{T} = T/T_\infty$. This results in the following dimensionless governing equation for energy:

$$\frac{d\hat{T}}{d\hat{t}} + \left(\hat{T} - 1\right) \approx \frac{\dot{Q}_{fire}}{\rho_\infty c_p T_\infty g^{1/2} l^{5/2}} - \frac{\dot{q}_{losses}}{\rho_\infty c_p T_\infty g^{1/2} l^{5/2}} \tag{2.20}$$

The second π group is derived from the dimensionless source, or fire power term:

$$\Pi_2 \equiv Q^* = \frac{\dot{Q}_{fire}}{\rho_\infty c_p T_\infty g^{1/2} l^{5/2}} \tag{2.21}$$

The second π group expresses the ratio of the energy released from the fire to the enthalpy flow. It is also commonly referred to as the Zukoski[a] number, Q^*.

Heat lost from the system is a combination of losses to solid surfaces, i.e. compartment walls and losses to the ambient via the vent opening. These losses are represented below as $\dot{q}_w$ and $\dot{q}_o$ respectively.

$$\dot{q}_{losses} = \dot{q}_o + \dot{q}_w \tag{2.22}$$

Losses through the vent are expressed as the combined radiation from smoke layer and compartment walls and can be approximated using the equation:

$$\dot{q}_o = A_o \sigma\left(\varepsilon_{sl}\left(T^4 - T_\infty^4\right) + \left(1 - \varepsilon_{sl}\right)\left(T_w^4 - T_\infty^4\right)\right) \tag{2.23}$$

In the above equation ε_{sl} is the emissivity of the smoke layer and A_o the area of the vent. Convective losses from the vent are negligible.

[a] Due to the popularization of its use in fire by Dr. Ed Zukoski

Heat lost from the system via the compartment walls can be expressed figuratively using a circuit analogy.

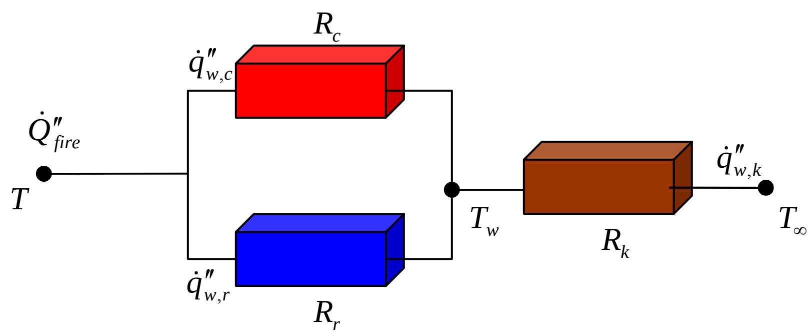

Figure 2.4: Circuit Analogy for Losses through Wall Surfaces

In the Fig 2.4 above, heat is transferred via the parallel paths of both convection and radiation to the compartment walls once released by the burning crib. This combined heat flux is then conducted through the walls.

$$\dot{q}''_{w,k} = \dot{q}''_{w,r} + \dot{q}''_{w,c} \tag{2.24}$$

The radiation heat exchange between the smoke layer and the wall can be expressed as a problem of radiation between two gray bodies. This problem is simplified by firstly assuming that the surface area of the smoke layer and compartment walls is equivalent and secondly that the compartment completely encloses the smoke layer. The second assumption results in the view factor between the walls and the smoke layer being unity. The general expression for this heat exchange is [5]:

$$\dot{q}_{w,r} = \frac{\sigma\left(T_{sl}^4 - T_w^4\right)}{\dfrac{1-\varepsilon_{sl}}{\varepsilon_{sl} A_{sl}} + \dfrac{1}{FA_{sl}} + \dfrac{1-\varepsilon_w}{\varepsilon_w A_w}} \tag{2.25}$$

In Eq. 2.25 F, is the shape factor between the smoke layer and wall. Using the simplifying assumptions above this reduces to:

$$\dot{q}''_{w,r} = \frac{\sigma\left(T_{sl}^4 - T_w^4\right)}{\dfrac{1}{\varepsilon_{sl}} + \dfrac{1}{\varepsilon_w} - 1} \tag{2.26}$$

If the smoke layer temperature is that of the compartment and the walls are considered to be covered in soot, Eq. 2.26 further reduces to:

$$\dot{q}''_{w,r} = \sigma\varepsilon_{sl}\left(T^4 - T_w^4\right) \tag{2.27}$$

The emissivity of the smoke layer can be expressed as, [6]:

$$\varepsilon_{sl} = 1 - e^{-\kappa L_e} \tag{2.28}$$

In Eq. 2.28 κ is the gas absorption coefficient and L_e, the mean beam length of the gas. The mean beam length is a function of the gas volume shape [4].

Convective heat transfer to the walls is governed by:

$$\dot{q}''_{w,c} = h_c\left(T - T_w\right) \tag{2.29}$$

Conduction through the wall can be approximated as conduction through a semi-infinite surface since the walls of the compartment will be designed using insulating materials. Fourier's law for conduction can then be simplified:

$$\dot{q}''_{w,k} = k_w \frac{dT}{dx} = k_w \frac{\left(T_w - T_\infty\right)}{\delta_w} \tag{2.30}$$

In Eq. 2.30 expression δ_w represents the physical wall thickness. The physical wall thickness is scaled using the thermal penetration depth for the case of a semi-infinite wall. Thermal penetration is proportional to the square root of the wall diffusivity and time [4], [5]:

$$\delta_t \sim \left(\alpha_w \tilde{t}\right)^{1/2} = \left(\frac{k}{\rho c}\right)_w^{1/2} \left(\frac{l}{g}\right)^{1/4} \tag{2.31}$$

Substituting Eq. 2.22 into the dimensionless loss term of the energy equation gives:

$$\hat{\dot{q}}_{losses} = \frac{\dot{q}_o + \dot{q}_w}{\rho_\infty c_p T_\infty g^{1/2} l^{5/2}} = \hat{\dot{q}}_o + \hat{\dot{q}}_w \tag{2.32}$$

The dimensionless wall loss term in Eq. 2.32 is equivalent to the conduction losses through the wall material, Eq. 2.24. Substituting Eq. 2.30 into the dimensionless wall loss term then normalizing wall temperature with the ambient and wall thickness with thermal penetration depth, Eq. 2.31, gives:

$$\hat{\dot{q}}_{w,k} = \left(\frac{A k_w T_\infty \left(\hat{T}_w - 1\right)}{\delta_t (\delta_w / \delta_t)} \right) \times \frac{1}{\rho_\infty c_p T_\infty g^{1/2} l^{5/2}} \tag{2.33}$$

From Eq. 2.33 the third and forth π groups are derived:

$$\hat{\dot{q}}_{w,k} = \frac{\Pi_3 \left(\hat{T}_w - 1\right)}{\Pi_4} \tag{2.34}$$

In Eq. 2.34 the π_3 group is defined as:

$$\Pi_3 \equiv \left(\frac{l^2 k_w T_\infty}{\delta_t} \right) \times \frac{1}{\rho_\infty c_p T_\infty g^{1/2} l^{5/2}} = \frac{(k\rho c)_w^{1/2}}{\rho_\infty c_p g^{1/4} l^{3/4}} \tag{2.35}$$

From Eq. 2.34 the π_4 is defined to be:

$$\Pi_4 \equiv \left(\frac{\delta_w}{\delta_t} \right) = \frac{\delta_w}{\left(\frac{k}{\rho c} \right)_w^{1/2} \left(\frac{l}{g} \right)^{1/4}} \tag{2.36}$$

From Eq. 2.24 the dimensionless wall conduction loss term, Eq. 2.33, can be expressed as the sum of the dimensionless convection and radiation heat flux to the walls. Therefore the dimensionless convection heat transfer term is:

$$\hat{\dot{q}}_{w,c} = \frac{h_c \left(\hat{T} - \hat{T}_w\right)}{\rho_\infty c_p g^{1/2} l^{1/2}} \tag{2.37}$$

The π_5 group is formed from its coefficient:

$$\Pi_5 \equiv \frac{h_c}{\rho_\infty c_p (gl)^{1/2}} \tag{2.38}$$

The dimensionless radiation flux is:

$$\hat{\dot{q}}_o = \frac{\sigma \varepsilon_{sl} T_\infty^3 \left(\hat{T}^4 - \hat{T}_w^4 \right)}{\rho_\infty c_p g^{1/2} l^{1/2}} \tag{2.39}$$

The coefficient from Eq. 2.39 then gives the π_6 group:

$$\Pi_6 \equiv \frac{\sigma \varepsilon_{sl} T_\infty^3}{\rho_\infty c_p g^{1/2} l^{1/2}} \tag{2.40}$$

The emissivity of the smoke layer provides the π_7 group which scales emissivity by preserving the absorbtivity and beam length.

$$\Pi_7 \equiv \kappa L_e \tag{2.41}$$

2.1.4 Dimensionless Groups from Species Conservation Equation

The species equation is made dimensionless through the same procedure adopted for both the momentum and energy equations. Energy has is scaled by enthalpy flow. This gives the equation:

$$\frac{\rho_\infty l^3}{\left(\frac{l}{g} \right)^{1/2}} \frac{dY_i}{d\hat{t}} + \rho_\infty (gl)^{1/2} l^2 Y_i = \frac{y_i Q^*}{\Delta h_c} \rho_\infty c_p T_\infty g^{1/2} l^{5/2} \tag{2.42}$$

Rearranging the above such that only the dimensionless heat release rate is on the right hand side of the equation gives:

$$\frac{\Delta h_c}{y_i c_p T_\infty} \frac{dY_i}{d\tau} + \frac{\Delta h_c Y_i}{c_p T_\infty y_i} = Q^* \tag{2.43}$$

Eq. 2.43, the dimensionless species equation, yields the final π group:

$$\Pi_8 = \frac{\Delta h_c}{y_i c_p T_\infty} \tag{2.44}$$

2.1.5 Summary of π Groups

Table 2.1 below summarizes the π groups mentioned in this chapter and their corresponding fundamental relationship.

Table 2.1: Summary of π Parameters

Π-Group	Dimensionless Relation	Derived Relationship
Π_1	$\frac{\mu}{\rho_\infty \tilde{u} l} = \frac{1}{\mathrm{Re}}$	Momentum flux to shear stress
Π_2	$\frac{\dot{Q}_{fire}}{\rho_\infty c_p T_\infty g^{1/2} l^{5/2}}$	Fire power to enthalpy flow
Π_3	$\frac{(k\rho c)_w^{1/2}}{\rho_\infty c_p g^{1/4} l^{3/4}}$	Wall conduction losses to advected enthalpy
Π_4	$\frac{\delta_w g^{1/4}}{\alpha_w^{1/2} l^{1/4}}$	Thermal thickness to wall thickness
Π_5	$\frac{h_c}{\rho_\infty c_p (gl)^{1/2}}$	Convective heat loss to advected enthalpy
Π_6	$\frac{\sigma \varepsilon_{sl} T_\infty^3}{\rho_\infty c_p (gl)^{1/2}}$	Heat loss to ambient to advected enthalpy
Π_7	$L_e \kappa$	Absorption coefficient and beam length
Π_8	$\frac{\Delta h_c}{y_i c_p T_\infty}$	Chemical energy and i^{th} species enthalpy

2.2 Scaling Relationships from π Groups

2.2.1 π_1 – Reynolds Number

The first π group is the inverse of the Reynolds number:

$$\Pi_1 = \frac{\mu}{\rho_\infty \tilde{u} l} = \frac{\mu}{\rho_\infty g^{1/2} l^{3/2}} \tag{2.45}$$

Neither the ambient density nor the dynamic viscosity of the fluid within the compartment is scaled in this study therefore this π group cannot be preserved. It is assumed though that the flows within the compartment are turbulent, hence Re will be large and as a result this group becomes negligible.

2.2.2 π_2 – Scaling Fire Power

Scaling of the fire power between the model, *m*, and the prototype, *p*, by preserving the π_2 group:

$$\Pi_2 = \frac{\dot{Q}_m}{\rho_\infty c_p T_\infty g^{1/2} l_m^{5/2}} = \frac{\dot{Q}_p}{\rho_\infty c_p T_\infty g^{1/2} l_p^{5/2}} \tag{2.46}$$

This results in the following relationship:

$$\dot{Q}_p = \dot{Q}_m \left(\frac{l_p}{l_m} \right)^{5/2} \tag{2.47}$$

Eq. 2.47 states that in order to scale fire power from the prototype to a scaled model the fire power must be scaled by the factor, $\left(l_p / l_m\right)^{5/2}$. For the rest of this report this scaling factor will be simply referred to as $l^{5/2}$. If in this case the model were to be scaled geometrically to be 1/10th that of the prototype then the fire power would scale as $(1/10)^{5/2}$.

As mentioned previously, compartment temperature is normalized with the ambient temperature. Since ambient temperature is not scaled compartment gas and wall temperatures both scale to the zero power:

$$T,\ T_w \sim l^0 \tag{2.48}$$

2.2.3 π₃ and π₄ – Wall Material Scaling

π groups 3 and 4 describe how the wall material and its thickness should be scaled. π_3 states that:

$$\Pi_3 = \frac{(k\rho c)_w^{1/2}}{\rho_\infty c_p g^{1/4} l^{3/4}} \Rightarrow (k\rho c)_w \sim l^{3/2} \tag{2.49}$$

The π_3 group scales thermal inertia of the wall material. From the π_4 group:

$$\Pi_4 = \frac{\delta_w g^{1/4}}{\alpha_w^{1/2} l^{1/4}} \Rightarrow \frac{\delta_w}{\alpha_w^{1/2}} \sim l^{1/4} \tag{2.50}$$

The above group then states how the physical wall thickness and thermal diffusivity of the wall material scale.

2.2.4 π₅ – Convective Heat Flux Scaling

The π_5 group scales the convective heat transfer coefficient:

$$\Pi_5 = \frac{h_c}{\rho_\infty c_p (gl)^{1/2}} \Rightarrow h_c \sim l^{1/2} \tag{2.51}$$

There is an alternate means of deriving a scaling relation for the convective heat transfer coefficient and that is through a turbulent forced flow boundary layer correlation [5]. This defines the Nusselt number and hence the convective coefficient as:

$$\mathrm{Nu} \equiv \frac{h_c l}{k} = 0.037\,\mathrm{Re}^{4/5}\,\mathrm{Pr}^{1/3} \tag{2.52}$$

Substituting Eq. 2.45 for Re and assuming that Pr for the flow is unity gives an alternate scaling for the convective heat transfer coefficient:

$$h_c \sim \left(\frac{\rho_\infty (gl)^{1/2} l}{\mu} \right)^{4/5} \frac{k}{l} \Rightarrow h_c \sim l^{1/5} \tag{2.53}$$

2.2.5 π_6 – Radiation Scaling

Preserving the π_6 group scales emissivity and as a result also scales radiation:

$$\Pi_6 = \frac{\sigma \varepsilon_{sl} T_\infty^3}{\rho_\infty c_p (gl)^{1/2}} \Rightarrow \varepsilon_{sl} \sim l^{1/2} \tag{2.54}$$

Using the approximate model for emissivity, Eq. 2.28, the scaling relation for emissivity can be rewritten as:

$$\varepsilon_{sl} = 1 - e^{-\kappa L_e} \sim l^{1/2} \tag{2.55}$$

The gas layer can be either optically thick, $\kappa L_e >> 1$, or optically thin, $\kappa L_e << 1$. In the optically thick case the emissivity of the smoke layer approaches unity. To scale the π_6 then requires:

$$\Pi_6 = \frac{\sigma T_\infty^3}{\rho_\infty c_p (gl)^{1/2}} \Rightarrow T_\infty \sim l^{1/6} \tag{2.56}$$

This cannot be achieved since the ambient temperature is not scaled, therefore the π_6 group cannot be preserved for the optically thick case. If the gas layer is optically thin then emissivity is proportional to the absorbtivity and beam length. The π_6 group then requires the following scaling:

$$\Pi_6 = \frac{\sigma(L_e\kappa)T_\infty^3}{\rho_\infty c_p (gl)^{1/2}} \sim \frac{\sigma(l\kappa)T_\infty^3}{\rho_\infty c_p (gl)^{1/2}} \Rightarrow \kappa \sim l^{-1/2} \tag{2.57}$$

The gas absorption coefficient varies with fuel, therefore by varying fuel type the gas absorption coefficient can be forced to scale to the negative half power and in doing so preserve the π_6 group.

2.2.6 Summary of Heat Flux Scaling

Conduction is simplified using the linear form of Fourier's law, Eq. 2.30. Substituting wall thickness scaling, Eq. 2.50, into Eq. 2.30 gives:

$$\dot{q}_k'' = k_w \frac{(T - T_\infty)}{\alpha_w^{1/2} l^{1/4}} \tag{2.58}$$

Simplifying Eq. 2.58 results in wall conduction scaling with thermal inertia:

$$\dot{q}_k'' \sim \frac{(k\rho c)_w^{1/2}}{l^{1/4}} \tag{2.59}$$

Thermal inertia is scaled by the π_3 group, Eq. 2.49. Substituting the scaling for thermal inertia into Eq. 2.59 results in the scaling relation for wall conduction:

$$\dot{q}_k'' \sim l^{1/2} \tag{2.60}$$

Convective heat flux scales according to the scaling relation for the convective coefficient used. Scaling using Eq. 2.53 results in convective heat flux scaling as:

$$\dot{q}_c'' \sim l^{1/5} \tag{2.61}$$

Alternatively according to Eq. 2.51, convective heat flux scales as:

$$\dot{q}_c'' \sim l^{1/2} \tag{2.62}$$

Similarly with convection, radiative heat transfer scales with emissivity. In the optically thick case emissivity approaches unity and from Eq. 2.56 cannot be preserved, therefore radiation scales as:

$$\dot{q}_r'' \sim l^0 \tag{2.63}$$

There are two approaches to scaling optically thin emissivity. The first approach varies the fuel and the second does not. If the fuel load is varied to force the gas absorption coefficient to scale by Eq. 2.57 then emissivity will scale to the half power. Therefore, for the optically thin case in which fuel is varied radiation scales as:

$$\dot{q}_r'' \sim l^{1/2} \tag{2.64}$$

If the fuel is not varied then emissivity will scale as the mean beam length. Since the mean beam length scales to the unity power, radiation in this instance scales as:

$$\dot{q}_r'' \sim l^1 \tag{2.65}$$

2.2.7 π_8 – Species Concentration

The π_8 group scales species yield. Since none of the terms in the group are scaled yield then scales as:

$$\frac{\Delta h_c}{y_i c_p T_\infty} \Rightarrow y_i \sim l^0 \tag{2.66}$$

2.2.8 Summary of Length Scaling Results

Table 2.2 summarizes the scaling requirements for each π group.

Table 2.2: Summary of π Group Scaling Results

Π Group	Quantity Scaled	Comments
T	Temperature	$T \sim l^0$
Π_1	Reynolds Number	*Not Explicitly Preserved*
Π_2	Fire Power	$\dot{Q} \sim l^{5/2}$
Π_3	Conduction	$(k\rho c)_w \sim l^{3/2}$ $\dot{q}''_k \sim l^{1/2}$
Π_4	Wall Thickness	$\dfrac{\delta_w}{\alpha_w^{1/2}} \sim l^{1/4}$
Π_5	Convection	$\dot{q}''_c \sim l^{1/5}$ $\dot{q}''_c \sim l^{1/2}$
Π_6	Radiation	$\dot{q}''_r \sim l^0$ $\dot{q}''_r \sim l^{1/2}$ $\dot{q}''_r \sim l^1$
Π_7	Species	$y_i \sim l^0$

For similitude between a prototype full scale enclosure fire and its scaled model the dependent variables are a function of the following independent dimensionless groups:

$$\left\{\frac{T_g}{T_\infty}, \frac{T_w}{T_\infty}, \frac{u}{(gl)^{1/2}}, y_i\right\} = function\left\{\frac{x_i}{l}, \frac{t}{\left(\frac{l}{g}\right)^{1/2}}, \Pi_{1\to 7}\right\} \qquad (2.67)$$

2.2.9 Preserved π Groups

It is not possible to preserve all the π groups derived previously. For example, the Reynolds number is not explicitly preserved. In order to preserve convection, the convective heat transfer coefficient needs to be scaled. The scaling theory then presents two contradictory methods to scale the convective heat transfer coefficient. To preserve radiation requires knowledge of the gas layer emissivity. Herein lays the 'art' of scaling, examining the dominant physics of a problem and preserving the pertinent π groups.

Fig 2.4 illustrates the circuit analogy for heat loss from the compartment. A quantification of the circuit resistor quantities was given in [7] and [3] and is listed in Table 2.3 below.

Table 2.3: Typical Thermal Resistor Quantities

Resistor	Range (m^2K/kW)
Conduction	$R_k \approx 316$
Convection	$R_c \approx 100$
Radiation	$R_r \approx 150$

From the Table 2.3 the conductive resistance is the most dominant thermal resistor. Designing the compartment walls using insulation board and blanket further increases this dominance. For this reason the π_3 and π_4 groups are preserved and the π_5, π_6, and π_7 groups discarded, i.e. conduction is preserved in favor of either convection or radiation. Eq. 2.67 is now modified to preserve the dominant physics:

$$\left\{\frac{T_g}{T_\infty},\frac{T_w}{T_\infty},\frac{u}{(gl)^{1/2}},y_i\right\} \approx function\left\{\frac{x_i}{l},\frac{t}{\left(\frac{l}{g}\right)^{1/2}},\Pi_2,\Pi_3,\Pi_4\right\} \tag{2.68}$$

2.3 Wood Crib Scaling

Wood cribs were chosen to represent a fuel load of furniture within the compartment. The wood cribs then had to be scaled according to the derived scaling relations. Fig 2.5 below shows an example of a wood crib and its associated variables.

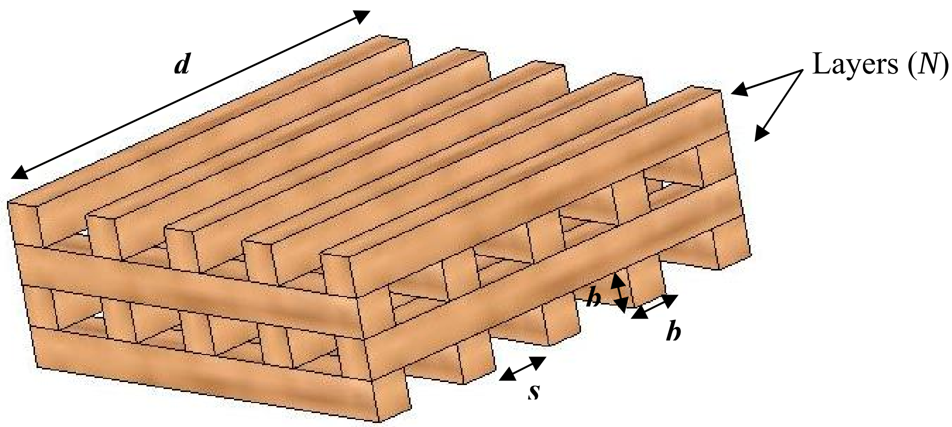

Figure 2.5: Example Wood Crib

The variables for a crib have been summarized below in Table 2.4.

Table 2.4: Crib Parameters

Crib Parameter Symbol	Physical Crib Property
N	Sticks per layer
n	Number of layers
b	Stick thickness
d	Stick length
s	Stick spacing

2.3.1 Wood Crib Theory

There has been extensive research into the burning rate of wood cribs. Notable work includes that of Gross [8] who discovered that the burning rate of various configurations of wood cribs can be grouped into two categories, either densely packed or openly packed cribs. Block [9] then defined a fundamental theory for the burning rate of either densely packed or openly packed cribs. He discovered that for densely packed cribs the burning rate was a strong function of crib height and packing density whereas in the openly packed case it was a function only of the physical properties of the fuel elements and not its geometry. Block went on to define this openly packed burning rate as:

$$\dot{m}''_f = Cb^{-1/2} \tag{2.69}$$

In Eq. 2.69, *C* is a constant representing the species of wood [9].

Both Gross and Heskestad [10] referred to this dependency on stick density as the *porosity* factor:

$$P \equiv \frac{A_v}{A_s} s^{1/2} b^{1/2} \tag{2.70}$$

An alternative view of porosity is as the ratio of vertical vent flow, $A_v s^{1/2}$, to the burning rate. Further work by Croce [11] shown below in Fig 2.6, clearly differentiates these two burning regimes. In Fig 2.6 below, it can be seen that for porosity below 0.5 mm burning rate is dependent on porosity, this is defined as the densely packed wood crib burning regime. For porosities larger than 0.5 mm the burning rate is porosity independent and this is defined to be the openly packed burning regime.

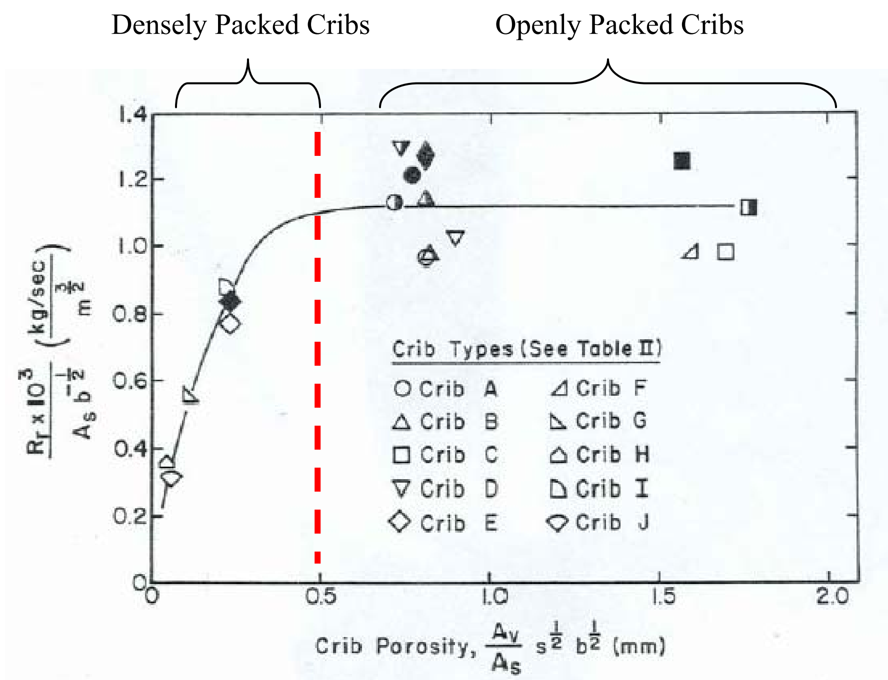

Figure 2.6: Crib Porosity and Burning rate Experiments by Croce [11]

All wood cribs were designed in this study to all fall under the category of porosity independent or openly packed burning regimes.

2.3.2 Derivation of Scaling for Crib Parameters

Fig 2.7 below is of a plan view of a wood crib. A_v is the crib vent area:

$$A_v = (d - nb)^2 \tag{2.71}$$

Stick length can be expressed as a sum of the stick thicknesses and the stick spaces:

$$d = nb + (n-1)s \tag{2.72}$$

Each crib variable can be expressed in terms of its scaling relations, i.e. $d \sim l^{d'}$ or $b \sim l^{b'}$. Using this technique of expressing the crib variables Eq. 2.72 can be rewritten as:

$$d = nb + (n-1)s \Leftrightarrow l^{d'} = l^{n'} l^{b'} + l^{n'} l^{s'} \tag{2.73}$$

For Eq. 2.73 to be dimensionally correct the following relationships must be true:

$$d' = n' + b' \tag{2.74}$$

$$d' = n' + s' \tag{2.75}$$

It can be seen from the two equations above that:

$$b' = s' \tag{2.76}$$

Stick spacing *s*, can be expressed as:

$$s = \frac{(d - nb)}{n - 1} \tag{2.77}$$

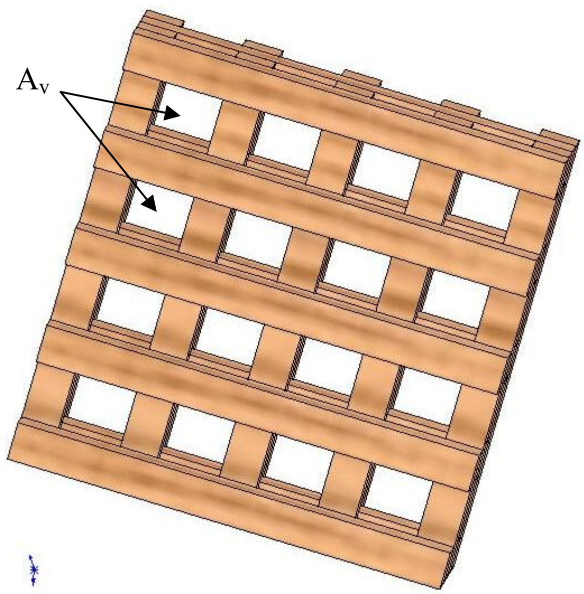

Figure 2.7: Plan View of Crib

From the π_2 group, Eq. 2.21, fire power scales as:

$$\dot{Q}_{fire} = \dot{m}_f \Delta h_c \sim l^{5/2} \tag{2.78}$$

Substituting the equation for the burning rate of porosity independent wood cribs, Eq. 2.69 into Eq. 2.78 gives:

$$\Delta h_c A_s C b^{-1/2} \sim l^{5/2} \tag{2.79}$$

A_s, in Eq. 2.79, is the surface area of the crib. Since the wood species used in this study is constant, neither Δh_c or C in Eq. 2.79 can be scaled as they are constant. The total surface area of a crib is approximated to be:

$$A_s \sim 4nNbd \tag{2.80}$$

Substituting Eq. 2.80 into Eq. 2.79 and removing the constant terms gives:

$$nNdb^{1/2} \sim l^{5/2} \tag{2.81}$$

Expressing Eq. 2.81 in terms of its dimensional relationship gives the equation:

$$n' + N' + d' + \frac{b'}{2} = \frac{5}{2} \tag{2.82}$$

Expressing porosity as the ratio of mass flow rate through vents to the burning rate gives:

$$P = \frac{A_v s^{1/2}}{A_s b^{-1/2}} \sim \frac{\dot{m}_v}{\dot{m}_f} \tag{2.83}$$

If porosity is then held constant between scales, air flow through the vents must scale as the burning rate:

$$\dot{m}_f \sim \dot{m}_v = A_v s^{1/2} \sim l^{5/2} \tag{2.84}$$

Substituting the expression for vent area and stick spacing derived above in Eq. 2.71 and Eq. 2.77 into the scaling relation for vent flows in Eq. 2.84 results in:

$$A_v s^{1/2} = (d - nb)^2 s^{1/2} \sim l^{5/2} \tag{2.85}$$

Expressing Eq. 2.85 in terms of its length scaling relations as was done previously:

$$2d' + \frac{s'}{2} = \frac{5}{2} \tag{2.86}$$

Since burn time scales according to flow time, burn time will scale as:

$$t_b = \frac{m_f}{\dot{m}_f} \sim l^{1/2} \tag{2.87}$$

Substituting in the scaling for burning rate and the expression for the total mass of a crib:

$$\frac{nNb^2 d\rho_{wood}}{l^{5/2}} \sim l^{1/2} \tag{2.88}$$

This results in the scaling relationship:

$$nNb^2 d \sim l^3 \tag{2.89}$$

This relationship expressed in terms of its scaling gives the equation:

$$n' + N' + 2b' + d' = 3 \tag{2.90}$$

From the stick length relationship, Eq. 2.72:

$$d' = n' + b' \tag{2.91}$$

There are therefore a total of four equations, Eq. 2.82, Eq. 2.86, Eq. 2.90 and Eq. 2.91, and four unknowns, *n'*, *N'*, *b'* and *d'*, which can now be solved to give the scaling relationship for each of the crib parameters.

2.3.3 Derivation of Scaling for Crib Parameters – Croce and Heskestad

Croce's scaling methodology [7], based on Heskestad's hypothesis [6] is outlined in this section. Full equations have been expressed in terms of their length scaling relations as was done in Eq. 2.73. Croce [7] also preserved the Zukoski number, Eq. 2.21, and therefore had the same scaling relationship for burning rate. Expressing this relationship as done previously in Eq. 2.82 gives:

$$n' + N' + d' + \frac{b'}{2} = \frac{5}{2} \tag{2.92}$$

Preserving porosity between scales then gives:

$$2d' + \frac{s'}{2} = \frac{5}{2} \tag{2.93}$$

Cribs were then designed to be geometrically similar, i.e. crib height and stick length were both scaled as l. Crib height relates to the number of layers and stick thickness as:

$$H = Nb \sim l \tag{2.94}$$

Giving the equation:

$$b' + N' = 1 \tag{2.95}$$

The stick length relationship, Eq. 2.72 and Eq. 2.75, gives the result:

$$d' = n' + b' \tag{2.96}$$

The geometric scaling of stick length gives:

$$d' = 1 \tag{2.97}$$

Burn time was not scaled according to flow time as was done in the new scaling methodology. There are now five equations, Eq. 2.92, Eq. 2.93, Eq. 2.95, Eq. 2.96 and Eq. 2.9 and four unknowns. This over-specified system of equations is solved by relaxing the final equation. Table 2.5 below summarizes both the crib parameter scaling relations from Croce and that derived using the new scaling methodology.

Table 2.5: Crib Parameter Scaling Relations

Crib Parameter	Croce	Flow Time Scaling
N	$l^{5/8}$	$l^{5/6}$
n	$l^{1/2}$	$l^{1/3}$
b	$l^{1/2}$	$l^{1/3}$
d	$l^{9/8}$	$l^{7/6}$
H	l^{1}	$l^{2/3}$

3. MEASURING HEAT FLUX

Chapter 2 discussed how heat flux scales in compartment fires. This discussion revealed contradictory methods for the scaling of both radiation and convection. Knowledge of how heat flux scales is especially important in light of the further development of this work to the scaling of structures within compartment fires.

This chapter discusses the technique used in measuring and differentiating the different heat fluxes within a compartment fire. A brief discussion is given of previous methods used to solve this problem. A novel technique of differentiating radiation and convection heat flux involving metal plate sensors is then introduced and given a rigorous theoretical treatment.

3.1 Previous Work on Convective Heat Flux Measurement

Tanaka and Yamada [12] investigated the convective heat flux during the early stages of a fire and at extinction. By assuming that the flow into the compartment was uni-directional the energy equation could be simplified and the heat transfer calculated by measuring the heat release rate, flow rate through the opening and temperature of the flow. The form of the energy equation used was:

$$\frac{d}{dt}\left(c_p \rho T V\right) = \dot{Q}_{fire} - c_p T_d \dot{m} - \dot{Q}_c \tag{3.1}$$

In Eq. 3.1, $\dot{Q}_{fire}$ represents the energy released by the fire, $\dot{Q}_c$, the convective loss component, T_d, the temperature of the flow through the vent and $\dot{m}$, the flow rate through the opening. If V and $c_p \rho T$ are assumed to be virtually constant then Eq. 3.1 can be simplified to:

$$\dot{Q}_c = \dot{Q}_{fire} - c_p T_d \dot{m} \tag{3.2}$$

Mass conservation is expressed as:

$$\frac{d}{dt}(\rho V) = -\dot{m} \tag{3.3}$$

Using the ideal gas law the mass conservation equation can be rewritten as:

$$\frac{dT}{dt}\frac{PMV}{RT^2} = \dot{m} \tag{3.4}$$

The rate of convective heat loss can then be calculated by substituting Eq. 3.4 into Eq. 3.2. The heat transfer coefficient is then calculated using the equation:

$$h_c = \frac{\dot{Q}_c}{A(T_w - T)} \tag{3.5}$$

Average temperature is taken to be gas temperature and the wall temperature was measured using a series of plates attached to the compartment walls. Thermocouples were welded to the unexposed faces of the plates and these temperatures were taken to be the wall temperature. The convective heat transfer coefficient was correlated with heat release rate giving [12]:

$$\frac{h_c}{\rho_\infty c_p (gl)^{1/2}} = \begin{cases} 2.0 \times 10^{-3} & Q^* \leq 4.0 \times 10^{-3} \\ 0.08(Q^*)^{2/3} & Q^* > 4.0 \times 10^{-3} \end{cases} \tag{3.6}$$

In the above expression Q* is the dimensionless fire power or Zukoski number from Eq. 2.21. The length scale l above refers to the characteristic length of the compartment which in this case is the compartment height.

More recently Tofilo et.al, [13], studied the effects of sootiness and heat release rate on heat transfer rates for a compartment fire. The radiative and convective components of the heat flux were differentiated and studied. They devised a technique, to extract this information, which utilized a metal plate embedded in the surface of the wall material, as shown in Fig. 3.1.

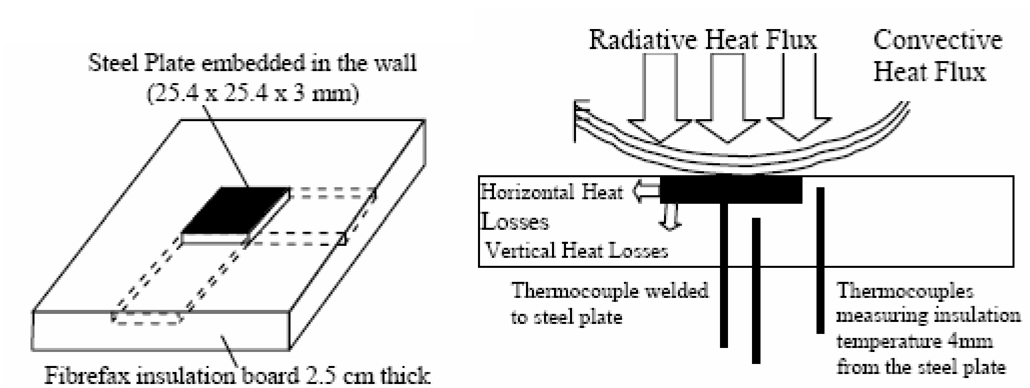

Figure 3.1: Metal Plate Technique to Measure Heat Flux [13]

The energy balance for the metal plate is [13]:

$$\dot{q}''_{inc} = \rho c \delta \frac{dT_s}{dt} + \dot{q}''_{cond} + h_c (T_s - T) + \sigma (T_s^4 - T^4) \tag{3.7}$$

The conduction losses from the plate, $\dot{q}''_{cond}$, can be measured using the thermocouples placed at either side of the plate within the insulation and using a simple linear approximation to the conduction equation. The unsteady temperature term can be considered negligible since the metal plate is thin. The incident heat flux to the metal plate, $\dot{q}''_{inc}$, is measured by a Gardon type heat flux gauge placed near the plate.

3.2 Novel Sensor Design and Approach

It was decided that a new sensor would be created to elucidate heat flux information from the crib fires. The metal plate sensor design is shown below in Fig. 3.2. The actual sensor is shown in Fig. 3.3. Throughout this report this sensor will be referred to as the metal plate sensor to differentiate it from the Gardon type heat flux gauges which are referred to as heat flux gauges.

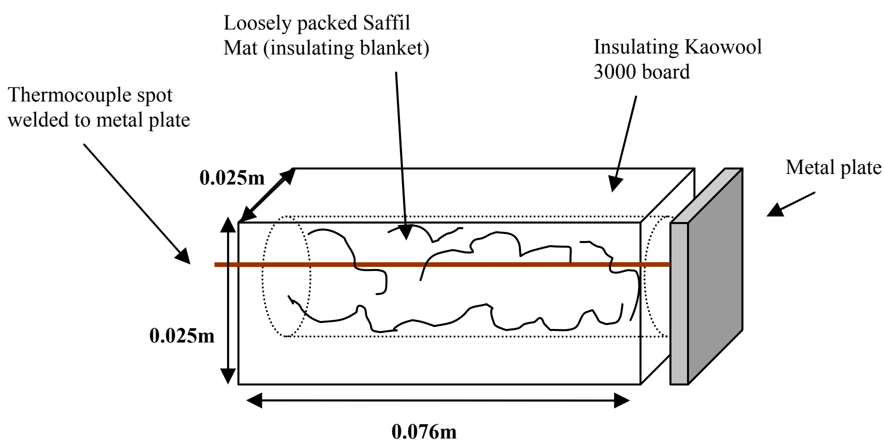

Figure 3.2: Metal Plate Sensor

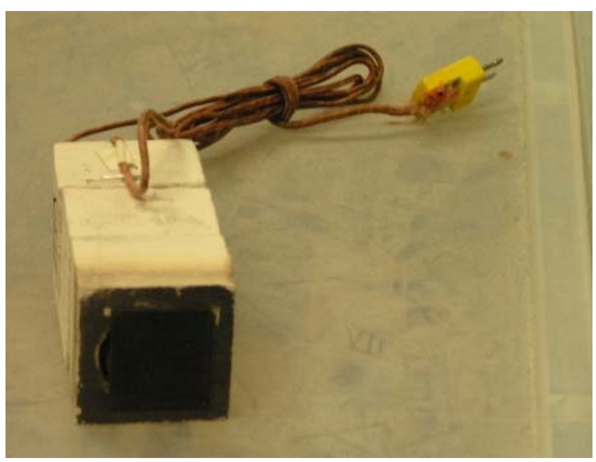

Figure 3.3: Built Plate Sensor

The sensor construction was straightforward; first a 2 mm thick steel plate was cut into 0.025 x 0.025 m pieces. This steel plate was first roughened using a sand blaster and then oxidized using a propane torch in order to increase plate emissivity. The emissivity was then further increased by spraying Medtherm® Heat flux gauge paint onto the surface of the plate with a known emissivity of 0.9. A 0.076 m long piece of 0.025 x 0.025 m square Kaowool 3000® insulating board was then hollowed and filled with Saffil Mat® insulating blanket. The blanket was packed loosely to ensure air gaps within the insulation in order to further decrease conduction losses from the metal plate. A K type thermocouple was then spot welded to the back of the metal plate and the plate attached to the board.

This metal plate sensor is used adjacent to a Gardon type heat flux gauge and both a gas and a wall temperature thermocouple. The compartment setup for these sensors is shown below in Fig. 3.4. The energy balance for the metal plate sensor is:

$$\left(\frac{mc}{A}\right)_m \frac{dT_m}{dt} + \dot{q}''_{cond} + \varepsilon_m \sigma T_m^4 = \dot{q}''_{fire,r} + h_{fire,c}\left(T_g - T_m\right) \qquad (3.8)$$

In Eq. 3.8 the unsteady term represents the heating of the metal plate; the thermocouple embedded in the plate measures T_m. The plate was chosen to be thin to minimize the effects of the transient heating term. The conductive losses, $\dot{q}''_{cond}$, are from the plate to the board and blanket behind it. On the right hand side of the equation the radiative heat flux from the fire, $\dot{q}''_{fire,r}$, represents both the radiation from the flames and the plume. The convective heat transfer coefficient, $h_{fire,c}$, is taken to be the same for both convection to the wall and to the metal plate. The conduction loss is deduced though calibration which will be discussed in the next section. The energy balance for the heat flux gauge is:

$$\dot{q}''_{HFG} = \dot{q}''_{fire,r} + h_{fire,c}\left(T_g - T_{HFG}\right) - \varepsilon_{HFG}\sigma T_{HFG}^4 \tag{3.9}$$

The data collected from the heat flux gauge measures $\dot{q}''_{HFG}$. The heat flux gauge is cooled to room temperature by cold water being re-circulated behind its face. T_{HFG} will be taken to be at ambient temperature, T_∞, throughout the rest of this study.

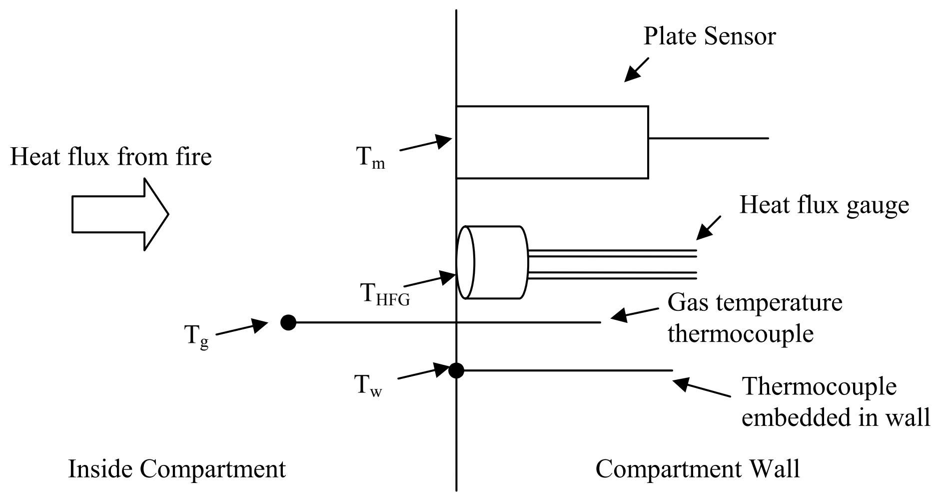

Figure 3.4: Plate Sensor, Heat Flux Gauge and Thermocouple Setup – Vertical View

The wall energy balance is:

$$\dot{q}''_{cond,w} + \varepsilon_w \sigma T_w^4 = \dot{q}''_{fire,r} + h_{fire,c}\left(T_g - T_w\right) \tag{3.10}$$

From Eq. 3.8, Eq. 3.9 and Eq. 3.10 there are a total of three equations and three unknowns. The measured and unknown quantities are summarized in Table 3.1.

Table 3.1: Summary of Unknown and Measured Variables

Measured	Unknown
T_g	$\dot{q}''_{fire,r}$
T_w	$h_{fire,c}$
T_m	$\dot{q}''_{cond,w}$
$\dot{q}''_{HFG}$	

Using the above setup the convective and radiative heat transfer components from the fire to the compartment walls can be differentiated and the conduction losses through the wall material measured.

3.2.1 Calibrating Sensor Conduction Loss and Time Response

Sensor calibration was conducted to resolve the conduction loss. Calibration was conducted using a heat flux gauge and metal plate sensor placed incident to the same radiant heat flux source as shown in Fig. 3.5. The radiant heat flux source in this case is a radiant panel which burns propane.

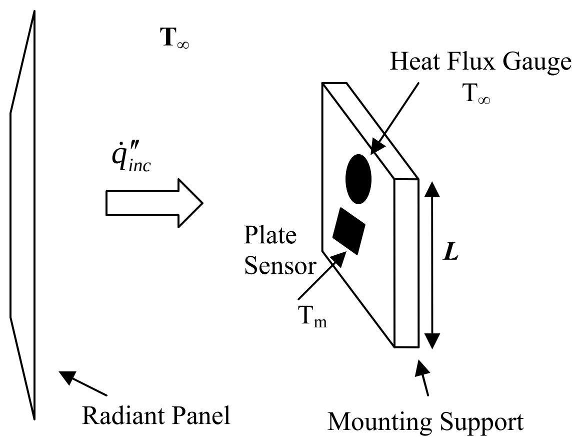

Figure 3.5: Sensor Calibration Setup

A steady state radiant heat flux from the panel is reached before the metal plate sensor is placed within its mounting support incident to the panel. The incident heat flux did vary slightly during testing. The energy balance for the plate sensor in the above setup is:

$$\left(\frac{mc}{A}\right)_m \frac{dT_m}{dt} = \alpha_m \dot{q}''_{inc} - \sigma\varepsilon_m\left(T_m^4 - T_\infty^4\right) - h_{c,plate}\left(T_m - T_\infty\right) - \dot{q}''_{cond} \tag{3.11}$$

In Eq. 3.11, $\dot{q}_{inc}$ represents the incident radiation heat flux from the radiant panel and α_m the absorbtivity of the metal plate. When the temperature of the metal plate sensor reaches steady state, the energy balance, Eq. 3.11, simplifies to:

$$\alpha_m \dot{q}''_{inc} = \sigma \varepsilon_m \left(T_m^4 - T_\infty^4\right) + h_{c,plate}\left(T_m - T_\infty\right) + \dot{q}''_{cond} \tag{3.12}$$

The heat flux gauge measures the incident heat flux, $\dot{q}''_{inc}$, and metal plate sensor temperature data is recorded. The conduction loss is rewritten using the linear approximation to Fourier's equation as:

$$\dot{q}''_{cond} = k\frac{\left(T_m - T_\infty\right)}{\delta} = h_k\left(T_m - T_\infty\right) \tag{3.13}$$

The above assumption is needed to linearize the metal plate sensor and is justifiable since this term is expected to be small. The metal plate sensor convective heat transfer coefficient can be calculated by using the theory for free convection from a vertical plate. The Gr number is first calculated to determine whether the flow is laminar or turbulent. The Gr number is defined as [6]:

$$\mathrm{Gr} \equiv \frac{g\beta}{\upsilon^2}\left(T_m - T_\infty\right)L^3 \tag{3.14}$$

The length scale L in Eq. 3.14 is the length of insulating board upon which the heat flux gauge and metal plate sensor are mounted. The mount is of dimensions 0.254m square. If $\mathrm{Gr} \ll 10^9$ the flows across the plate are laminar, and by setting Pr = 0.71, Nu can be calculated using [6]:

$$\mathrm{Nu} = \frac{\mathrm{Gr}^{1/4} \times \frac{3}{4}\mathrm{Pr}^{1/2}}{\left(2.435 + 4.884\mathrm{Pr}^{1/2} + 4.953\mathrm{Pr}\right)^{1/4}} \tag{3.15}$$

The convective heat transfer coefficient for a steady state metal plate sensor temperature can then be solved for from the definition of the Nu number and a specified conductivity for air, k_{air} :

$$\mathrm{Nu} = \frac{h_{c,plate} L}{k_{air}} \tag{3.16}$$

The effective conduction loss coefficient can be calculated by rearranging the steady state energy balance equation for the plate:

$$h_k = \frac{\alpha_m \dot{q}''_{inc} - \sigma \varepsilon_m \left(T_m^4 - T_\infty^4\right) - h_{c,plate}\left(T_m - T_\infty\right)}{\left(T_m - T_\infty\right)} \tag{3.17}$$

Fig. 3.6 below is a plot of the conductive losses from the plate sensor as a function of the incident flux. Fig. 3.7 below plots the conductive coefficient calculated from Eq. 3.17 above for various sensors constructed.

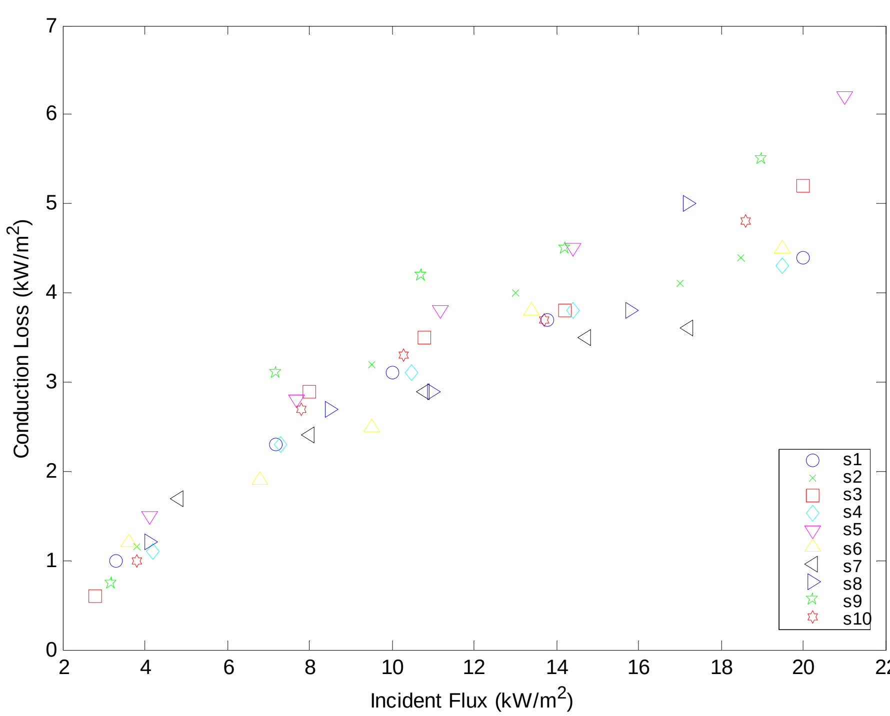

Figure 3.6: Conductive Losses from Metal Plate Sensor as a Function of Incident Flux

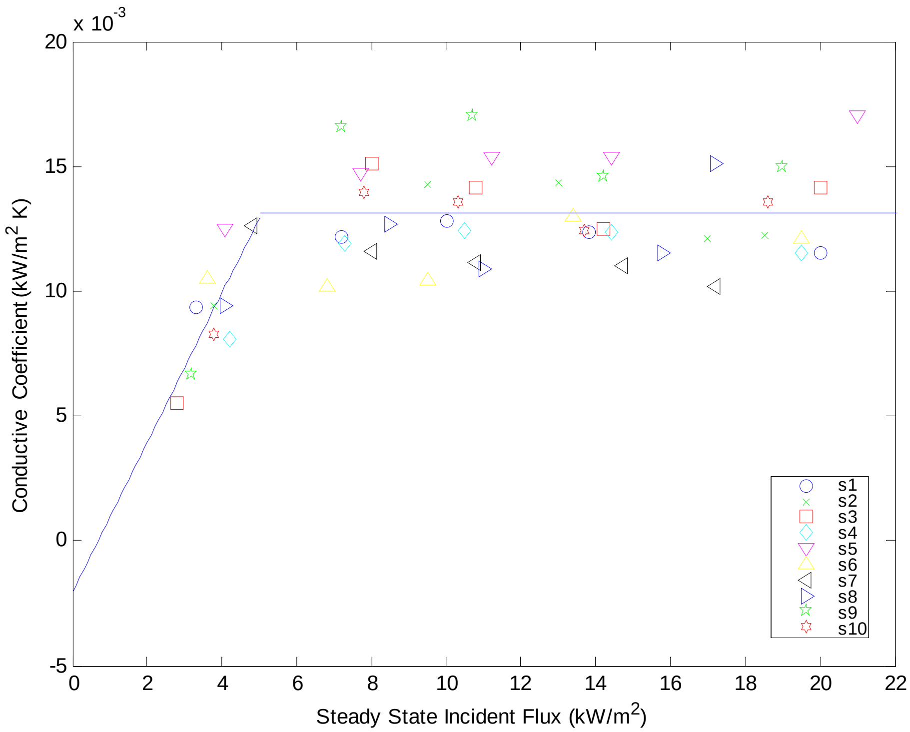

Figure 3.7: Metal Plate Sensor Conductive Heat Loss Coefficient

From Fig. 3.7 it is seen that for low incident flux the metal plate sensor has a positively sloped linear response to the incident flux which becomes constant at a flux higher than 5 kW/m^2. The correlation for the conductive heat loss coefficient is:

$$h_k = \begin{cases} 3.00\times10^{-3}\,\dot{q}''_{inc} - 2.04\times10^{-3} & \dot{q}''_{inc} < 5\dfrac{kW}{m^2} \\ 13.1\times10^{-3} & \dot{q}''_{inc} \geq 5\dfrac{kW}{m^2} \end{cases} \qquad (3.18)$$

The legends for Fig. 3.6 to Fig. 3.10 are labeled S1 to S10 in reference to the ten metal plate sensors built for the experiments.

In order for the data collected from the metal plate sensor to be meaningful, the time response of each metal plate sensor needs to be calculated. This time response can then be used to correct the inherent lag present in the metal plate sensor data.

The metal plate sensor radiation heat loss term is first re-expressed as:

$$\sigma\varepsilon_m\left(T_m^4 - T_\infty^4\right) = \sigma\varepsilon_m\left(T_m^2 + T_\infty^2\right)\left(T_m + T_\infty\right)\left(T_m - T_\infty\right) \tag{3.19}$$

Substituting Eq. 3.19 into the unsteady energy balance, Eq. 3.11, for the plate sensor gives:

$$\left(\frac{mc}{A}\right)_m \frac{dT_m}{dt} = \alpha_m \dot{q}_{inc} - h_{eff}\left(T_m - T_\infty\right) \tag{3.20}$$

The effective heat transfer coefficient, h_{eff}, represents:

$$h_{eff} = h_c + h_k + \sigma\varepsilon_m\left(T_m^2 + T_\infty^2\right)\left(T_m + T_\infty\right) \tag{3.21}$$

The measured metal plate sensor heat flux is taken to be:

$$\dot{q}_m'' = \sigma\varepsilon\left(T_m^4 - T_\infty^4\right) + h_c\left(T_m - T_\infty\right) + h_k\left(T_m - T_\infty\right) = h_{eff}\left(T_m - T_\infty\right) \tag{3.22}$$

Eq. 3.22 is then substituted into the energy balance, Eq. 3.20 to give:

$$\frac{(mc)_m}{A_m h_{eff}} \frac{d\dot{q}_m''}{dt} + \dot{q}_m'' = \alpha_m \dot{q}_{inc}'' \tag{3.23}$$

Defining the dimensionless time variable:

$$\tau = \frac{t}{\dfrac{(mc)_m}{A_m h_{eff}}} \tag{3.24}$$

The energy balance, Eq. 3.23, can be rewritten as:

$$\frac{d\dot{q}_m''}{d\tau} = \alpha_m \dot{q}_{inc}'' - \dot{q}_m'' \tag{3.25}$$

Using the initial condition that the metal plate sensor initially measures zero flux, $\dot{q}_m''(0) = 0$, Eq. 3.25 is solved giving:

$$\dot{q}''_m = \alpha_m \dot{q}''_{inc}\left(1 - e^{-\left(\frac{h_{eff} A_m}{(mc)_m}\right)t}\right) \tag{3.26}$$

From the above solution the metal plate sensor time response is:

$$t_r = \frac{(mc)_m}{h_{eff} A_m} \tag{3.27}$$

If the expression for the effective heat transfer coefficient, Eq. 3.21, of the plate is substituted into the Eq. 3.27 above it becomes explicit that there is temperature dependence in the time response:

$$t_r = \frac{(mc)_m}{\left[h_c + h_k + \sigma\varepsilon\left(T_m^2 + T_\infty^2\right)\left(T_m + T_\infty\right)\right]A_m} \tag{3.28}$$

Solving the energy equation, Eq. 3.20, in terms of temperature using the initial condition that the metal plate sensor is initially at ambient temperature gives the solution below where steady state temperature is T_{ss}:

$$\left(T_m - T_\infty\right) = \left(T_{ss} - T_\infty\right)\left(1 - e^{-\frac{t}{t_r}}\right) \tag{3.29}$$

For a particular steady state panel incident radiant flux there will be a unique time response for a metal plate sensor. When recorded time, t, equals response time, t_r, Eq. 3.29 reduces to:

$$\frac{\left(T_m - T_\infty\right)}{\left(T_{ss} - T_\infty\right)} = 1 - e^{-1} \tag{3.30}$$

Therefore from the recorded temperature data a measured time response can then be calculated. Fig. 3.8 below plots metal plate sensor time response as a function of steady state plate temperature and Fig. 3.9 as a function of steady state incident heat flux.

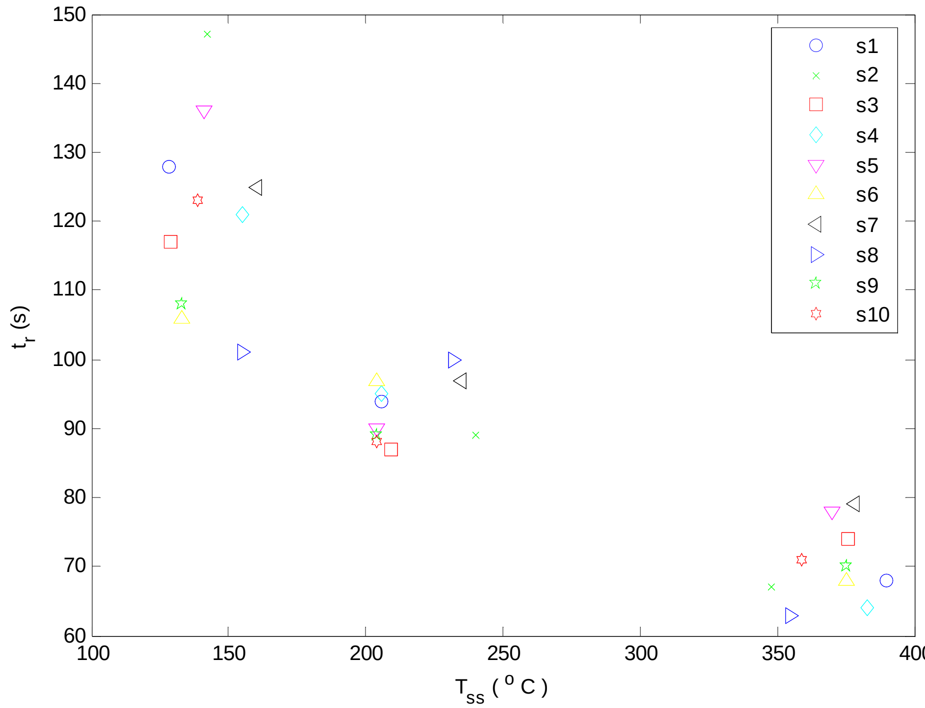

Figure 3.8: Metal Plate Sensor Time Response against Steady State Temperature

Fig. 3.8 above agrees with the theory from Eq. 3.28 which indicated that there is temperature dependence in the metal plate sensor time response.

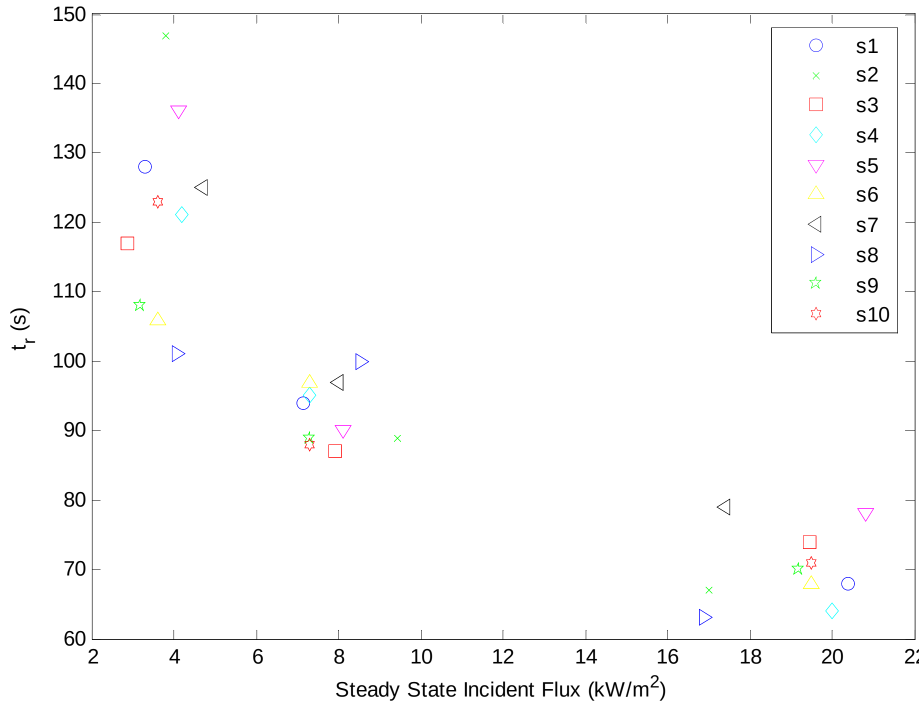

Figure 3.9: Metal Plate Sensor Time Response against Incident Flux

Having calibrated the metal plate sensor conduction loss and time response, $t_{r,m,}$ the effective mass, heat capacity and plate area can then be solved using the following expression:

$$t_{r,m}\left[h_c + h_k + \sigma\varepsilon\left(T_m^2 + T_\infty^2\right)\left(T_m + T_\infty\right)\right] = \frac{(mc)_m}{A_m} \tag{3.31}$$

Metal plate sensor measured, $\frac{(mc)_m}{A_m}$, is plot below in Fig. 3.10.

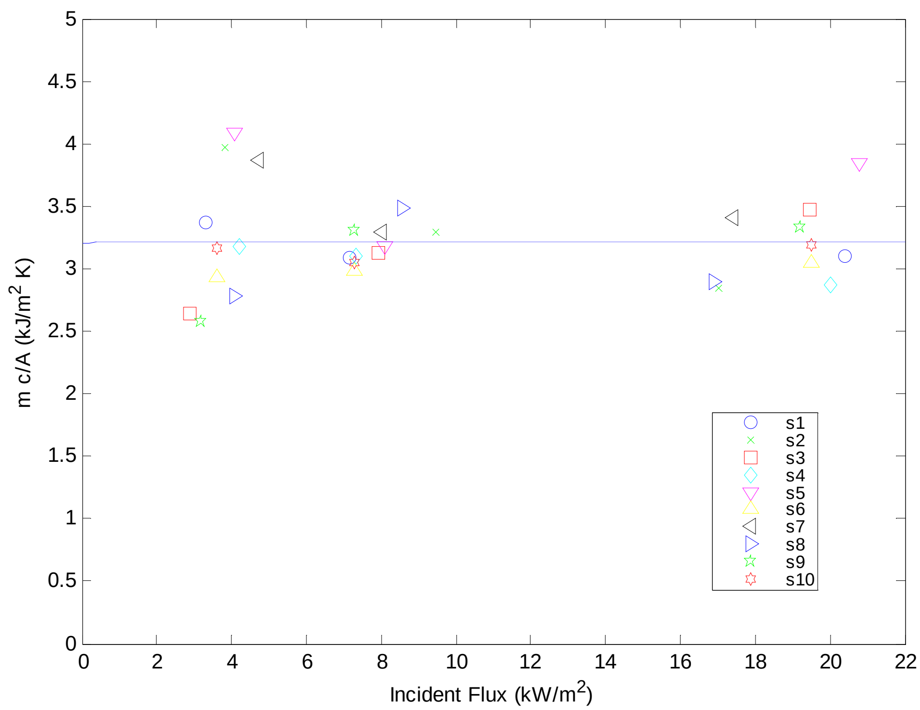

Figure 3.10: Metal Plate Sensor Properties Calibration Results

The measured metal plate sensor properties, $\left(\frac{mc}{A}\right)_m$, plot in Fig. 3.10 is constant with a value of approximately 3.21 kJ/kg K.

3.2.2 Corrected Sensor Output

Eq. 3.23 is solved numerically to obtain metal plate sensor data which has been corrected for the sensor time response. At each time step the metal plate sensor time response is computed using Eq. 3.28. The differential is computed numerically using a forward difference scheme. Sampling period is used as the time step.

$$t_{r,m}\frac{\dot{q}''_m(t+1)-\dot{q}''_m(t)}{\Delta t}+\dot{q}''_m(t)=\alpha_m\dot{q}''_{inc}(t) \tag{3.32}$$

The value obtained from numerically solving the left hand side of Eq. 3.32 above then gives the incident flux from the radiant panel. Fig. 3.11 and Fig. 3.12 below illustrate examples of a corrected calibration response in the case of metal plate sensors 1 and 2. In the legends of the figures below Q_m is the uncorrected metal plate sensor signal, Q_{crr} the signal calculated using Eq. 3.32 above and Q_{inc} the measured incident radiant panel heat flux from the heat flux gauge. The sensor measured response follows the incident heat flux closely once corrected. This provides a validation of the linear theory used to approximate the metal plate sensor response.

The plate incident flux is seen as an approximate step function by the plate sensor though it can be noticed that there is a slight increase in incident flux with time during the calibration. The turn off point during the calibration is viewed by the metal plate sensor as a step change in its input which then results in instabilities in the corrected sensor response. In the actual compartment, the fire will effectively provide a continuous "signal" seen by the metal plate sensor which can be correct without the discontinuities affecting the response as seen below.

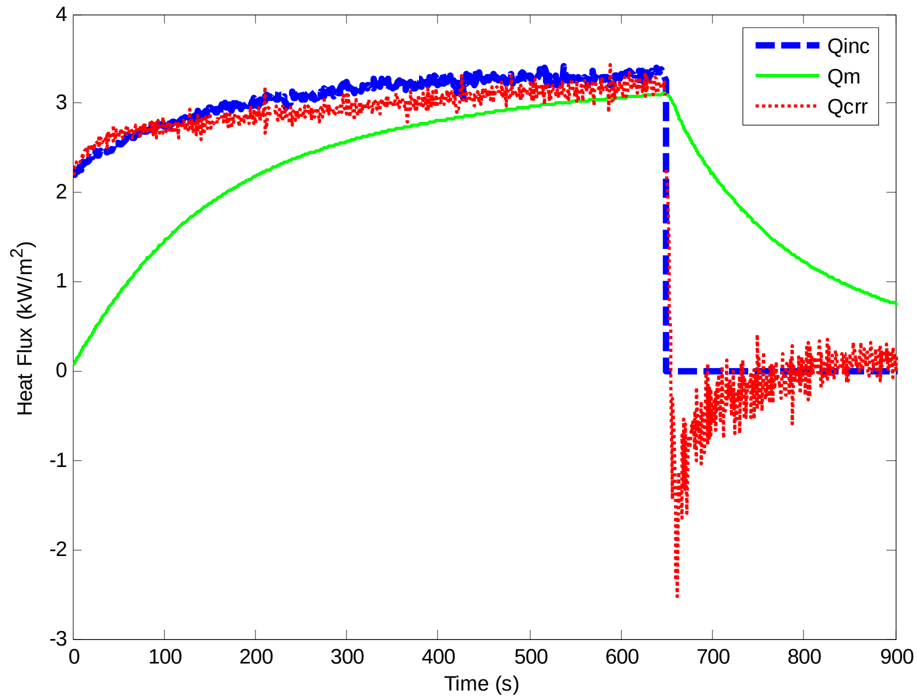

Figure 3.11: Sensor Measured and Corrected Response – Sensor 1

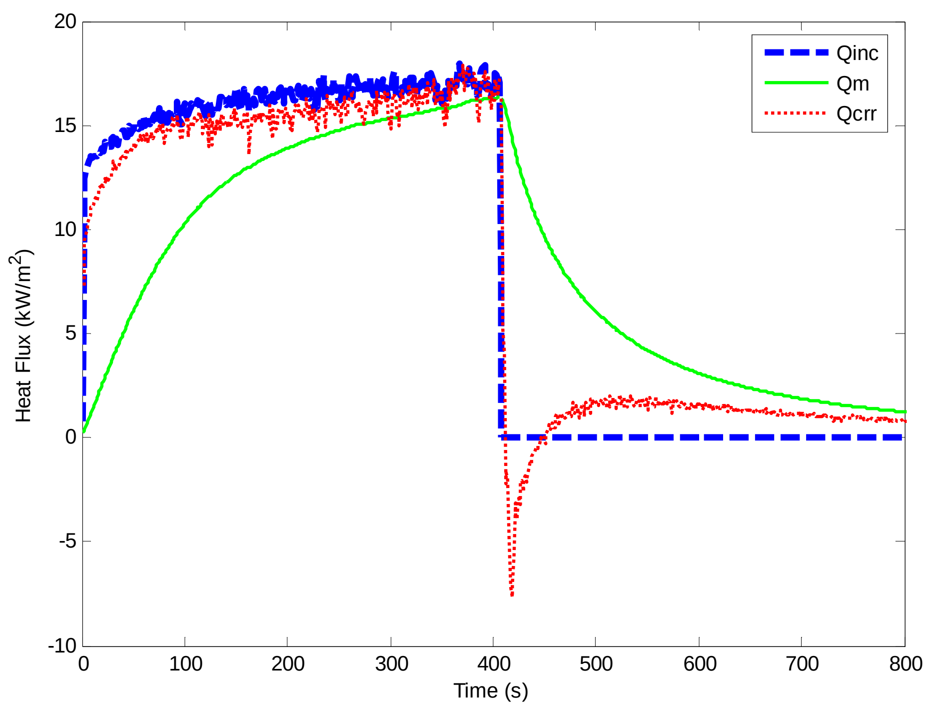

Figure 3.12: Sensor Measured and Corrected Response – Sensor 2

3.2.3 Sensor Time Response in Compartment Fires

Since the metal plate sensor has been proven to accurately measure a step change incident heat flux it can now be calibrated for use in compartment fires. The metal plate sensor time response when used in the compartment fire differs from the calibration case. Taking another look at the energy balance for the metal plate sensor:

$$\left(\frac{mc}{A}\right)_m \frac{dT_m}{dt} + \dot{q}''_{cond} + \varepsilon_m \sigma T_m^4 = \dot{q}''_{fire,r} + h_{fire,c}\left(T_g - T_m\right) \tag{3.33}$$

The metal plate sensor incident heat flux is:

$$\dot{q}''_{inc,fire} = \dot{q}''_{fire,r} + h_{fire,c}\left(T_g - T_m\right) \tag{3.34}$$

Expanding the radiation and conduction loss terms as done previously in Eq. 3.13 and Eq. 3.19, gives a new effective heat loss coefficient:

$$h_{eff,fire} = h_k + \sigma\varepsilon_m\left(T_m^2 + T_\infty^2\right)\left(T_m + T_\infty\right) \tag{3.35}$$

The sensor measured heat flux is:

$$\dot{q}''_m = h_k\left(T_m - T_\infty\right) + \varepsilon_m \sigma\left(T_m^4 - T_\infty^4\right) \tag{3.36}$$

Substituting Eq. 3.36 into the energy equation balance, Eq. 3.33, and using the dimensionless time, τ, defined in Eq. 3.24 results in the following first order differential equation:

$$\frac{d\dot{q}''_m}{d\tau} + \dot{q}''_m = \dot{q}''_{inc,fire} \tag{3.37}$$

The time response for the metal plate sensor when used in a compartment fire is:

$$t_{r,fire} = \frac{(mc)_m}{A_m h_{eff,fire}} \tag{3.38}$$

4. EXPERIMENT DESIGN AND METHODOLOGY

In chapter 4 the methodology used to design the experiments which were then used to investigate the scaling of heat flux within compartment fires is laid out. This process begins with the development of the compartments at each scale; full scale, 1/8 scale, 1/4 scale and 3/8 scale. The compartment fuel load and wall material design are then explained. The locations of the sensors used in obtaining the heat flux data from the compartment fires are illustrated. Finally a brief discussion is given on the technique used to ignite the wood cribs.

4.1 Design Requirements for Scaling Validation Experiments

To test the new scaling theory developed in chapter 2 and understand the scaling of heat flux in compartment fires a series of experiments were constructed within the framework outlined below.

1) Wood cribs must burn in porosity controlled regime.
2) The full scale wood crib must have a burn time of one hour.
3) The smallest wood crib must have a minimum of 5 sticks per layer and 4 layers.
4) Full scale fuel load should represent a realistic occupancy loading.
5) Full scale compartment will be of dimensions 3.76 x 3.76 x 2.54 m.
6) Full scale wall material will be Gypsum Board with a thickness of 15.9 mm

The porosity requirement is satisfied by setting the minimum crib porosity at 0.7 mm. From Fig. 2.6 it was seen that the minimum porosity to be in such a burn regime is 0.5 mm. A porosity of 0.7 mm was chosen to include a margin of error into the design. A larger porosity was not chosen as crib size and its associated costs, increases proportionally with porosity. The one hour burn time requirement was specified with the future goal of placing a structure within the compartments to test structural fire scaling. A one hour burn time will then replicate a standard fire resistance test for a building assembly [3]. The third requirement denotes a minimum crib size, below which the crib scaling theory does not hold, [3]. The final three requirements of the framework were based upon the desire to build a realistic compartment [3].

Three scale models, 1/8, 1/4 and 3/8, of the full scale compartment were then designed to fit the space constraints of the current laboratory facilities.

4.1.1 Full Scale Crib and Vent Design

In creating a design fire of one hour using wood cribs taking factors such as expense and facility space into account it became apparent that a free burning compartment fire was impracticable. A one hour free burning compartment fire would also require a wood crib whose area would exceed the floor area of the compartment. It was therefore decided to design a ventilation limited fire.

Harmathy [14] studied the burning rate of wood cribs in compartments under different ventilation conditions. Fig. 4.1 below illustrates his results. The relationship for burning rate and air flow rate into the compartment was derived for ventilation limited conditions to be [14]:

$$\dot{m}_f = 0.163 U_a \tag{4.1a}$$

$$U_a = 0.145 \rho_\infty g^{1/2} A_o h^{1/2} \tag{4.1b}$$

In Eq. 4.1, U_a is the flow rate of air through the vent, A_o is the vent area and h, the vent height. For simplicity the vent height was fixed to the full scale compartment height and only its width varied.

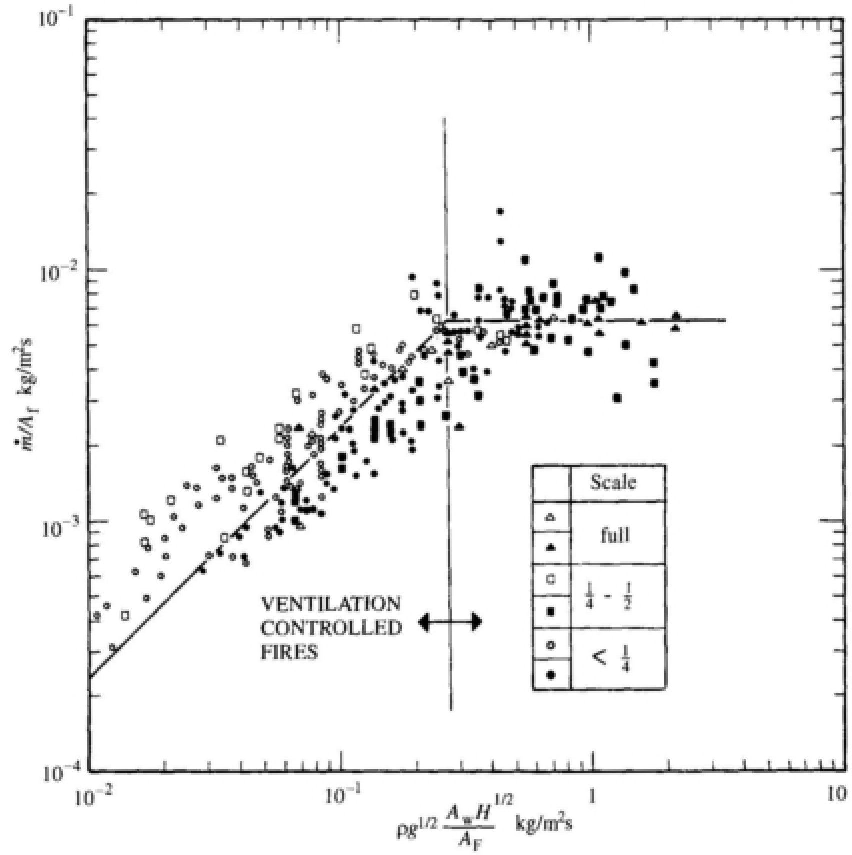

Figure 4.1: Burning Rate Behaviour of Cribs in Compartments [14]

In developing the full scale crib the requirement for the smallest scale, in this case the 1/8 scale, to have 5 sticks per layer and 4 layers results in the full scale crib having 28 sticks per layer and 8 layers, by the wood crib scaling laws in Table 2.5. Both parameters have been rounded to the nearest whole number since partial sticks and layers are not possible. The remaining wood crib design variables are stick length and thickness. The surface area of a crib, without overlap was derived to be:

$$A_s = nb^2\left[\left(1-n+2\frac{d}{b}\right)2N+2n-\frac{d}{b}\right] \tag{4.2}$$

Substituting Eq. 4.2, Eq. 2.71 and Eq. 2.77 into Eq. 2.70:

$$P = \frac{A_v}{A_s}s^{1/2}b^{1/2} = \frac{(d-nb)^{5/2}(n-1)^{-1/2}b^{1/2}}{nb^2\left[\left(1-n+2\frac{d}{b}\right)2N+2n-\frac{d}{b}\right]} \tag{4.3}$$

By setting porosity to 0.7 mm the above result can be re-arranged to give:

$$nb^2\left[\left(1-n+2\frac{d}{b}\right)2N+2n-\frac{d}{b}\right]0.7-(d-nb)^{5/2}(n-1)^{-1/2}b^{1/2} = 0 \tag{4.4}$$

Given a fixed stick thickness, the minimum stick length was calculated to satisfy Eq. 4.4 using a simple optimization algorithm. Once the crib parameters for a full scale crib are set and its mass calculated, the burn time is computed using Eq. 4.1a and Eq. 4.1b. The compartment vent size can then be varied until a burn time of approximately 70 minutes is reached. Finally loading on the compartment floor is calculated and compared against a standard office occupancy loading of 12 pounds per square foot (psf), or 545.5 Pa [15]. This process was repeated until a satisfactory burn time and loading was reached.

Fig. 4.2 below shows a plot of varying vent size and burn time for various full scale crib stick thickness.

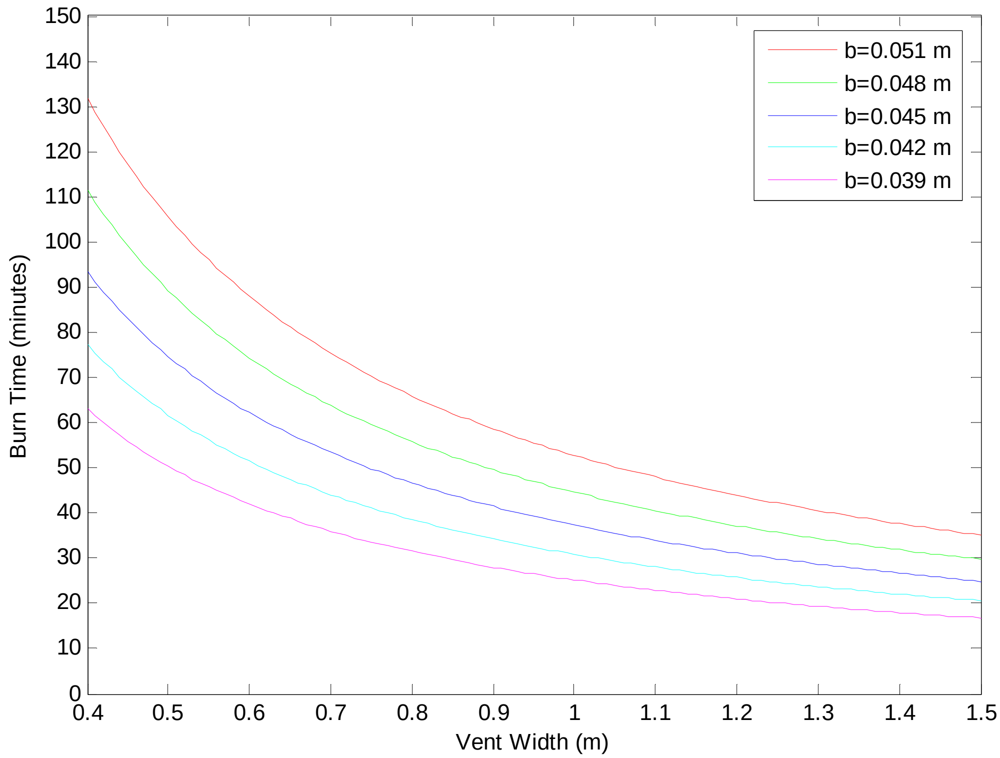

Figure 4.2: Burn Time for Different Stick Thicknesses

A burn time of 70 minutes at full scale was chosen to include a margin of error in the design. In the final design a full scale thickness of 0.045 m was chosen with a full scale compartment vent width of 0.5 m. The full scale loading was 11.46 psf or 548.7 Pa. Table 4.1 below summarizes the crib design at each scale. Rounding error from the number of sticks per layer and layers calculation results in changes in the porosity from the design value of 0.7 mm.

Table 4.1: Final Large Crib Design Parameters

Scale	b (m)	d (m)	n	N	Porosity (mm)
1	0.0445	2.335	28	8	0.73
3/8	0.0321	0.743	12	6	0.79
1/4	0.028	0.463	9	5	0.68
1/8	0.0222	0.206	5	4	0.72

The small crib design was based on a burn size that would be approximately 1/10th that of the large fire. Table 4.2 below outlines the specifications for the small crib design.

Table 4.2: Small Large Crib Design Parameters

Scale	*b* (m)	*d* (m)	*n*	*N*	Porosity (mm)
1	0.0191	1.257	28	8	0.70
3/8	0.0137	.4004	12	6	0.75
1/4	0.012	0.250	9	5	0.68
1/8	0.0095	0.111	5	4	0.71

4.1.2 Compartment Wall Material Design

The compartment wall material design involved selecting appropriate insulating materials with properties that matched Gypsum board at full scale. This meant calculating both the π_3 and π_4 groups for a specific material thought to be appropriate at a specific scale and comparing it against the π_3 and π_4 groups for gypsum board. For example, an appropriate 1/8 scale material would be an insulating blanket. Using data for these blankets provided by Kaowool® the π_3 and π_4 groups could be calculated and the materials compared to gypsum board. The materials with the closest match to gypsum board at each scale were then selected. Fig. 4.3 and Fig. 4.4 below illustrate the ability of the selected compartment wall materials to match that of gypsum board at full scale.

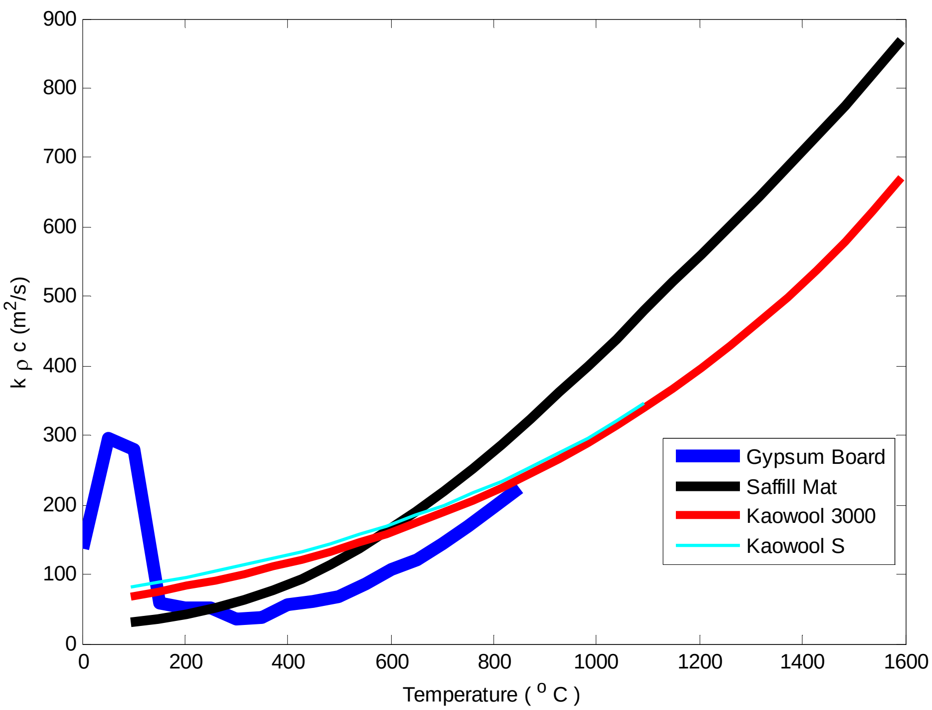

Figure 4.3: Scaled Wall Material Properties Plot against Gypsum Board

Compartment wall materials chosen came with a specified manufacturer thickness. Using these thickness and the material properties the π_4 group for each of the materials was plot against temperature, Fig. 4.4.

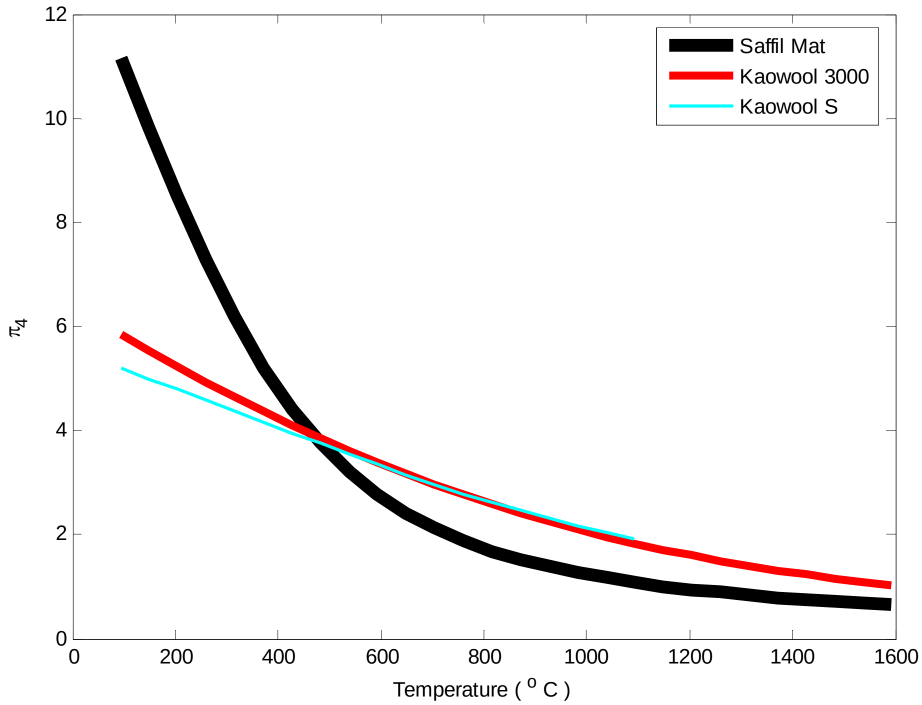

Figure 4.4: Materials Scaled π_4 Group Compared to Gypsum Board

The three materials which were the closest matched to gypsum board were Saffil Mat, Kaowool 3000 Board and Kaowool S board for the 1/8, 1/4 and 3/8 scale compartments respectively. Their thicknesses at their respective scales were 34 mm for the Saffil Mat and 13 mm for the two boards.

4.1.3 Proposed Testing Schedule

An experiment matrix was then developed for the compartment fires. Due to the size of the 3/8 scale compartment and lack of available facilities to conduct experiments of this size, it was only possible for 1/8 and 1/4 scale compartment fires to be conducted. Two small and large fires were conducted at the 1/8 scale and one of each was conducted at the 1/4 scale. Table 4.3 below summarizes the test schedule and the acronyms for each test.

Table 4.3: Compartment Burn Testing Schedule

Test ID	Description
1/8SF1	1/8 Scale small fire – Burn 1
1/8SF2	1/8 Scale small fire – Burn 2
1/8LF1	1/8 Scale large fire – Burn 1
1/8LF2	1/8 Scale large fire – Burn 2
1/4SF1	1/4 Scale small fire – Burn1
1/4LF2	1/4 Scale large fire – Burn1

4.2 Compartments and Sensor Setup

The full scale compartment of dimensions 3.76 x 3.76 x 2.54 m corresponding to its width, length and height respectfully, has to be scaled geometrically to design three compartments at 1/8, 1/4 and 3/8 scales. These compartments have dimensions listed below in Table 4.4.

Table 4.4: Summary of Compartment Dimensions

Compartment Scale	Dimensions (m) (W x L x H)
1/8	0.47 x 0.47 x 0.32
1/4	0.94 x 0.94 x 0.635
3/8	1.41 x 1.41 x 0.95

Four sensor locations were selected for the 1/8 scale compartment. These were on the upper left and right walls, the ceiling and the lower back wall. The first three locations were used to gather heat flux data in the upper layer of the fire in the compartment and the forth location was in the lower layer of the fire. Fig. 4.5, Fig. 4.6 and Fig. 4.7 illustrate the location of the sensors in the 1/8 scale compartment.

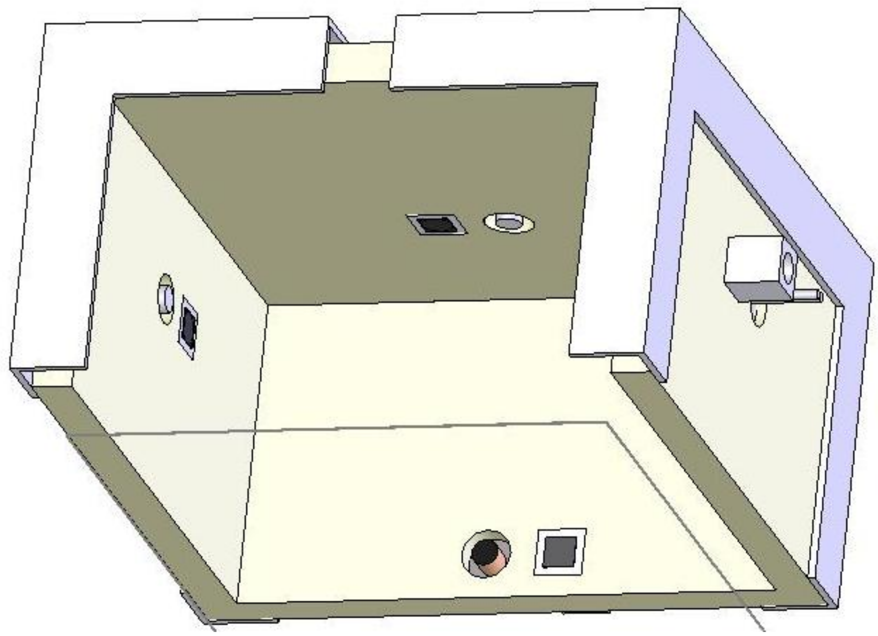

Figure 4.5: 1/8 Scale Compartment Sensor Setup

The Fig. 4.5 shows the sensor setup with the compartment floor and vents cut away. Fig. 4.6 below shows the setup from the outside looking at the compartment from the rear.

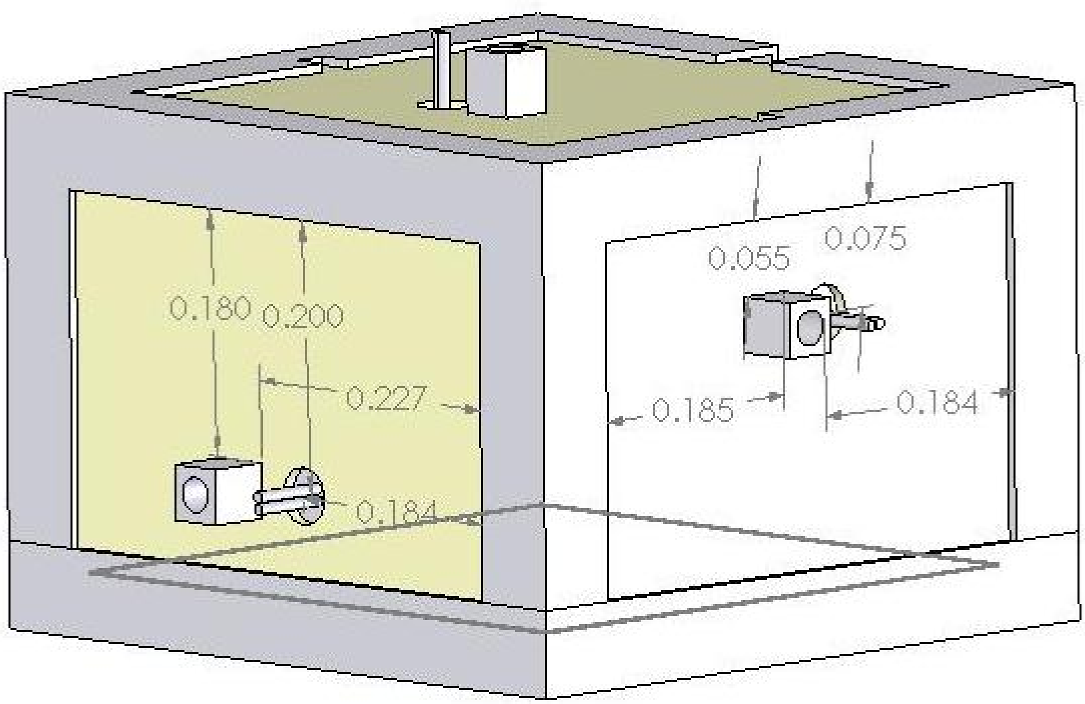

Figure 4.6: 1/8 Scale Compartment Sensor Setup - Rear View Dimensions

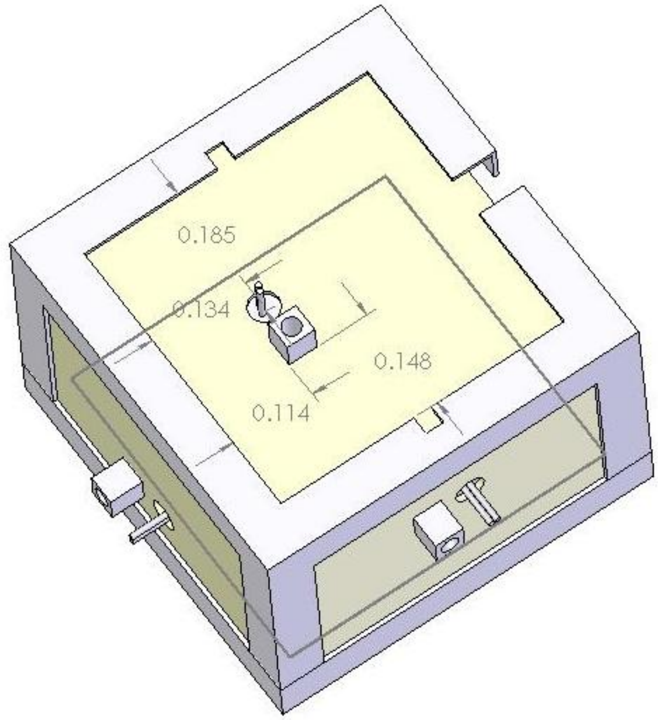

Figure 4.7: 1/8 Scale Compartment Sensor Setup - Top View Dimensions

Between scales the locations of the sensors are scaled geometrically to be at homologous locations. After testing was completed with the 1/8 scale compartment one of the Gardon type heat flux gauges failed resulting in only three sensor locations being utilized in the 1/4 scale. The sensors were located at the left wall, back wall and ceiling locations homologous to the sensor locations in the 1/8 scale compartment. Fig. 4.8, Fig. 4.9 and Fig. 4.10 below illustrate the location of the sensors in the 1/4 scale compartment.

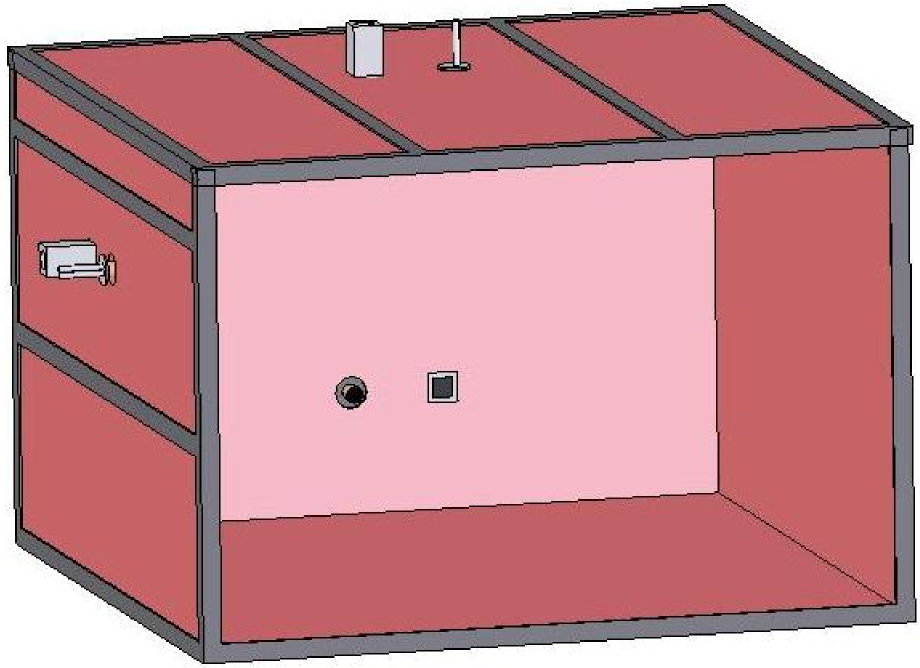

Figure 4.8: 1/4 Scale Compartment Sensor Setup - Front View

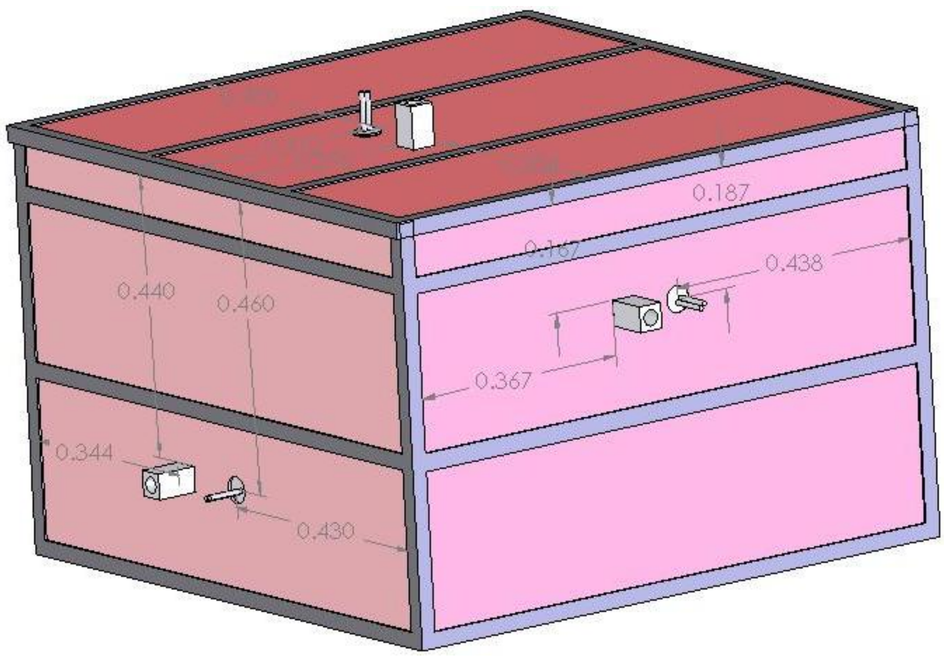

Figure 4.9: 1/4 Scale Sensor Setup - Dimensions

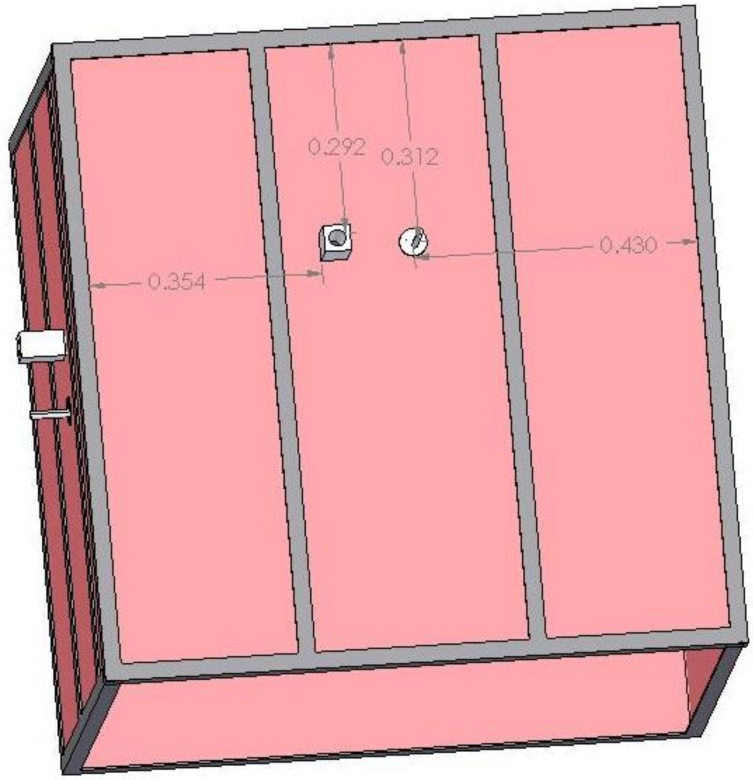

Figure 4.10: 1/4 Scale Sensor Setup - Dimensions

Sensor locations are labeled using a coordinate system based on their position relative to the height, *H*, width, *W*, or depth, *D*, of the compartment. Since the sensor locations were homologous between scales, these positions are identical in both the 1/4 and 1/8 scale compartments. The origin (0,0,0), is located at the back wall lower left hand corner of the compartment. The front wall, right upper corner is the (*D*,*W*,*H*) coordinate. Fig. 4.11 below illustrates this labeling convention. Table 4.5 below lists the coordinate locations of the sensors in the compartments. The location chosen to represent the sensor setup was the plate sensor location.

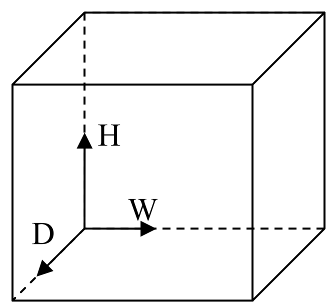

Figure 4.11: Coordinate Labelling Convention

Table 4.5: Sensor Setup Coordinates

Sensor Location	Coordinate
Left Wall	(0.44D,0,0.65H)
Back Wall	(0,0.55W,0.2H)
Ceiling	(0.44D,0.37W,H)
Right Wall	(0.55D,W,0.65H)

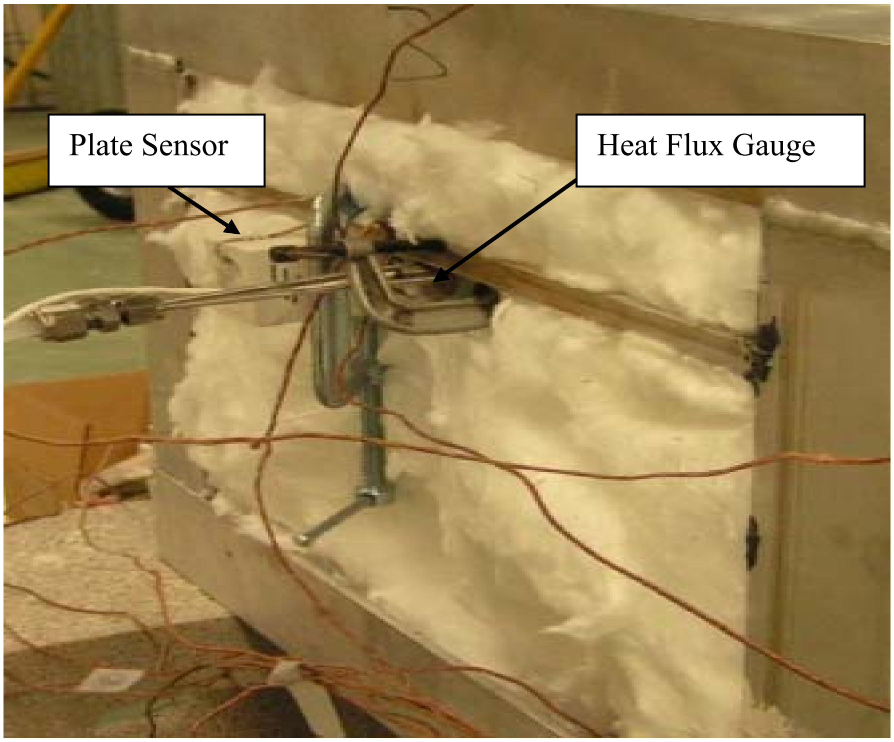

Figure 4.12: Sensor Setup - 1/8 Scale Compartment

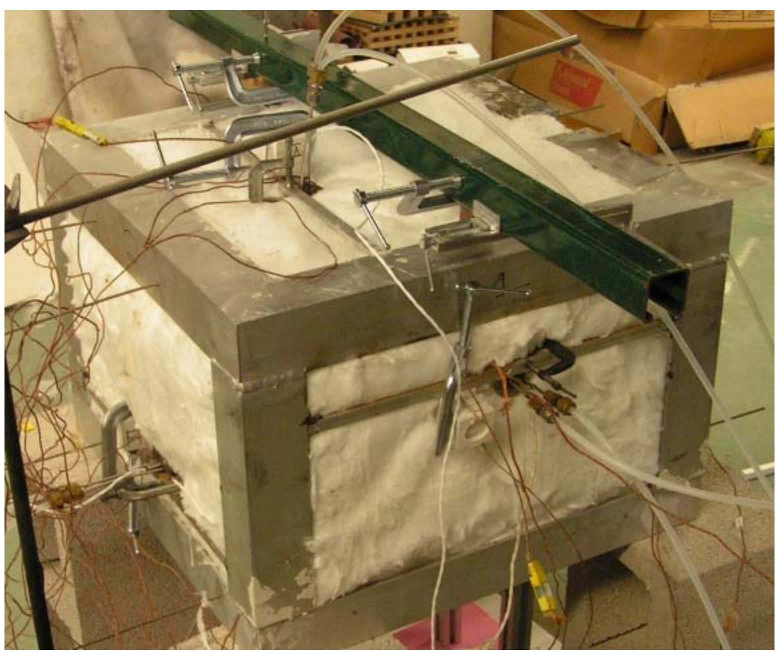

Figure 4.13: Left Wall, Ceiling and Back Wall Sensor Setup - 1/8 Scale Compartment

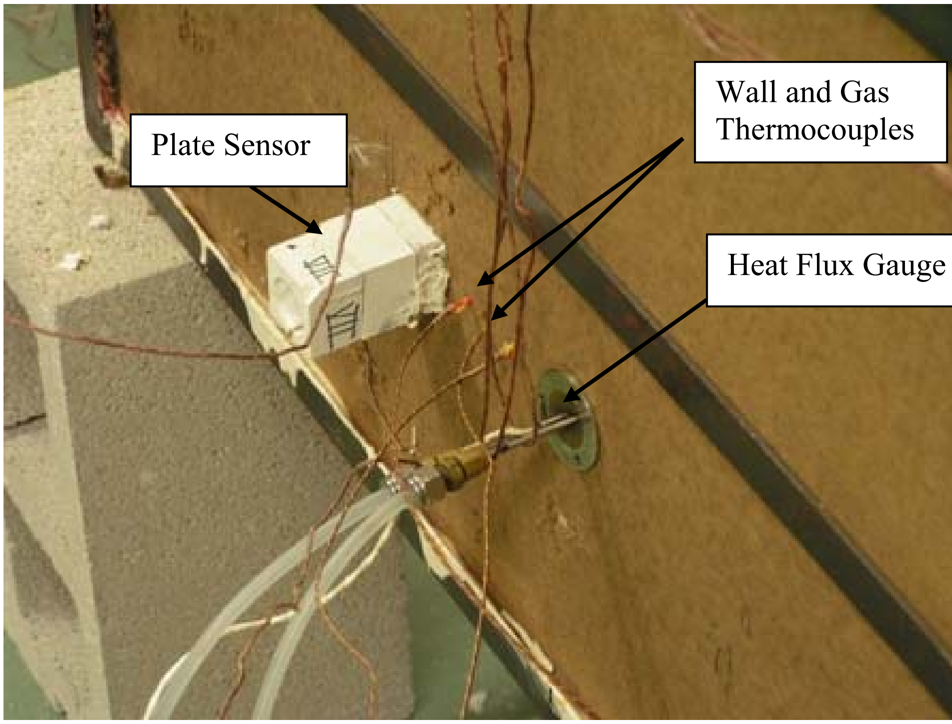

Figure 4.14: Sensor Setup - 1/4 Scale Compartment

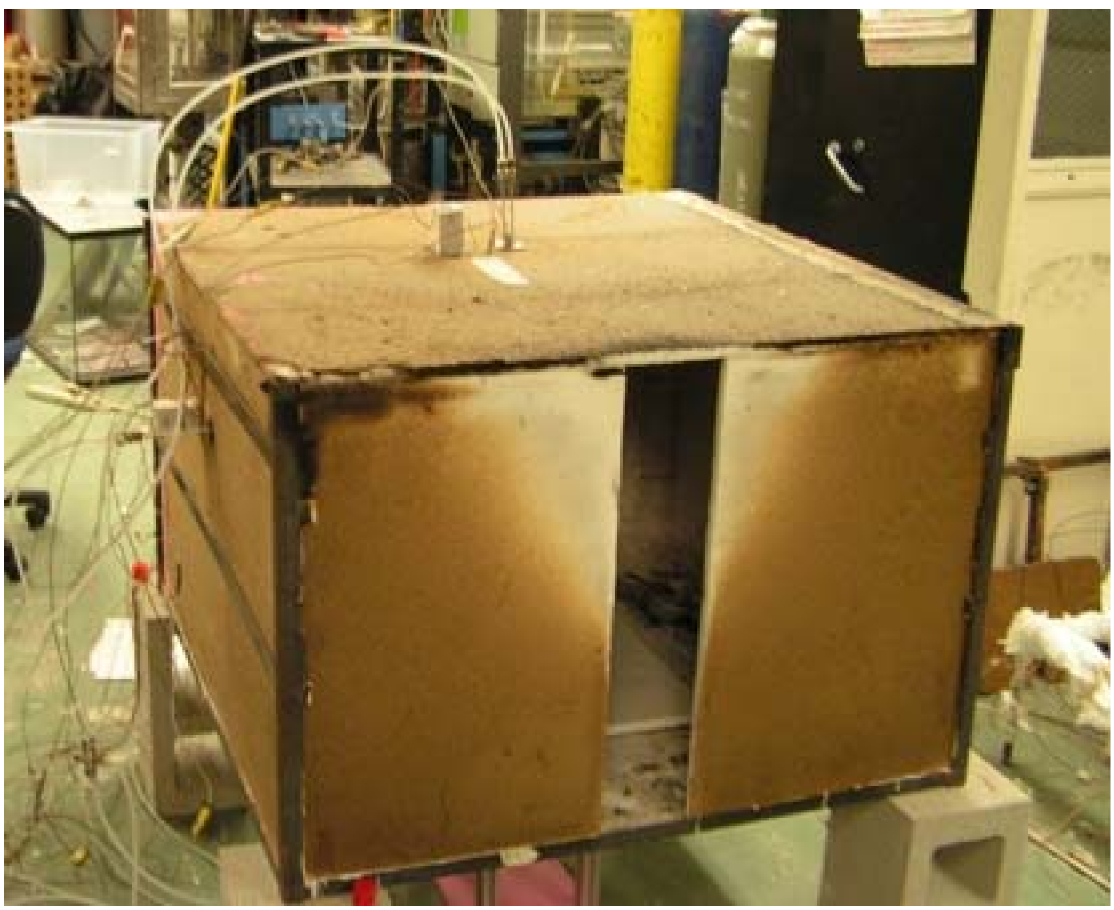
Figure 4.15: Left and Ceiling Sensor Setup - 1/4 Scale Compartment

4.2.1 Ignition of Wood Cribs

Wood cribs were placed in an oven at 105 ^{o}C for 48 hours prior to each burn to ensure that its moisture content was as low as possible. The cribs were ignited using a heptane pool fire. This pool fire was scaled between compartments and fuel loads. For each crib a square pan was constructed which was 125% larger than the base area of the crib and 2 mm in depth. It was decided that a 0.5 mm deep heptane pool would be used for each crib as its ignition source [3]. The crib was then elevated above the lip of the fuel pan at a distance equal to the particular crib's stick thickness. Fig. 4.16 below illustrates a schematic of the wood crib, pan and crib elevator prior to a burn.

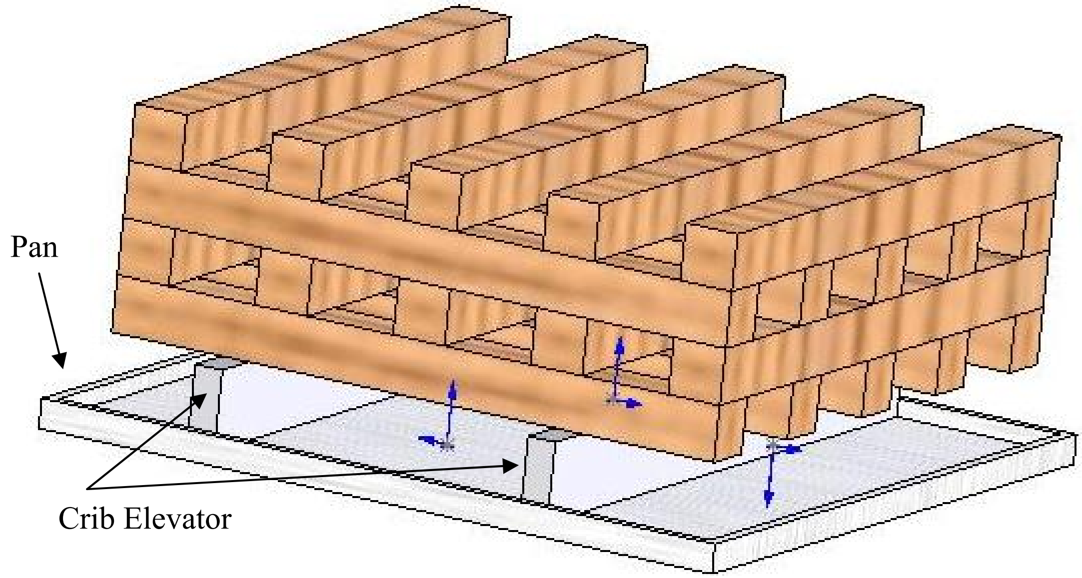

Figure 4.16: Wood Crib and Pan Pre-Burn Setup

5. RESULTS

This chapter presents and discusses results from the experiments designed in chapter 4. In the first part of this chapter, prior results are presented from work conducted by Perricone [3] to demonstrate the overall viability of new scaling theory. Following this results are shown to illustrate the repeatability of wood crib fires. Sensor data is then presented to illustrate the effectiveness of the novel metal plate sensor to differentiate between the convective and radiative heat fluxes in compartment fires. Scaling results are then presented and finally a correlation for the convective heat transfer coefficient data is derived based upon temperature rise within the compartment.

5.1 Prior Scaling Results and Data Comparisons

Before analyzing data from the experiments conducted in this thesis a brief outline of scaling results from Perricone [3] are presented. Perricone's data presents a strong argument in favor of the current scaling approach. These results then initiated further research into the scaling methodology which then became the basis for this thesis and ongoing work on scaling structures in fires. Where possible, data from tests conducted in both studies is compared to emphasize the repeatability of the wood crib fire data.

5.1.1 Free Burn Results

Before conducting compartment fire experiments a series of free burn experiments were conducted using the wood cribs designed for each scale. During these experiments the 3/8 scale was also tested as laboratory facilities provided by the ATF[b] were available. Both the small crib and large crib designs were evaluated. The experimental labeling convection adopted by Perricone [3] is outline in Table 5.1.

Table 5.1: Perricone Test Identification

Test	Description
1-L-C/F-1/2	1/8 Scale Large fire
2-L-C/F-1/2	2/8 Scale Large fire
3-L-C/F-1/2	3/8 Scale Large fire
1-S-C/F-1/2	1/8 Scale Small fire
2-S-C/F-1/2	2/8 Scale Small fire
3-S-C/F-1/2	3/8 Scale Small fire

The numerical suffix in the test labels in Table 5.1 are used to differentiate between repeated experiments. In the case where the fire is a free burn, the letter F is used instead of C which indicates a compartment burn.

Fig. 5.1 and Fig. 5.2 below plot the scaled crib free burning rate data, π_2, for the large and small fires respectively. The π_2 group has been plot against the dimensionless time, τ:

$$\tau = t\left(\frac{g}{l}\right)^{1/2} \tag{5.1}$$

[b] Bureau of Alcohol, Tobacco and Firearms

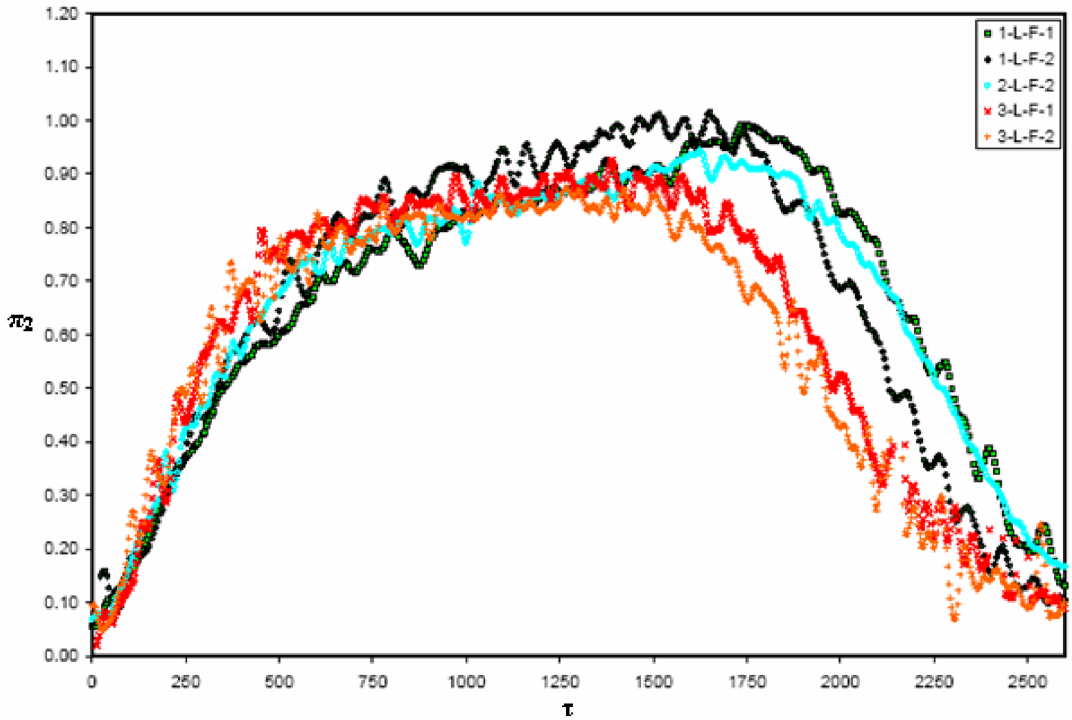

Figure 5.1: Dimensionless Free Burning Rate Results - Large Crib Design [3]

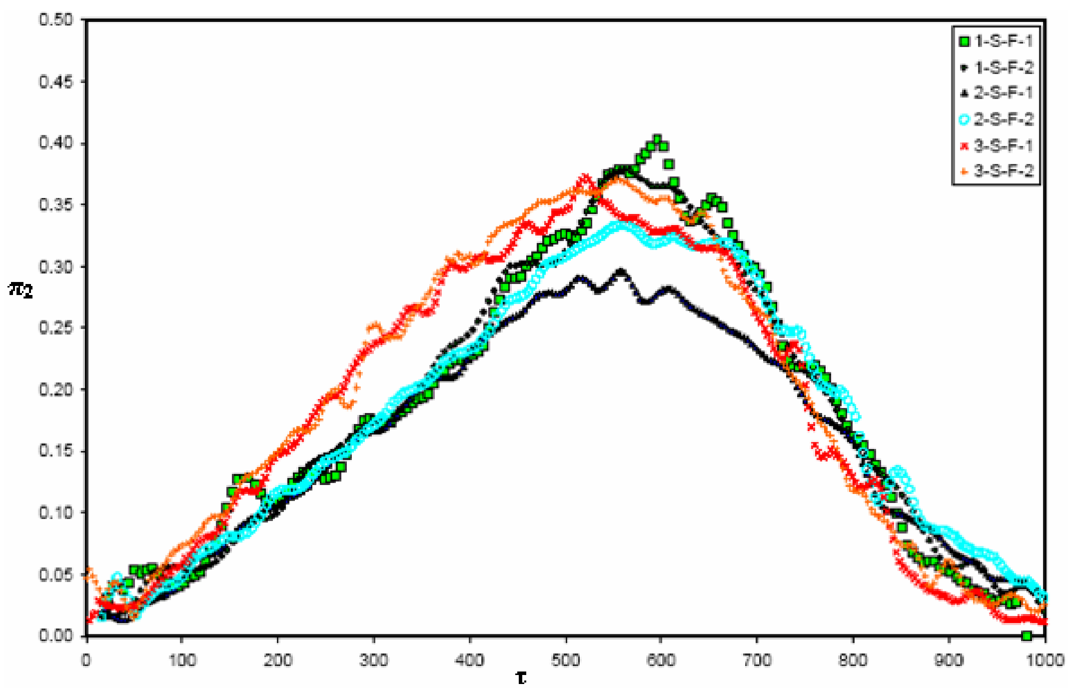

Figure 5.2: Dimensionless Free Burning Rate Results - Small Crib Design [3]

Fig. 5.1 and Fig. 5.2 show the ability of the current scaling methodology to scale the burning rate of free burning wood cribs. The free burning rates for both the small and large wood cribs have been successfully scaled between the 1/8, 1/4 and 3/8 scales.

These results also indicate that the methodology used in scaling the wood crib parameters was successful.

5.1.2 Compartment Burning Rate Data

Fig. 5.3 below plots the scaled burning rate for the large wood cribs in the compartments. As with the free burn data the π_2 group at each scale has been plot against the dimensionless time, τ.

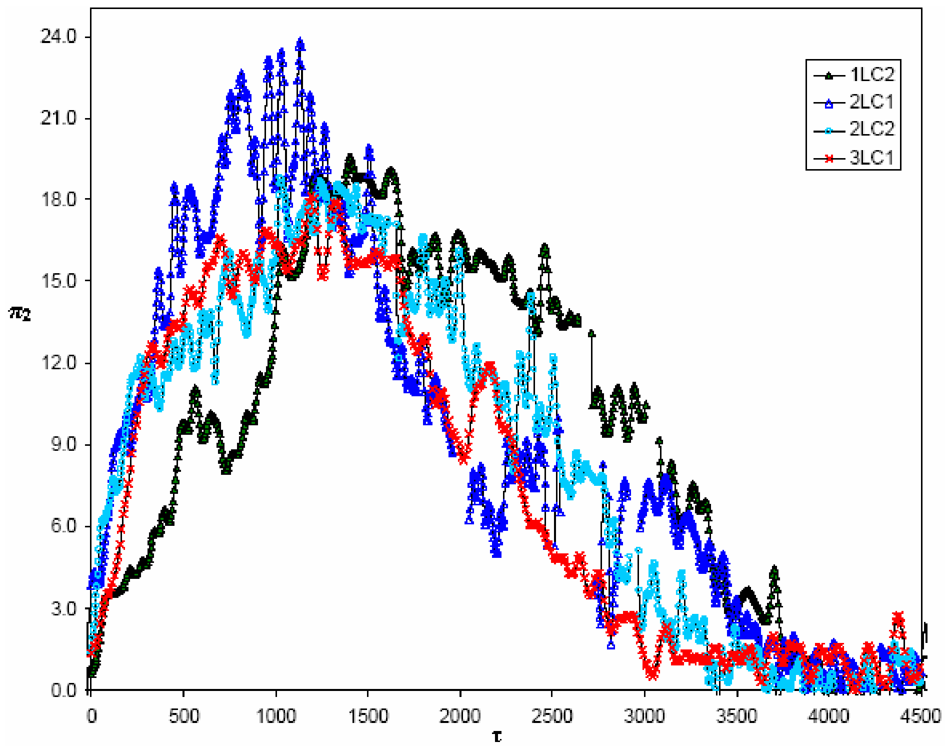

Figure 5.3: Dimensionless Compartment Burning Rate Results - Large Crib Design [3]

From Fig. 5.3 it is concluded that the transient burning rate behavior of the wood cribs in compartments has been scaled. There is some variation in the scaled burning rate behavior between the three scales which is due to the uneven ignition characteristics of the cribs.

5.1.3 Compartment Species Concentration

Fig. 5.4 and Fig. 5.5 below, plot scaled upper layer O_2 for the small and large fires against dimensionless time. Since species concentration does not scale, Eq. 2.44, the concentration of O_2 is expected to be constant between scales.

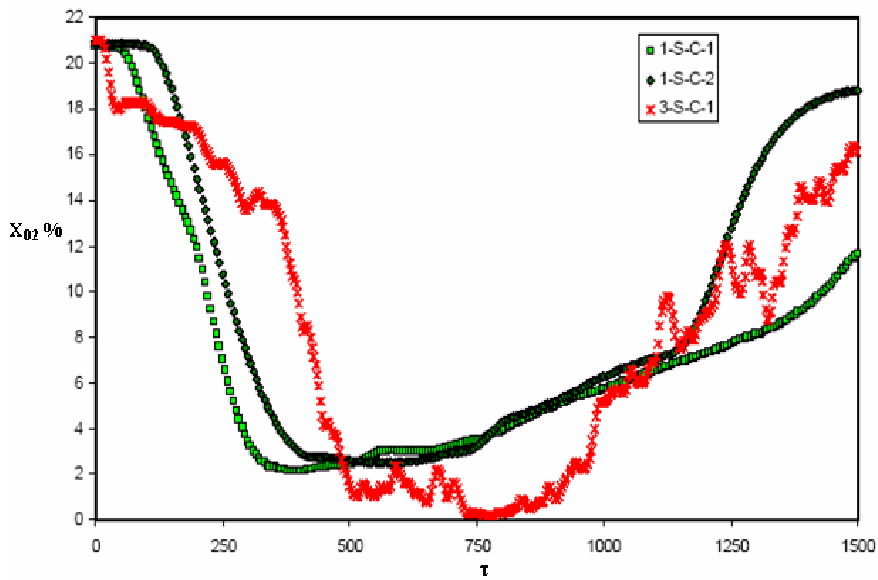

Figure 5.4: Small Crib Design, Upper Layer O_2 [3]

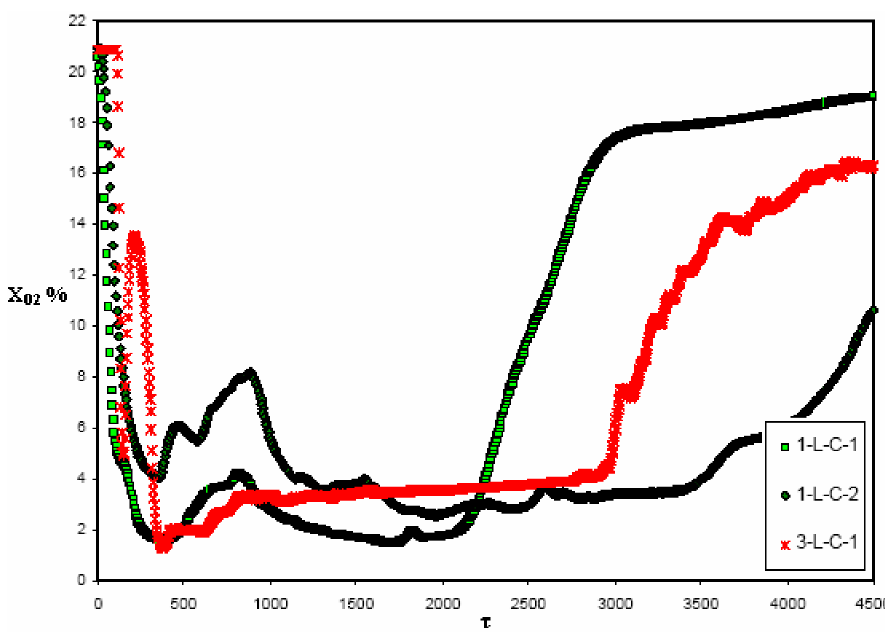

Figure 5.5: Large Crib Design, Upper Layer O_2 [3]

Fig. 5.4 and Fig. 5.5 both indicate agreement in O_2 concentration between the 1/8 and 3/8 scales. Both plots also indicate the transition of the fire to ventilation limited conditions and extinction at similar times. Therefore the transient behavior of the species concentration appears to have been preserved between scales.

5.1.4 Gas Temperature Data Repeatability

Temperature data collected at identical locations from both Perricone's data and current test data are plot in Fig. 5.7 to Fig. 5.14 below. In the plot legend the suffix '-[3]' denotes data from Perricone [3], all other data has been collected during tests conducted for this thesis. The fluctuations visible between the data sets were caused by a thinner type thermocouple wire used by Perricone.

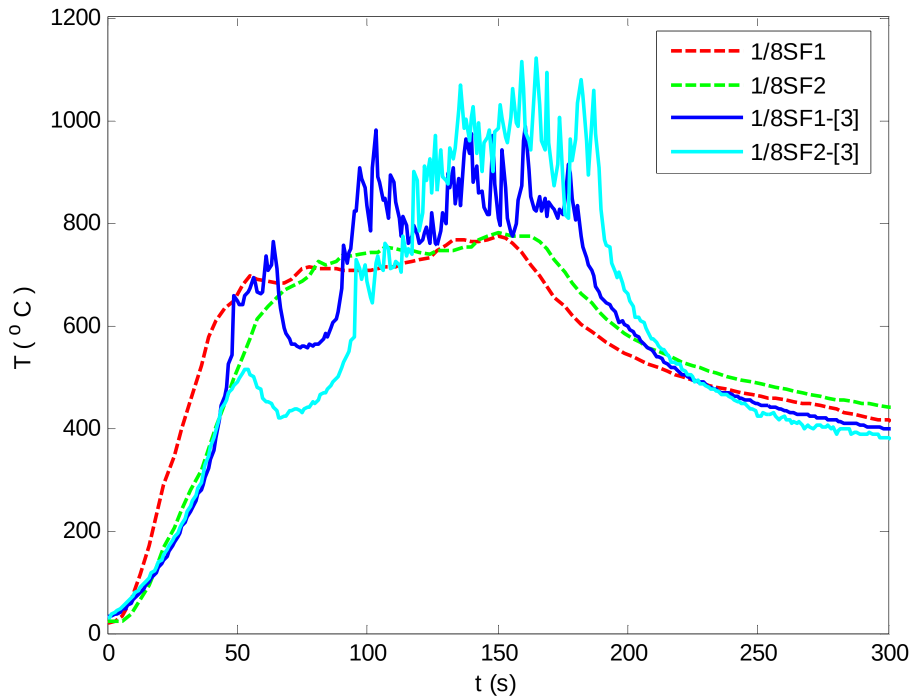

Figure 5.6: Data Comparison - 1/8 Scale Small Fire (0.44D, 0, 0.65H) Gas Temperature

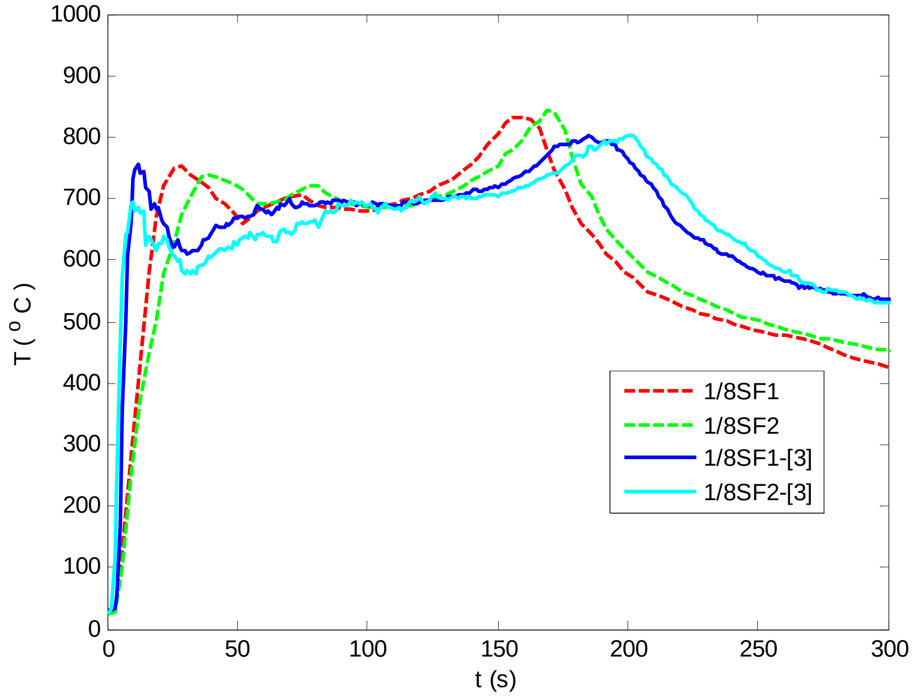

Figure 5.7: Data Comparison - 1/8 Scale Small Fire (0.44D, 0.37W, H) Gas Temperature

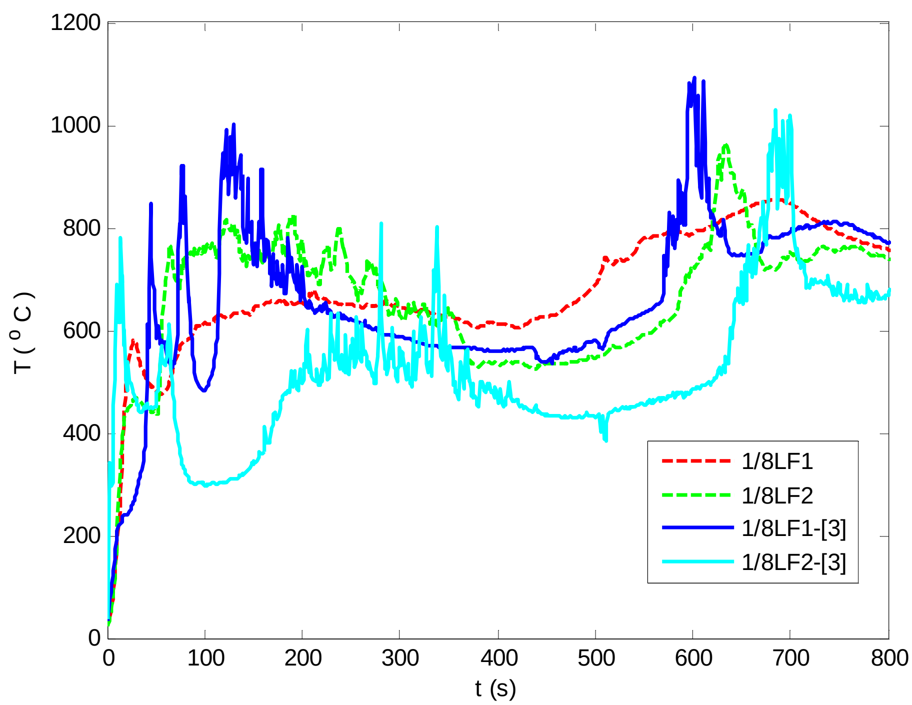

Figure 5.8: Data Comparison - 1/8 Scale Large Fire (0.44D, 0, 0.65H) Gas Temperature

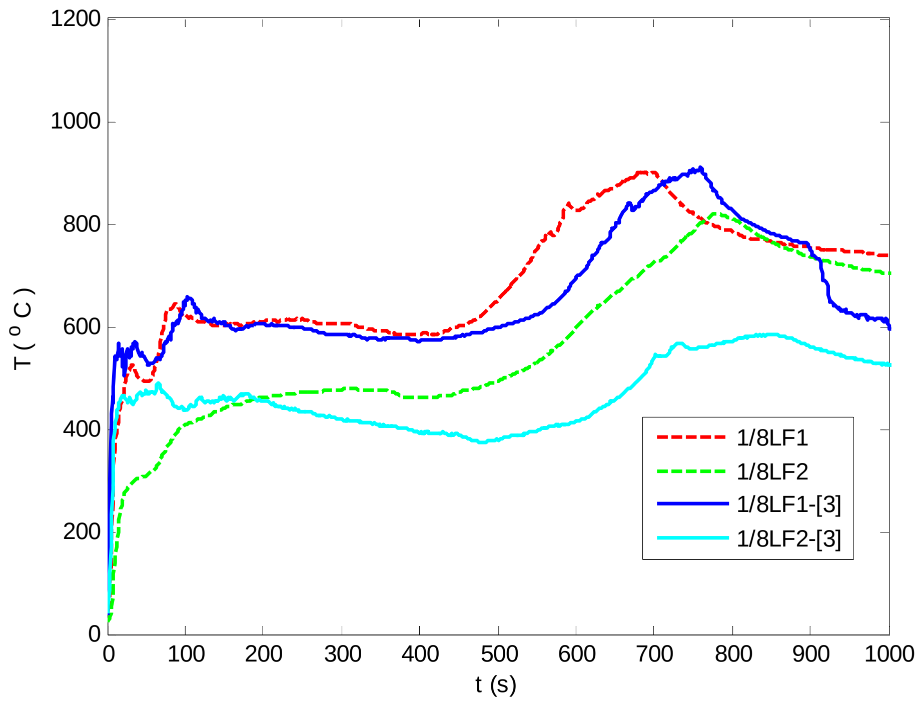

Figure 5.9: Data Comparison - 1/8 Scale Large Fire (0.44D, 0.37W, H) Gas Temperature

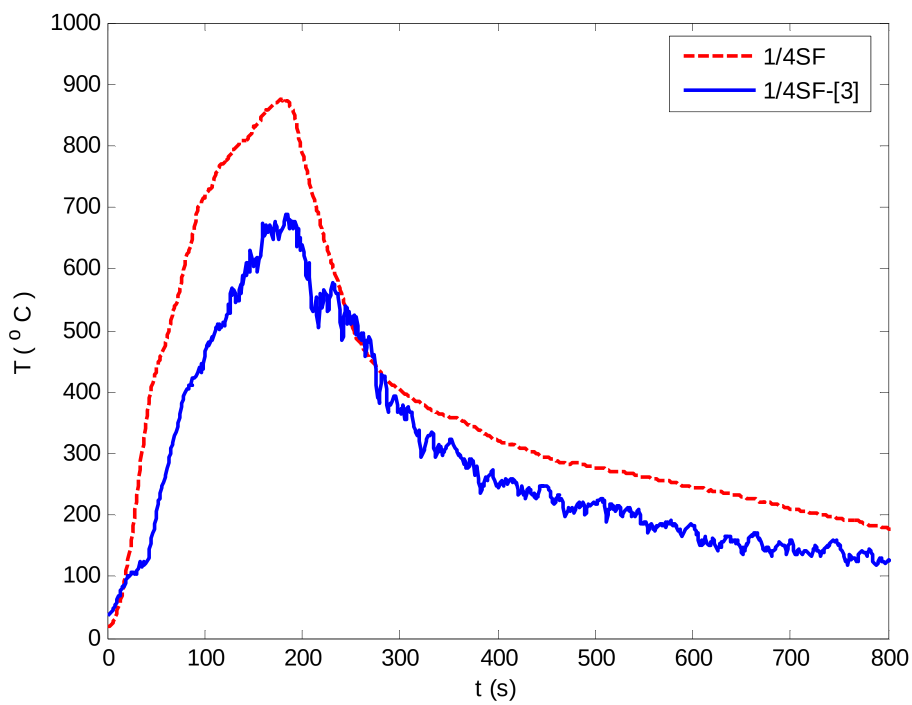

Figure 5.10: Data Comparison - 1/4 Scale Small Fire (0.44D, 0W, 0.65H) Gas Temperature

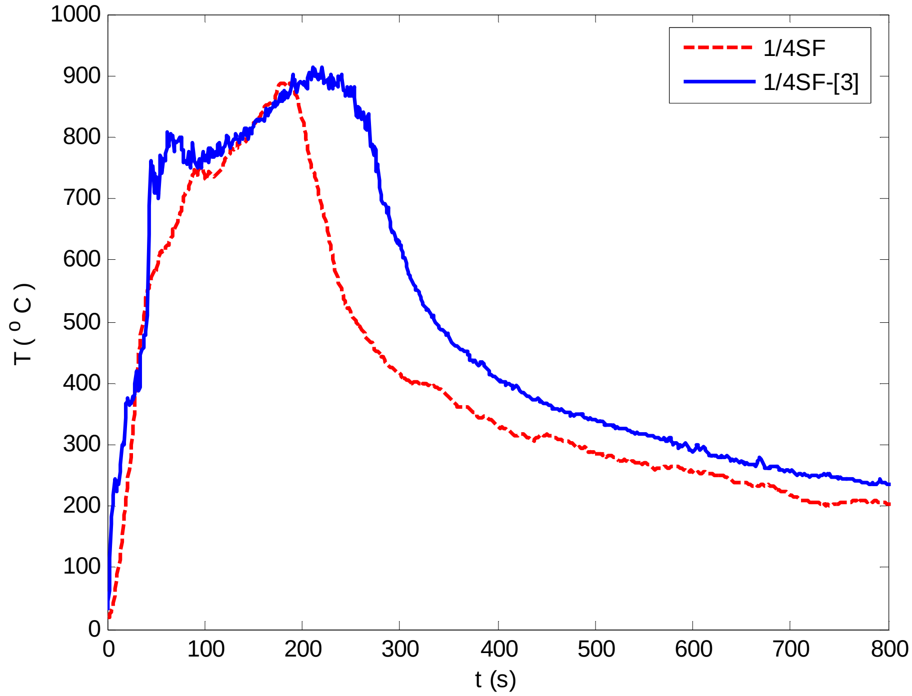

Figure 5.11: Data Comparison - 1/4 Scale Small Fire (0.44D, 0.37W, H) Gas Temperature

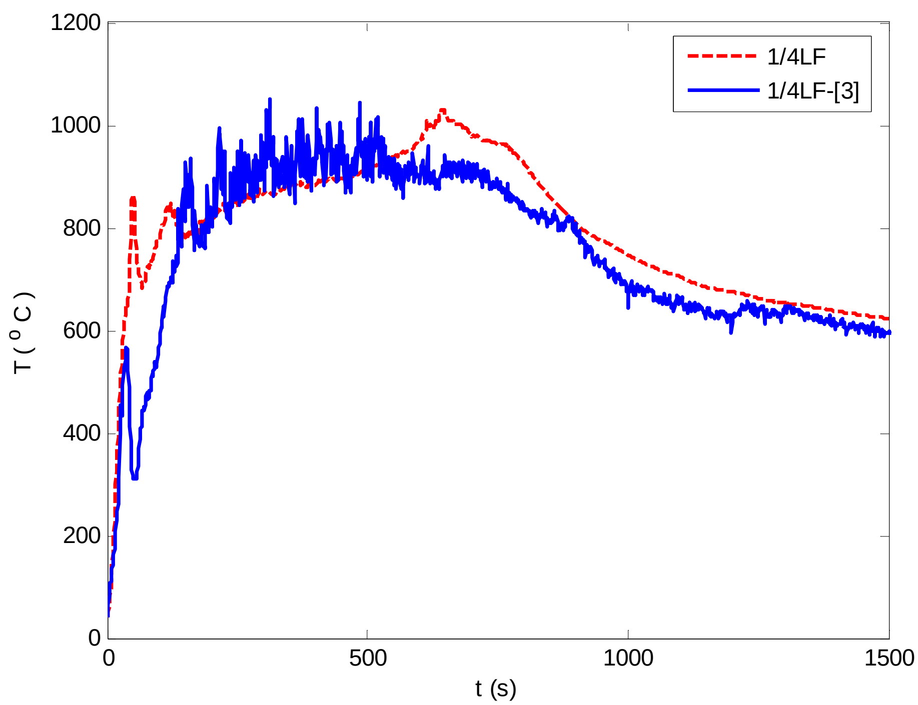

Figure 5.12: Data Comparison - 1/4 Scale Large Fire (0.44D, 0W, 0.65H) Gas Temperature

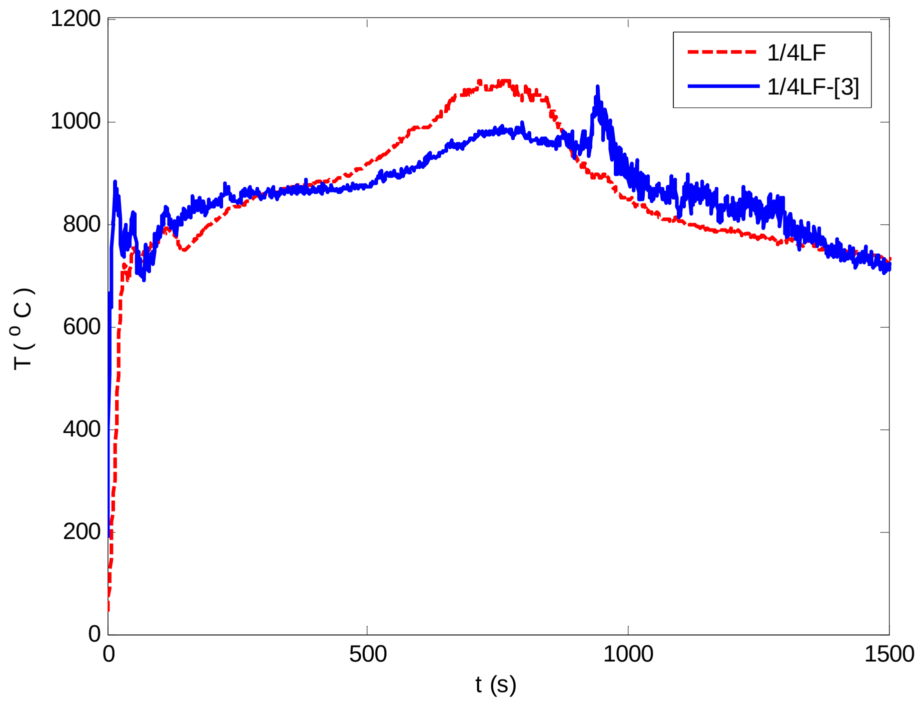

Figure 5.13: Data Comparison - 1/4 Scale Large Fire (0.44D, 0.37W, H) Gas Temperature

There is some variation for short time periods in the temperature data between repeated experiments. A possible reason for these temperature variations was the warping of the pan used to ignite the wood cribs. Warping caused an uneven distribution of the igniter liquid which in turn varied the ignition characteristics of wood cribs between repeat tests. This then lead to the variations seen in the temperature data of repeat tests above. Overall though, there is very good agreement between repeated wood crib fire temperature data.

5.1.5 Mass Loss Rate Repeatability

Variations again seen below in the mass loss rate between identical test, in Fig. 5.15 and Fig. 5.16, are most likely due to uneven ignition characteristics of the wood cribs.

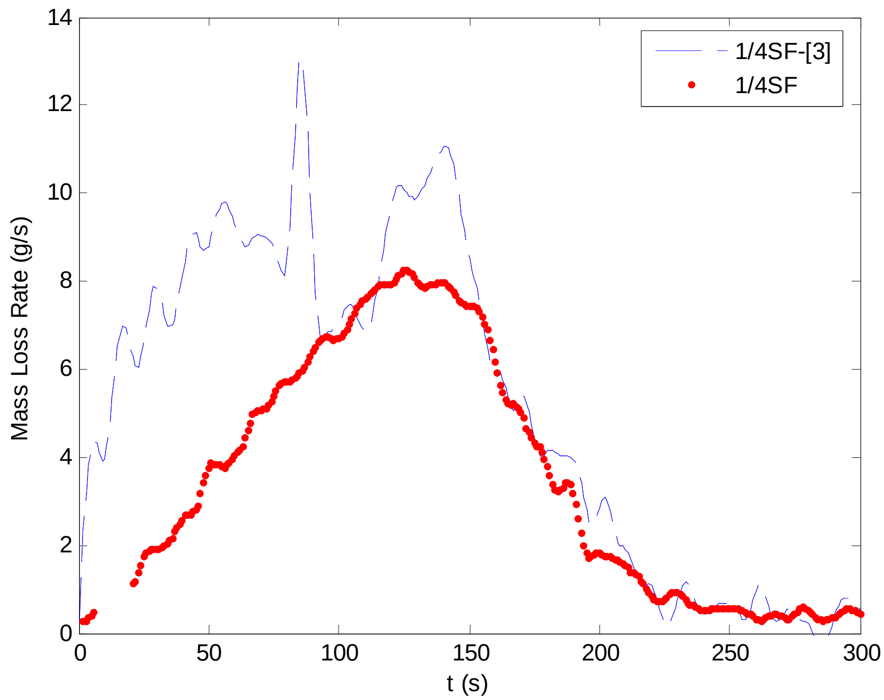

Figure 5.14: Data Comparison - 1/4 Scale Small Fire Mass Loss Rate

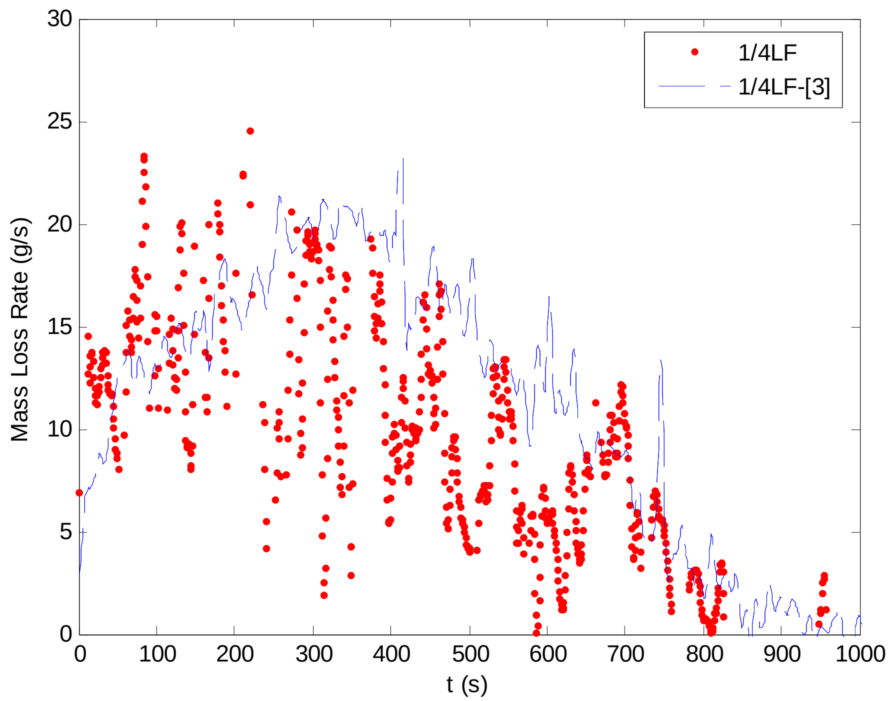

Figure 5.15: Data Comparison - 1/4 Scale Large Fire Mass Loss Rate

The burning rate comparison plots, Fig. 5.14 and Fig. 5.15, illustrate the repeatability of burning rate from wood crib fires however care needs to be taken in the ignition of the cribs to ensure even ignition.

Sections 5.1.4 and 5.1.4 give a clear indication that wood crib fires and hence their data are repeatable.

5.2 Compartment Measured Convective and Radiative Flux Data

This section illustrates the process whereby the convective and radiative components of a compartment fire can be differentiated through the use of metal plate sensor and heat flux gauge data.

The metal plate sensor measured flux in a compartment fire is given by Eq. 3.36. Using the compartment fire metal plate sensor time response, Eq. 3.38, the metal plate sensor measured flux can be corrected:

$$t_{r,fire}\frac{d\dot{q}''_m}{dt}+\dot{q}''_m=\dot{q}''_{m,crr} \tag{5.2}$$

The corrected metal plate sensor measured heat flux, Eq. 5.2, is equal to the total incident radiation and convection heat flux from the compartment fire to the metal plate sensor:

$$\dot{q}''_{m,crr}=\dot{q}''_{fire,r}+h_{fire,c}\left(T_g-T_m\right) \tag{5.3}$$

The heat flux gauge measures incident convective and radiative flux from the fire to a surface at room temperature:

$$\dot{q}''_{HFG}=\dot{q}''_{fire,r}+h_{fire,c}\left(T_g-T_\infty\right) \tag{5.4}$$

The difference between the heat flux gauge measured flux, Eq. 5.4, and the metal plate sensor measured flux, Eq. 5.3, gives the convective heat transfer coefficient:

$$h_{fire,c}=\frac{\dot{q}''_{HFG}-\dot{q}''_{m,crr}}{\left(T_m-T_\infty\right)} \tag{5.5}$$

Once the convective heat transfer coefficient is calculated both the convective and radiative heat flux from the compartment fires can be calculated by rearranging either Eq. 5.3 or Eq. 5.4. Fig. 5.17 to Fig. 5.19 illustrates the difference in between the heat flux gauge and the metal plate sensor measured flux.

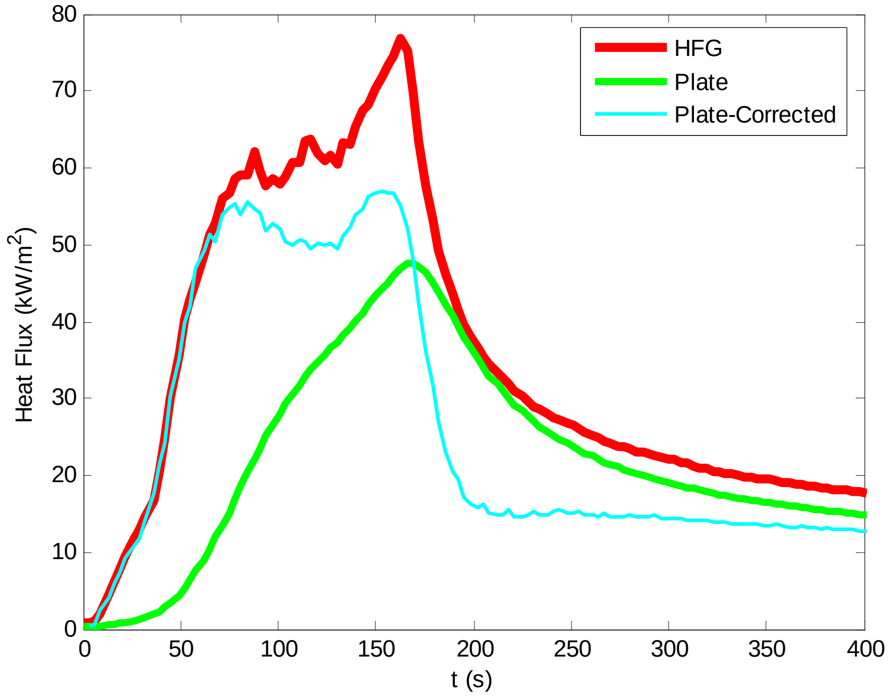

Figure 5.16: 1/8 Scale Small Fire – (0.55D, W, 0.65H) Measured Heat Flux

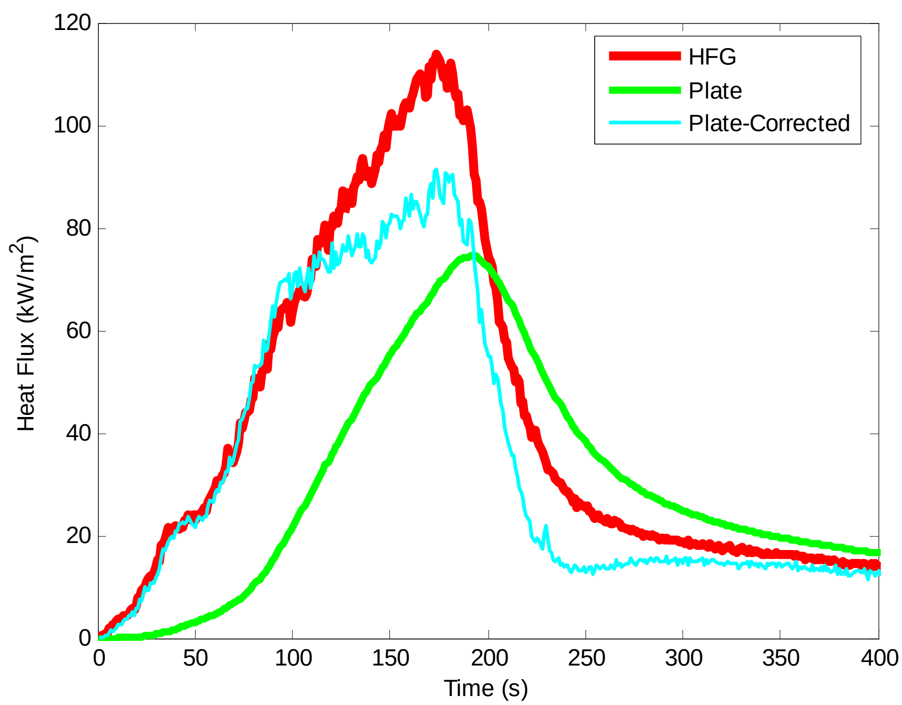

Figure 5.17: 1/4 Scale Small Fire - (0.44D, W, 0.65H) Measured Heat Flux

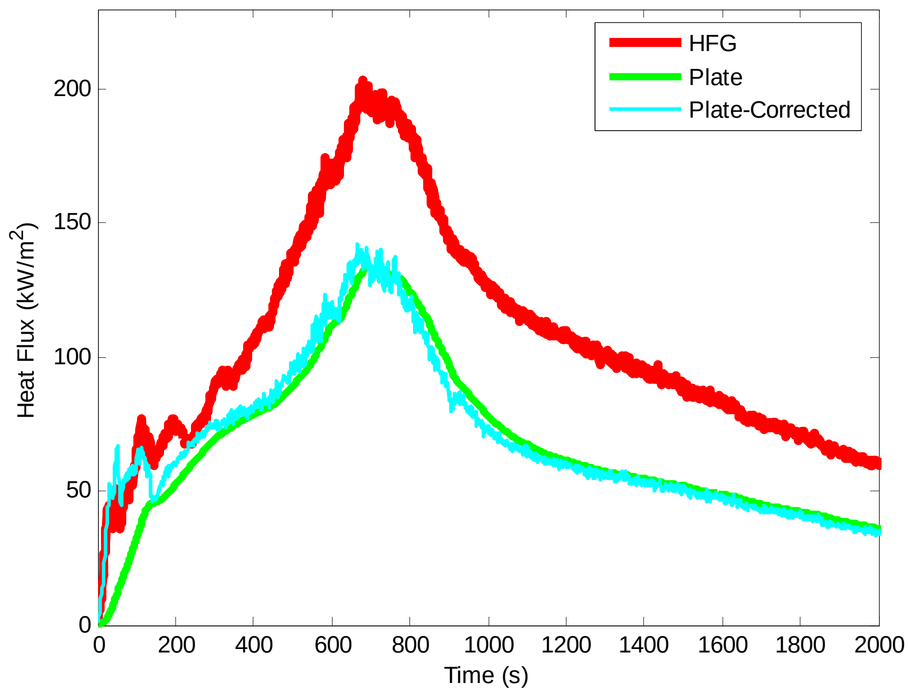

Figure 5.18: 1/4 Scale Large Fire - (0.44D, 0.37W, H) Measured Heat Flux

5.1.1 Convective Heat Transfer Coefficient

Using Eq. 5.5 the convective heat transfer coefficient data from each compartment is plot below. Fig. 5.20 to Fig. 5.22 below plot the convective coefficient for the 1/8 scale small fires at the various specified sensor locations.

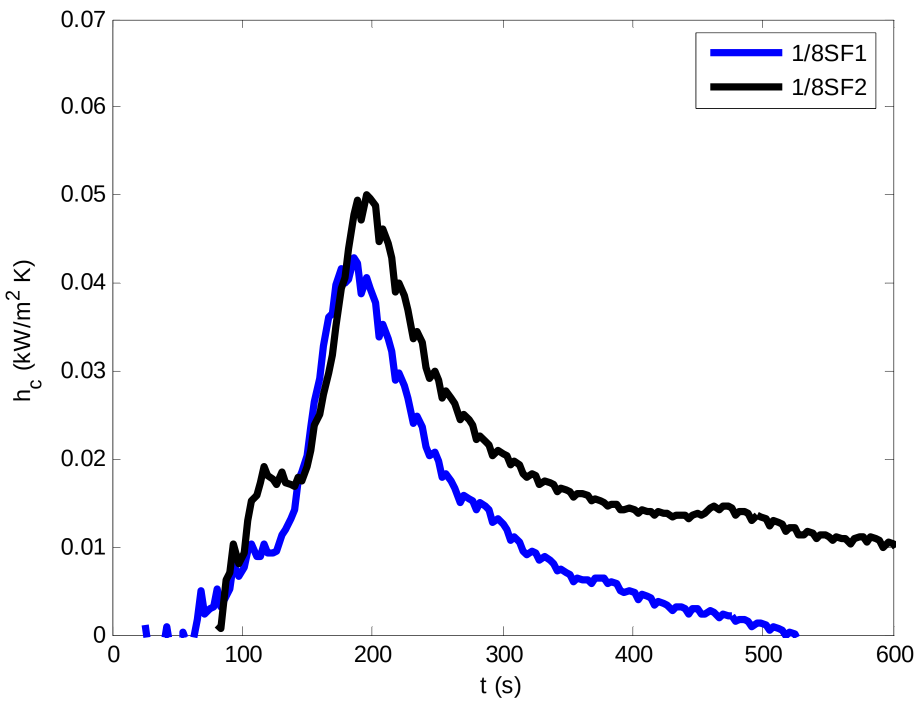

Figure 5.19: 1/8 Scale Small Fire - (0.55D, W, 0.65H) Convective Heat Transfer Coefficient

In Fig. 5.20 to Fig. 5.22 the convective heat transfer coefficient value peaks at the maximum gas temperature within the compartment. There is some difficulty in resolving the convective heat transfer coefficient data during the early stages of the fire. There is also a high level of repeatability in the data between consecutive tests,

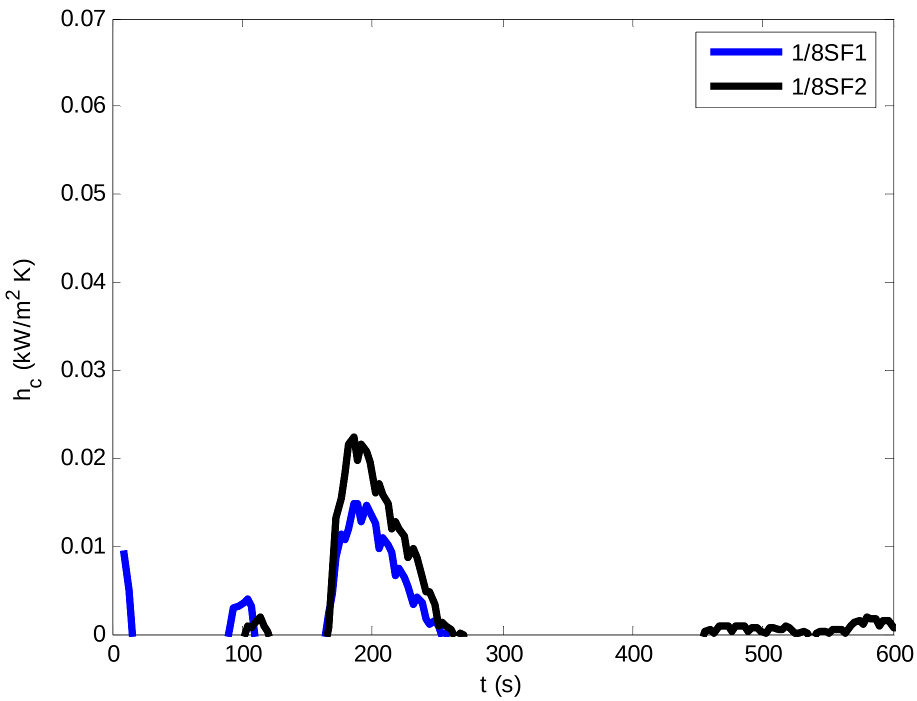

Figure 5.20: 1/8 Scale Small Fire - (0, 0.55W, 0.2H) Convective Heat Transfer Coefficient

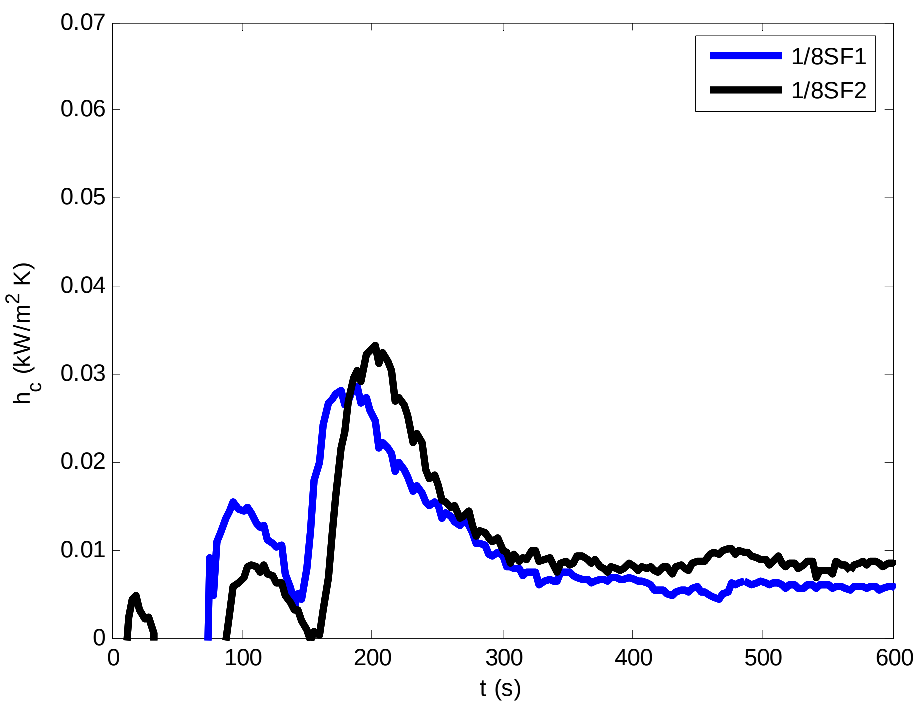

Figure 5.21: 1/8 Scale Small Fire - (0.44D, 0.37W, H) Convective Heat Transfer Coefficient

Fig. 5.23 to Fig. 5.25 below plot the convective heat transfer coefficient for the 1/4 scale small fires and Fig. 5.26 and Fig. 5.27 for the 1/4 scale large fires.

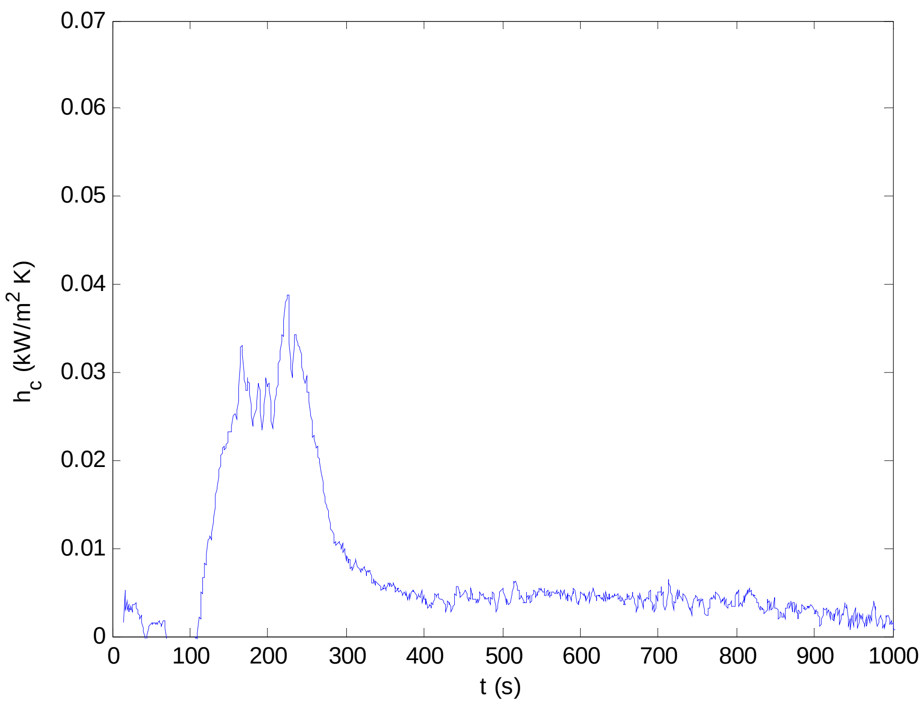

Figure 5.22: 1/4 Scale Small Fire - (0.44D, 0, 0.65H) Convective Heat Transfer Coefficient

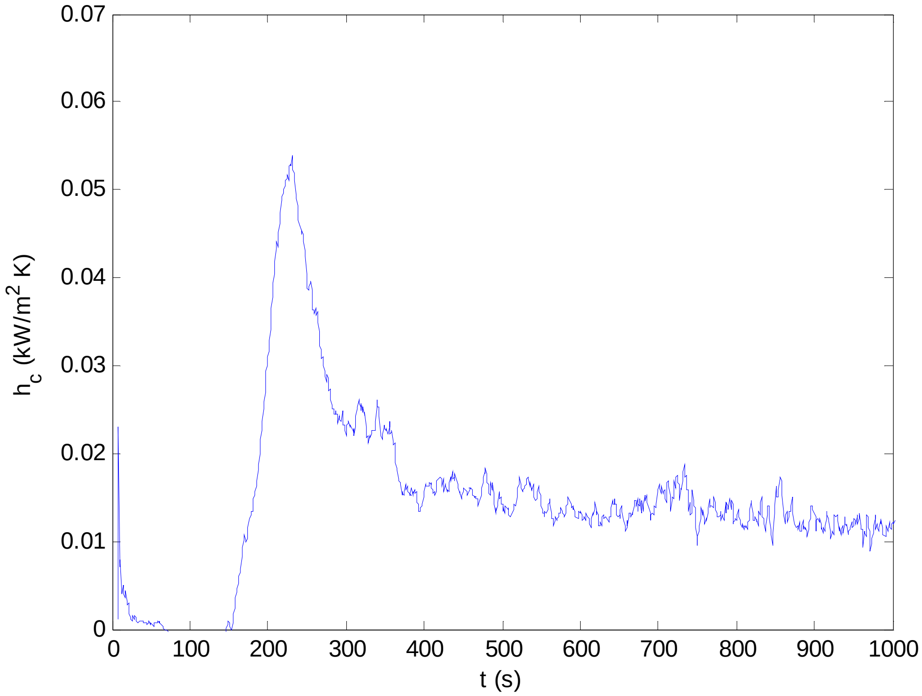

Figure 5.23: 1/4 Scale Small Fire - (0, 0.55W, 0.2H) Convective Heat Transfer Coefficient

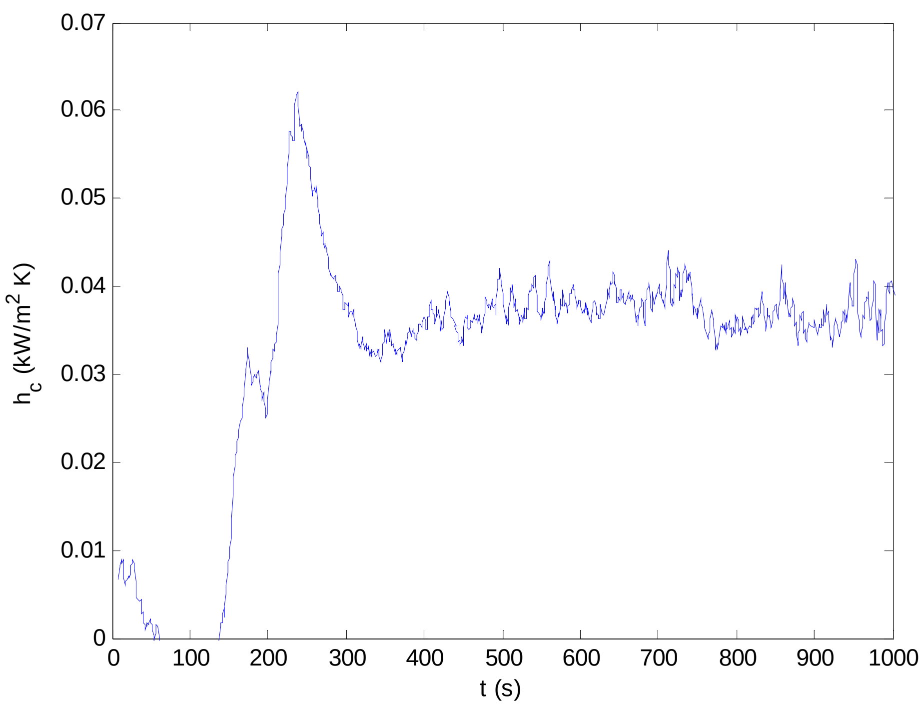

Figure 5.24: 1/4 Scale Small Fire - (0.44D, 0.37W, H) Convective Heat Transfer Coefficient

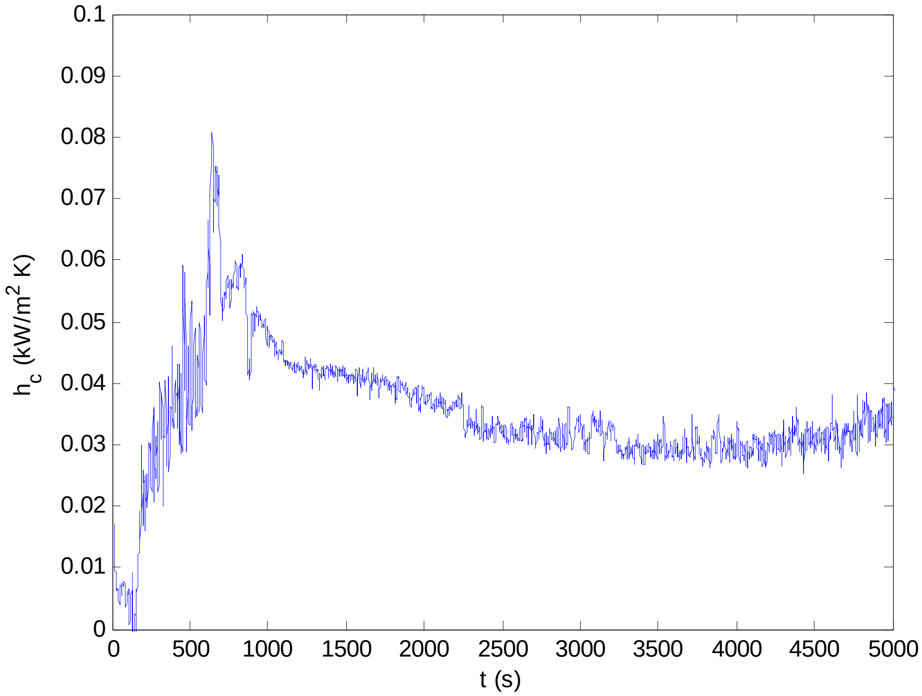

Figure 5.25: 1/4 Scale Large Fire – (0, 0.55W, 0.2H) Convective Heat Transfer Coefficient

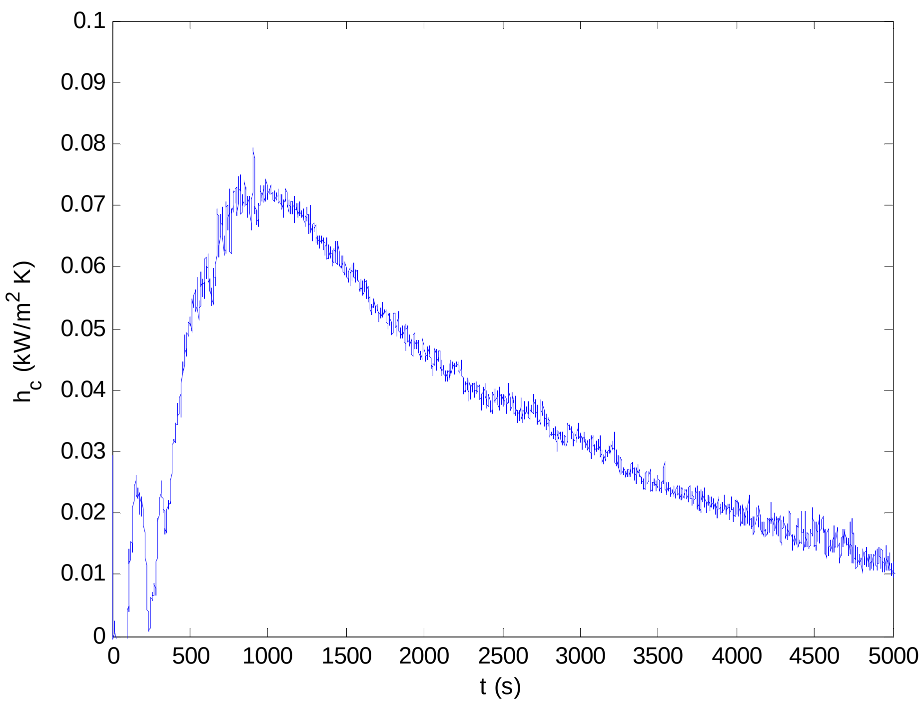

Figure 5.26: 1/4 Scale Large Fire - (0.44D, 0.37W, H) Convective Heat Transfer Coefficient

As seen with the convective heat transfer coefficient data measured in the 1/8 scale compartment fires the 1/4 scale data for both the large and small fires peaks when the maximum temperature is recorded in the compartment.

5.3 Scaling Results

5.3.1 Gas Temperature

The scaling theory states that gas temperature between homologous locations for compartment fires scales as:

$$T \sim l^0 \tag{5.6}$$

Temperature data for the small and large crib fires at the various sensor locations is plot below. Fig. 5.28 to Fig. 5.30 plots the scaled gas temperature data from the small fires and Fig. 5.31 to Fig. 5.33 the scaled gas temperature data from the large fires. Where possible Perricone's data [3] is overlaid on the current data and differentiated using the same suffix notation used earlier in the chapter. The x-axis is dimensionless time as define in Eq. 5.1.

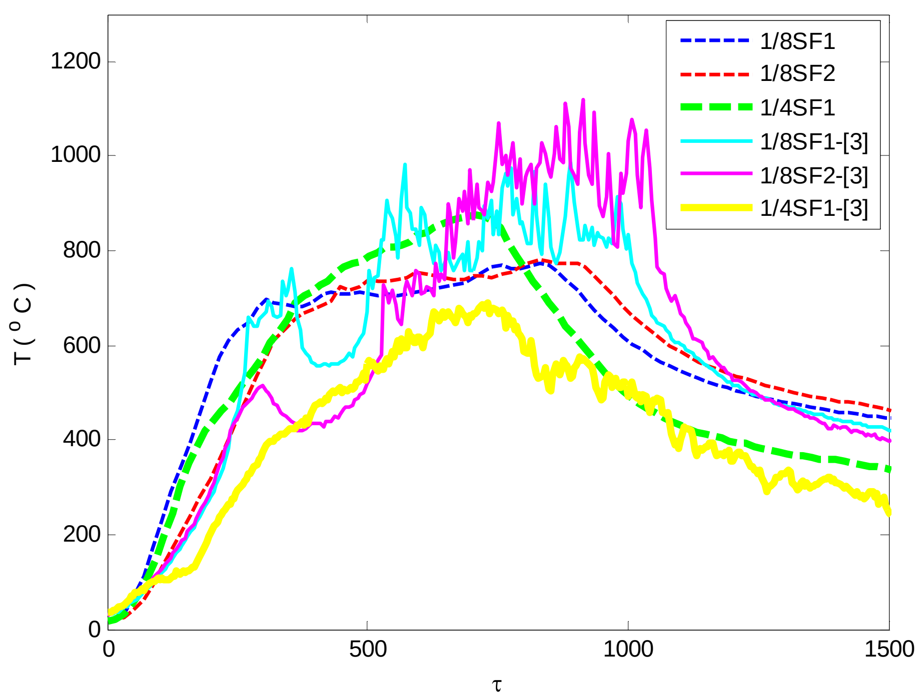

Figure 5.27: Small Fire - (0.44D, 0, 0.65H) Scaled Gas Temperature

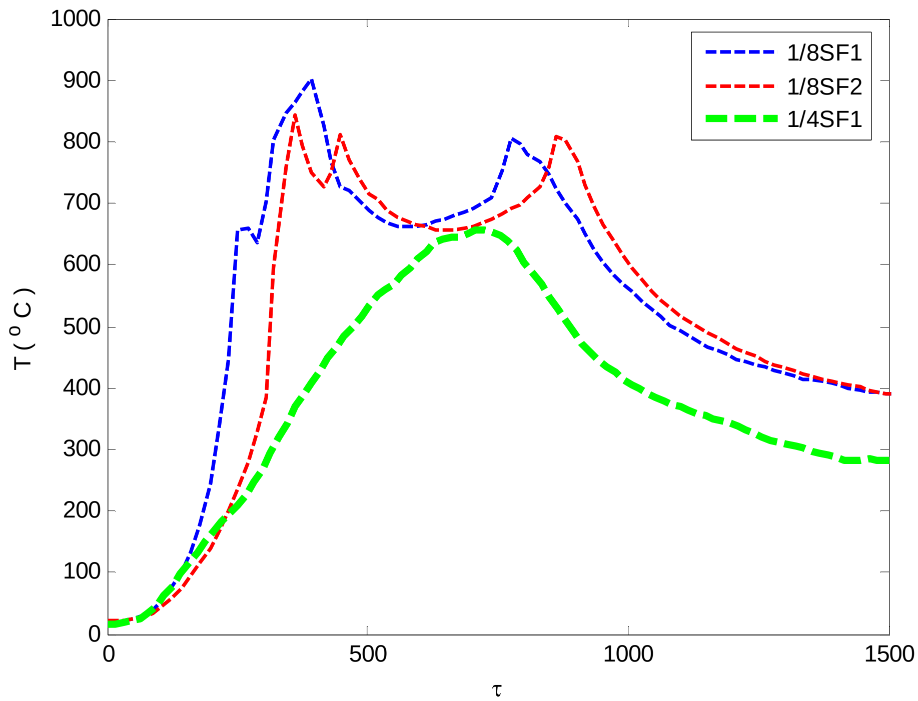

Figure 5.28 Small Fire - (0, 0.55W, 0.2H) Scaled Gas Temperature

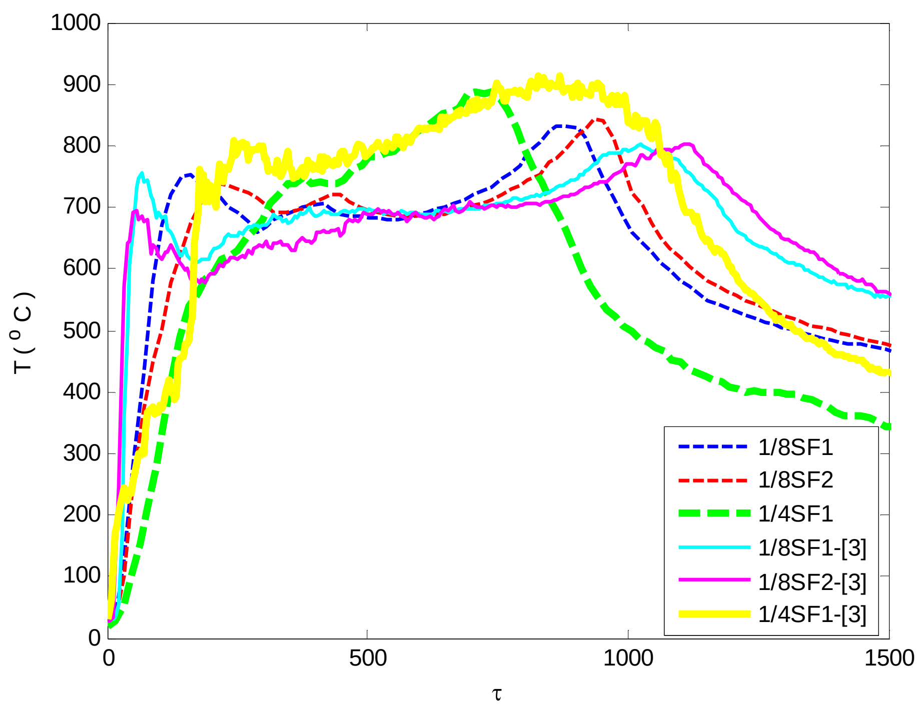

Figure 5.29: Small Fire - (0.44D, 0.37W, H) Scaled Gas Temperature

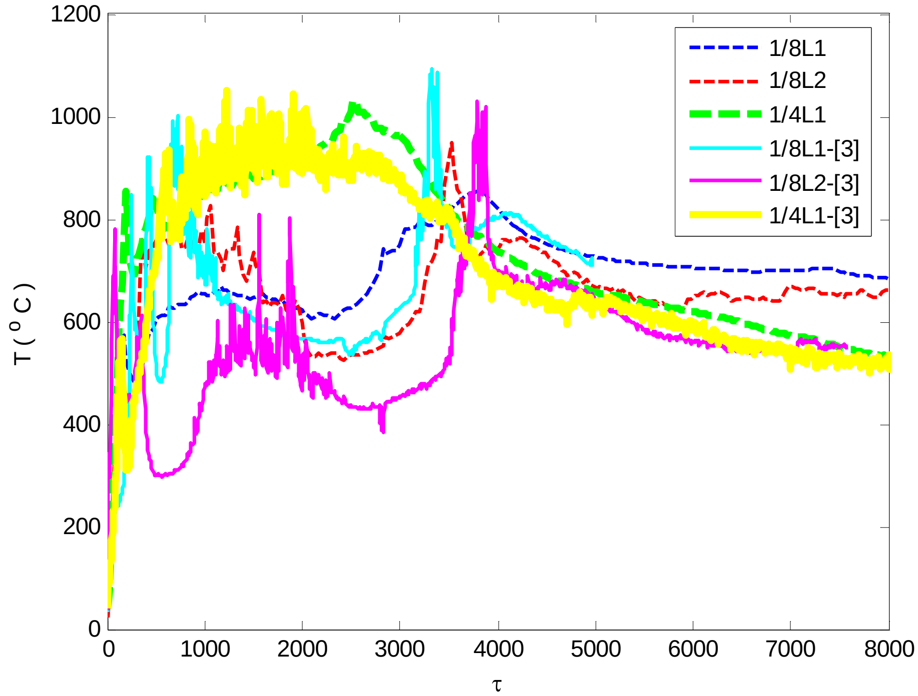

Figure 5.30: Large Fire – (0.44D, 0, 0.65H) Scaled Gas Temperature

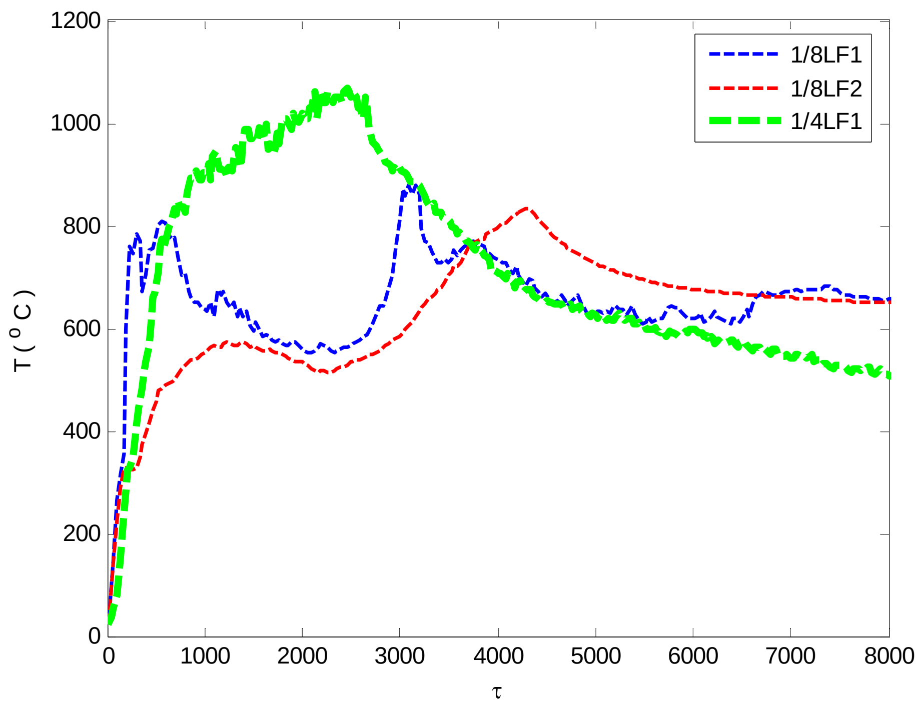

Figure 5.31: Large Fire – (0, 0.55W, 0.2H) Scaled Gas Temperature

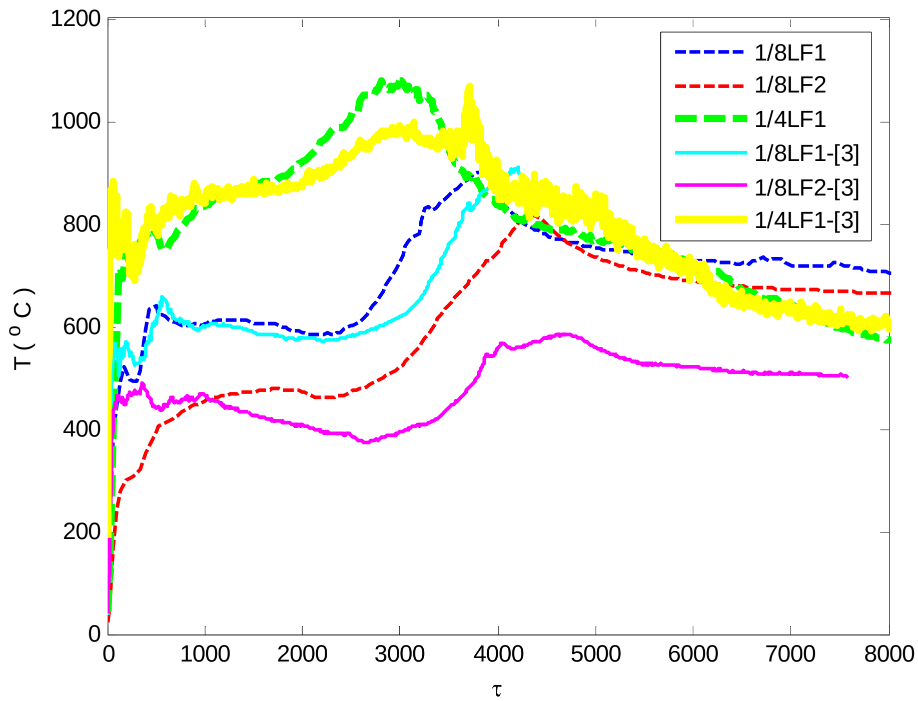

Figure 5.32: Large Fire – (0.44D, 0.37W, H) Scaled Gas Temperature

There is good overall scaling between temperature data at various locations for the various scales though there are some peak differences between the 1/8 and 1/4 scales.

5.3.2 Wall Temperature

Compartment wall temperature scaling is identical to compartment gas temperature scaling, i.e.:

$$T_w \sim l^0 \tag{5.7}$$

There was some difficulty in obtaining an accurate wall temperature for the 1/8 scale as the wall material used was an insulation blanket which had the tendency to cover the thermocouple bead during testing. This resulted in lower wall temperatures being measured at the 1/8 scale.

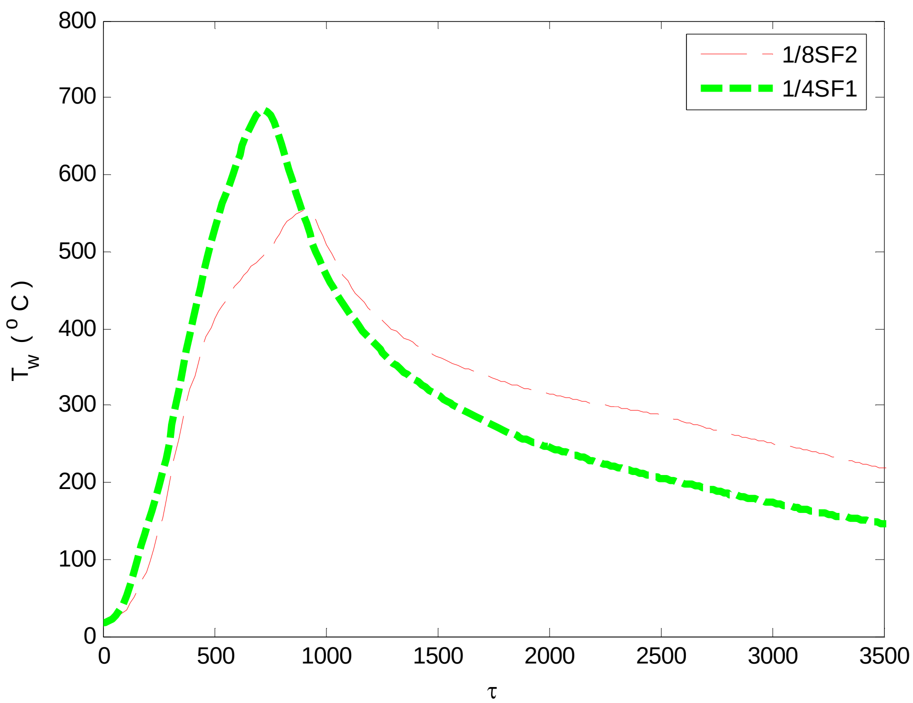

Figure 5.33: Small Fire – (0.44D, 0, 0.65H) Scaled Wall Temperature

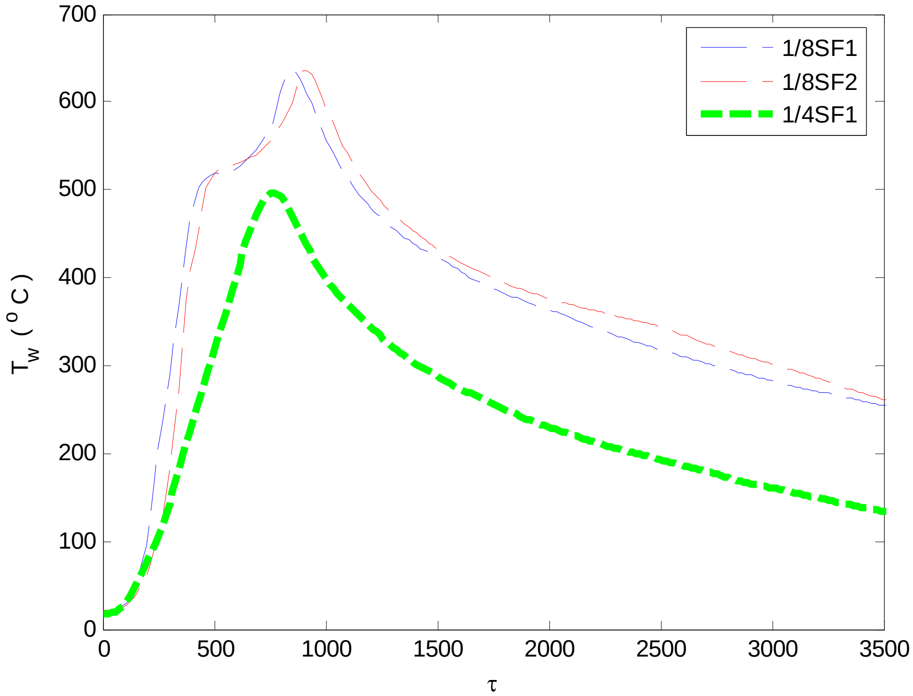

Figure 5.34: Small Fire – (0, 0.55W, 0.2H) Scaled Wall Temperature

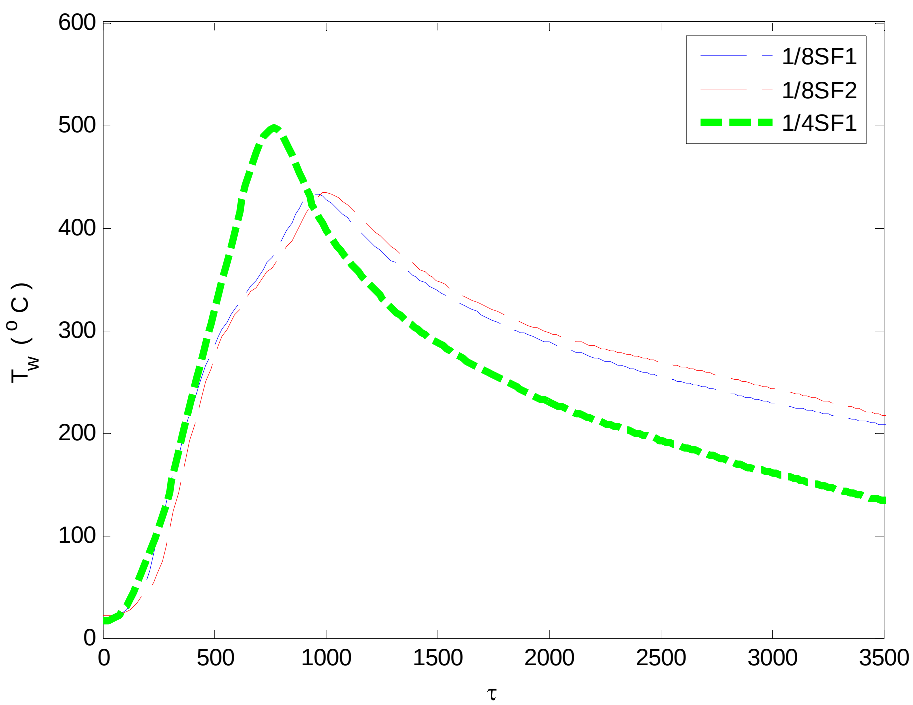

Figure 5.35: Small Fire – (0.44D, 0.37W, H) Scaled Wall Temperature

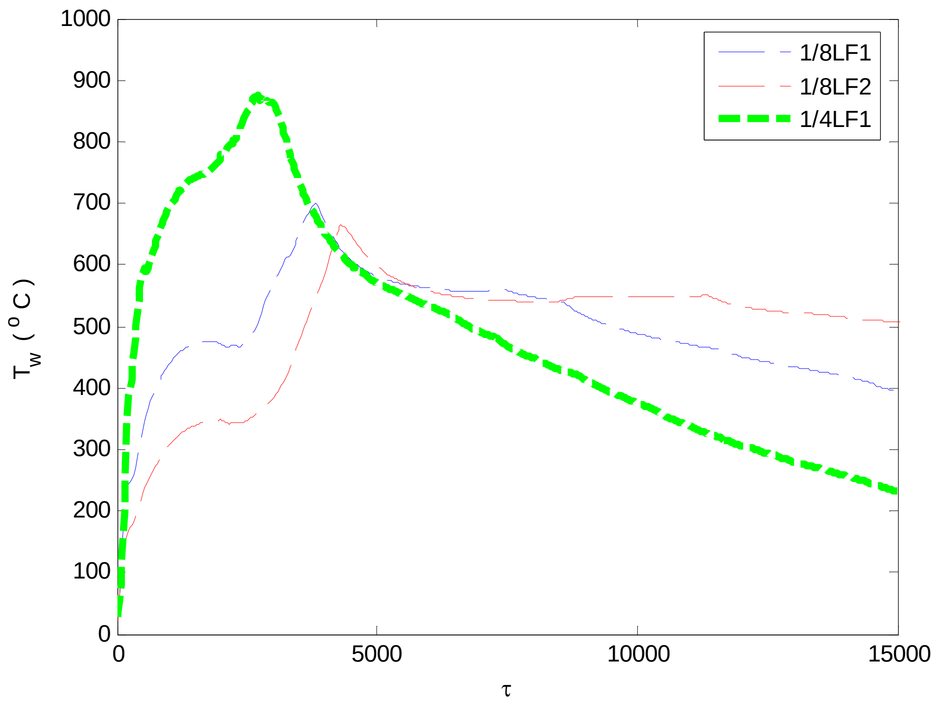

Figure 5.36: Large Fire – (0.44D, 0, 0.65H) Scaled Wall Temperature

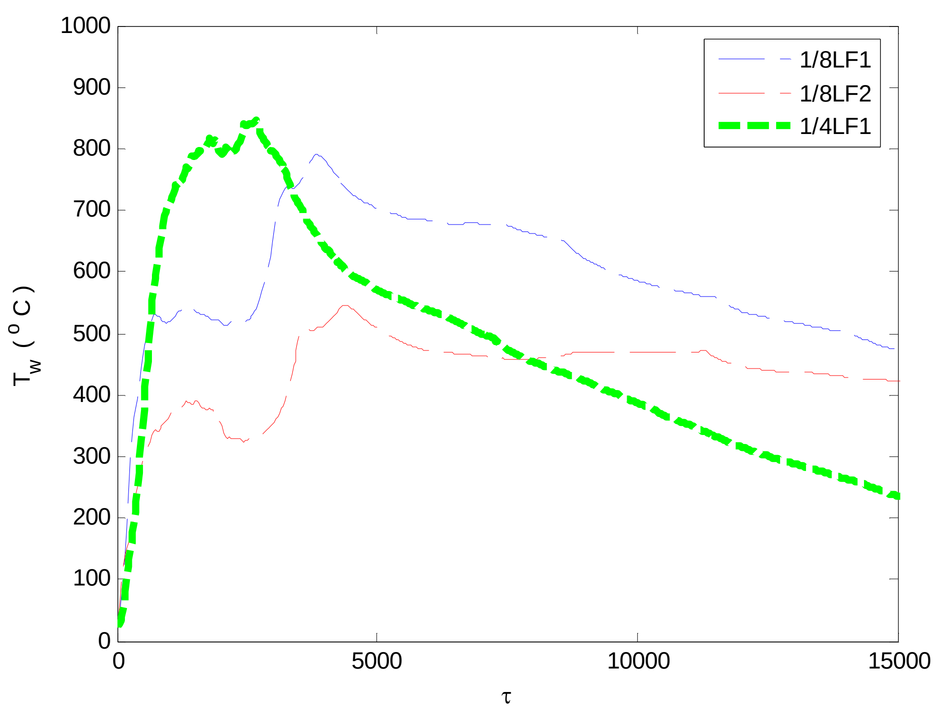

Figure 5.37: Large Fire – (0, 0.55W, 0.2H) Scaled Wall Temperature

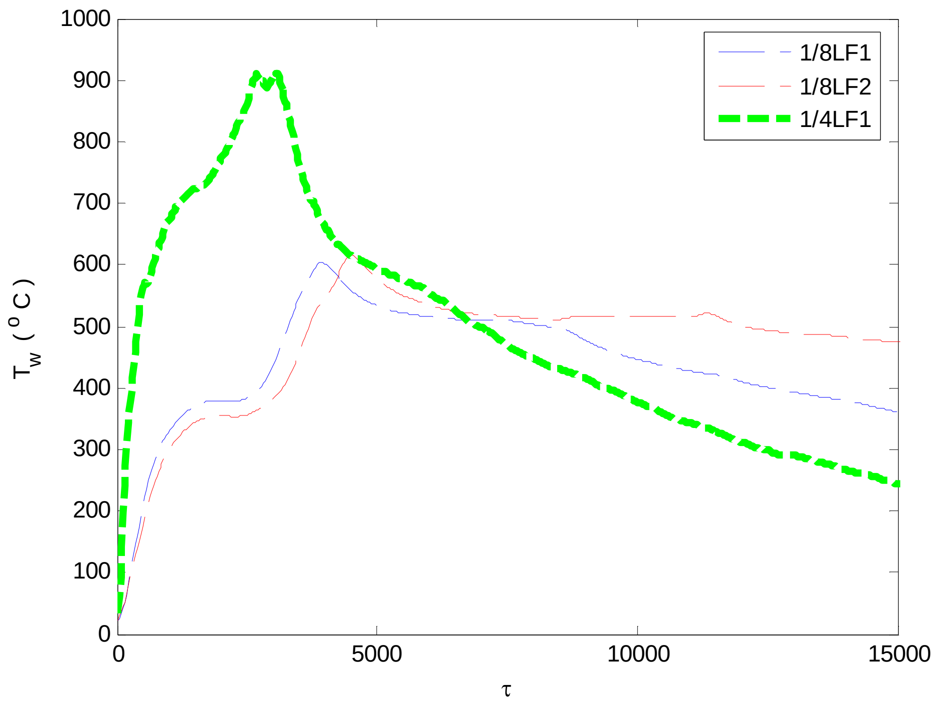

Figure 5.38: Large Fire – (0.44D, 0.37W, H) Scaled Wall Temperature

As with the gas temperature data, for the wall temperature data there are periods of good scaling between the 1/8 and 1/4 fires. Nevertheless, there are periods of significant variations between the peak temperatures of both fires. In Fig. 5.36 to Fig. 5.39 there is also a deviation from the scaling seen during the decay stage of the fire when wall temperatures recorded at the 1/8 scale is larger than the 1/4 scale wall temperature.

5.3.3 Radiation

Radiation heat transfer to the compartment walls scaled either to the zero or half power corresponding to thermally thick or thermally thin emissivity. The radiation heat transfer to the walls is calculated as:

$$\dot{q}''_{w,r} = \dot{q}''_{fire,r} - \varepsilon_w \sigma T_w^4 \tag{5.8}$$

The compartment wall emissivity is assumed to be unity. Analyzing the data it was found that radiation to the wall scaled best using the thermally thick emissivity criteria for emissivity which gives:

$$\dot{q}''_{w,r} \sim l^0 \tag{5.9}$$

Scaled small fire radiation data has been plot below in Fig. 5.40 to Fig. 5.42.

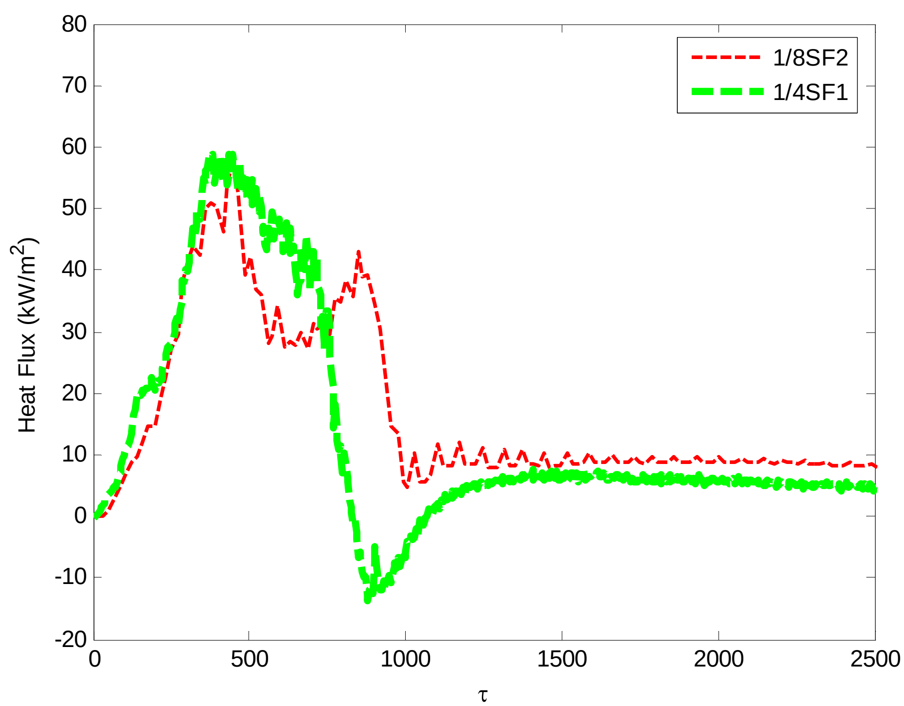

Figure 5.39: Small Fire – (0.44D, 0, 0.65H) Scaled Radiation to Wall

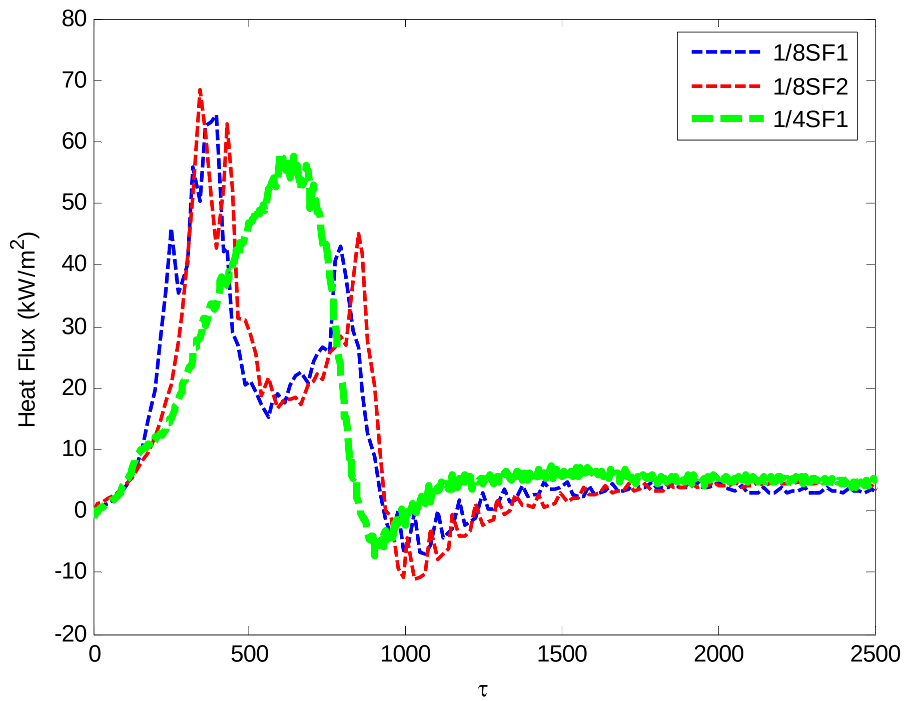

Figure 5.40: Small Fire – (0, 0.55W, 0.2H) Scaled Radiation to Wall

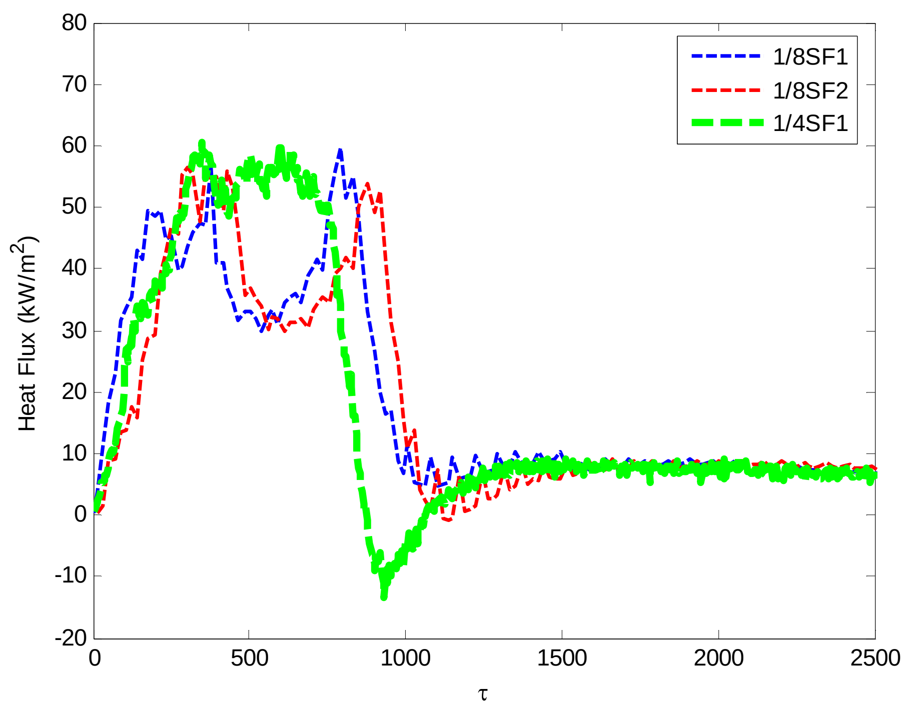

Figure 5.41: Small Fire – (0.44D, 0.37W, H) Scaled Radiation to Wall

There is very good agreement between the scaled radiation data for the small fires.

5.3.4 Convection

Convection to the compartment walls scaled either to the one fifth or half power depending on the scaling model used. Convection heat flux to the wall is calculated as:

$$\dot{q}''_{w,c} = h_{fire,c}\left(T_g - T_w\right) \tag{5.10}$$

Upon analyzing the data it was found that scaling convection as $l^{1/2}$ provided the best fit for the data relative to the $l^{1/5}$ fit. Convective heat transfer to the walls for each scale has been scaled up to full scale, i.e. $\dot{q}''_{scaled} = \frac{\dot{q}''_{w,c}}{l^{1/2}}$, where l is the compartment height.

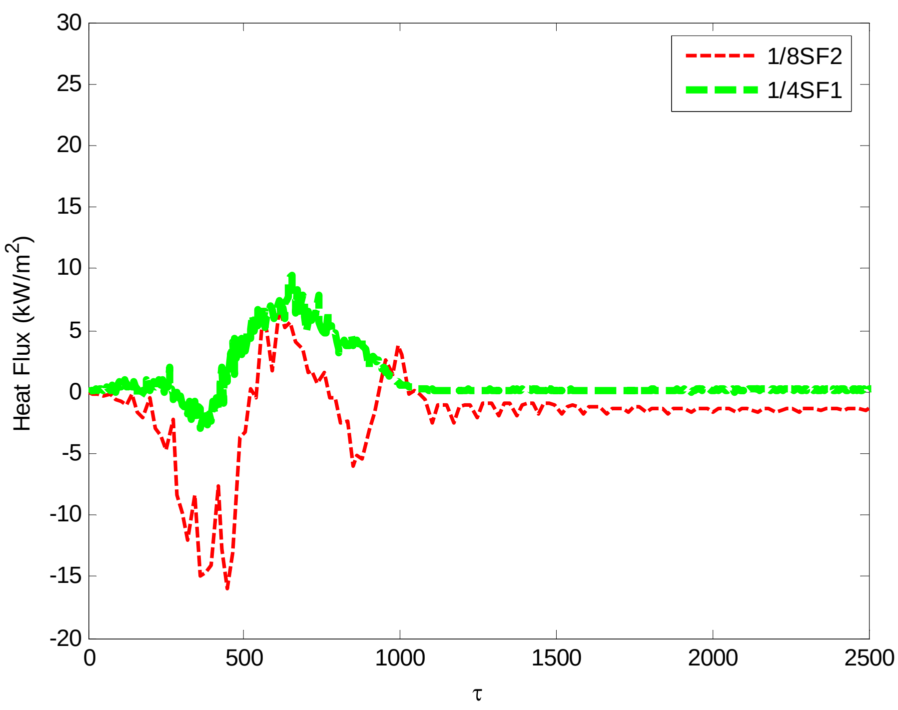

Figure 5.42: Small Fire – (0.44D, 0, 0.65H) Scaled Convection to Wall

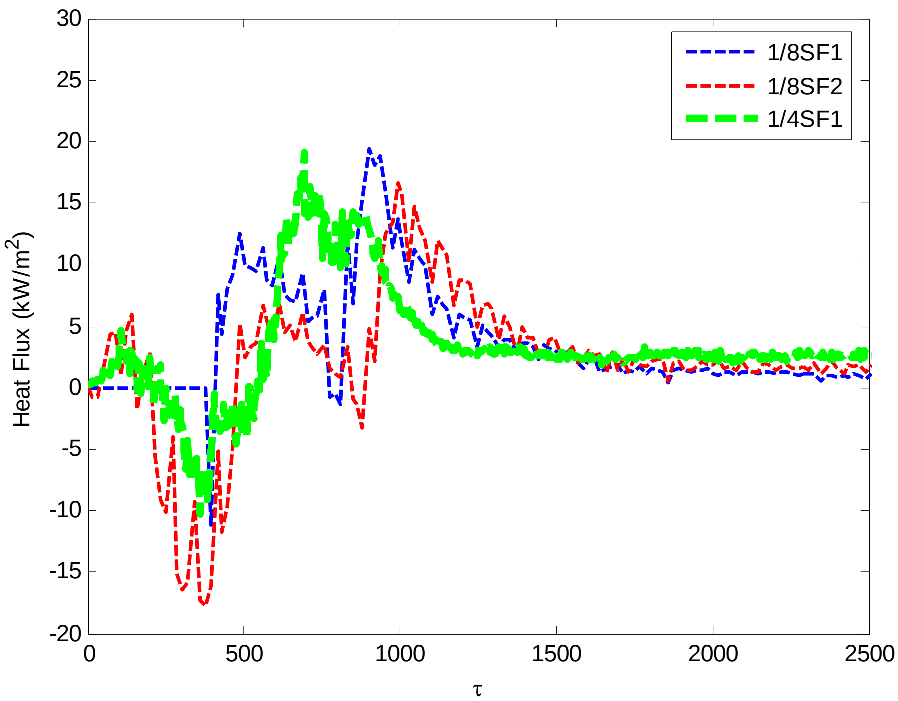

Figure 5.43: Small Fire – (0.44D, 0.37W, H) Scaled Radiation to Wall

As with radiation to the walls, convection to the walls scales well between the 1/8 and 1/4 small fires.

5.3.5 Conduction / Total Heat Flux to Wall

Conduction through the compartment walls scales to the half power. Conduction can be alternatively expressed as the sum of the net radiation and convection to the compartment walls:

$$\dot{q}''_{w,k} = \dot{q}''_{w,r} + \dot{q}''_{w,c} \tag{5.11}$$

Wall conduction data for each fire has been scaled using the expression, $\dot{q}''_{scaled} = \dfrac{\dot{q}''_{w,k}}{l^{1/2}}$, where l is the compartment height. Fig. 5.45 to Fig. 5.47 below plots the results of the scaled conduction for each of the small fires.

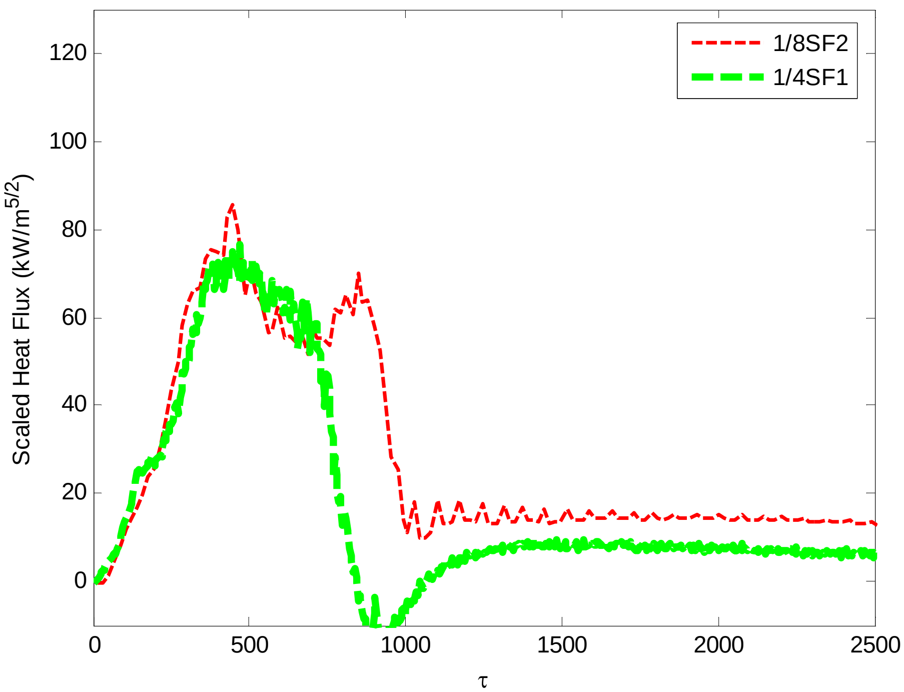

Figure 5.44: Small Fire – (0.44D, 0, 0.65H) Scaled Total Heat Flux to Wall

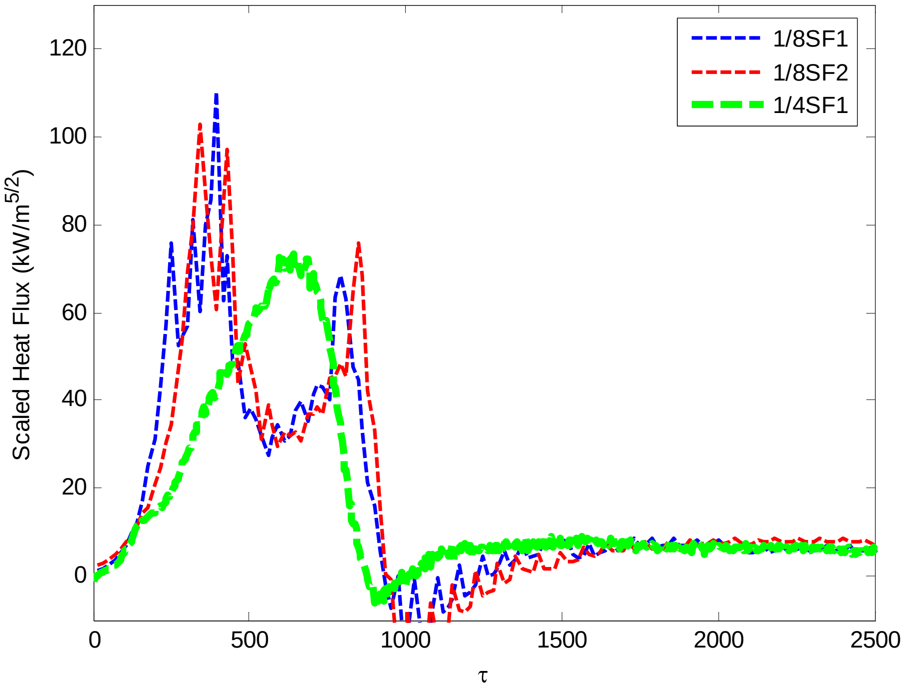

Figure 5.45: Small Fire – (0, 0.55W, 0.2H) Scaled Total Heat Flux to Wall

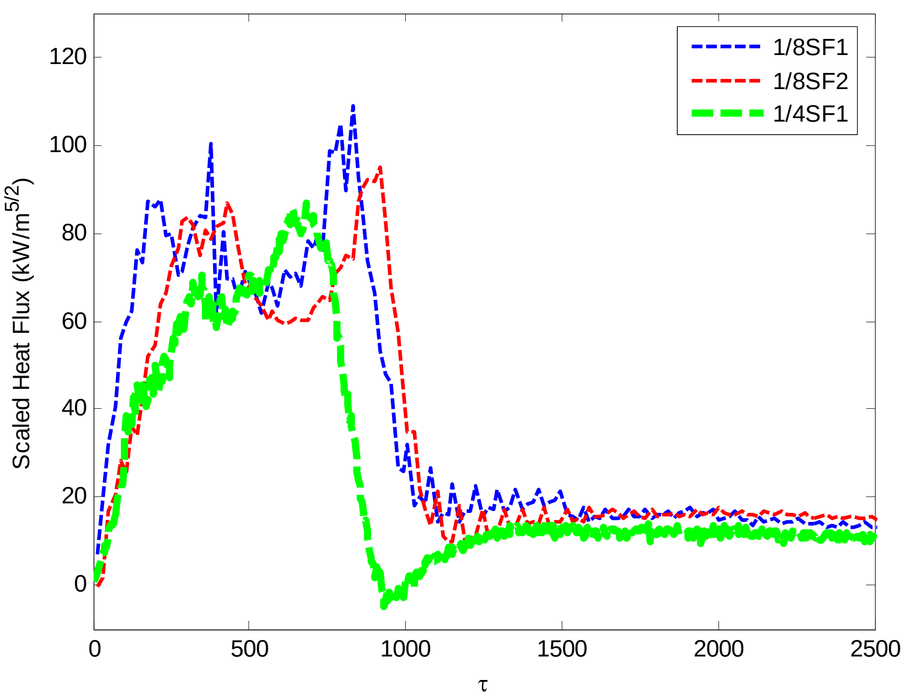

Figure 5.46: Small Fire – (0.44D, 0.37W, H) Scaled Total Heat Flux to Wall

Conduction scales similar to radiation between the 1/8 and 1/4 scale compartment fires. This is mainly due to the much higher radiation flux than convection in the compartments. It can be seen from the plots above that wall conduction scales well.

5.4 Analysis of Convective Heat Transfer Coefficient Data

In section 3.1 Tanaka and Yamada's [12] correlation for the convective heat transfer coefficient with the dimensionless fire power was presented:

$$\frac{h_c}{\rho_\infty c_p (gl)^{1/2}} = \begin{cases} 2.0\times10^{-3} & Q^* \le 4.0\times10^{-3} \\ 0.08 Q^{*2/3} & Q^* > 4.0\times10^{-3} \end{cases} \tag{5.12}$$

Zukoski and Kubota [17] derived an alternate correlation for the convective heat transfer coefficient with the dimensionless fire power:

$$h_c = \rho_\infty c_p (gl)^{1/2} Q^{*1/3}\, r \tag{5.13}$$

The parameter *r* corresponds to the sensor location. It is clear from these two correlations that convective heat transfer coefficient is dependent on the burning rate within the compartment; the precise relationship though was unresolved. The rationale behind such a correlation is that the fire plume generates the velocities within the compartment which in turn drives the convection to the walls.

The experiments conducted previously were for small pool fires or under very controlled conditions which allowed accurate analysis and manipulation of the energy equations to arrive at the above correlations. The fires constructed in this study were ventilation limited. This caused difficulties in deriving a burning rate which could be used to correlate against the convective coefficient data. Another issue with the burning rate correlation would be in understanding the after extinction convective heat transfer coefficient since $Q^* = 0$.

An alternate method of correlating convective heat transfer coefficient is against temperature rise within the compartment. Since temperature differences essentially drive the flows within and into the compartment it could be viewed as being a more fundamental correlation than a correlation with the burning rate done in previous work, furthermore $Q^* \sim \Delta T$.

The temperature correlations have been conducted for both the before extinction and after extinction cases of the compartment fires. Fig. 5.48 and Fig. 5.49 below plot the before extinction convective heat transfer coefficient against temperature difference for the small and large 1/4 scale fire respectively. Fig. 5.50 to Fig. 5.52 plot the after extinction case for the small 1/8, 1/4 and large 1/4 scale fires respectively.

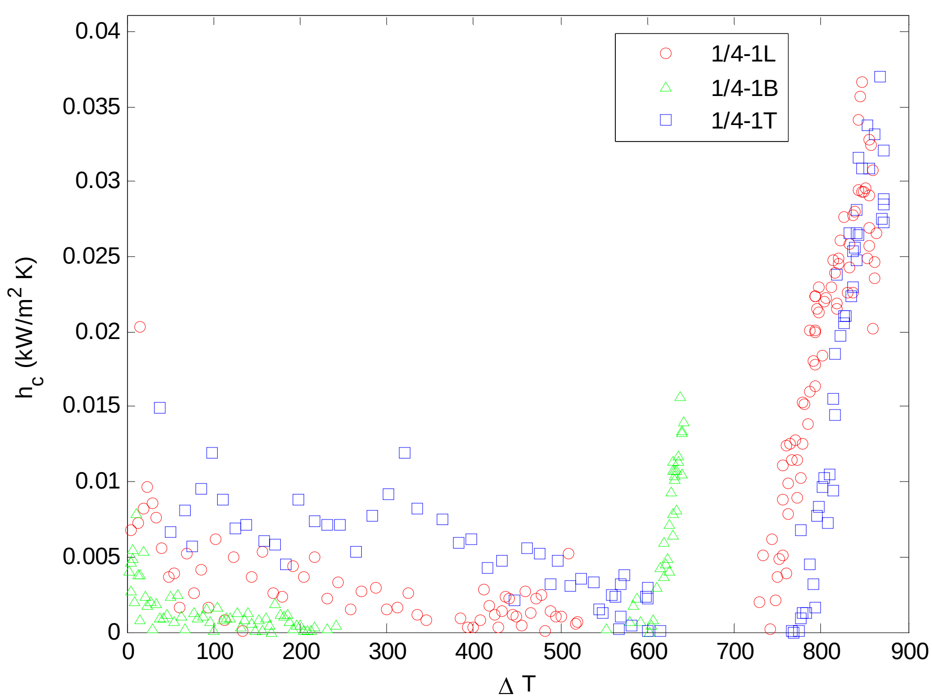

Figure 5.47: 1/4 Scale Small Fire – Convective Heat Transfer Coefficient Before Extinction

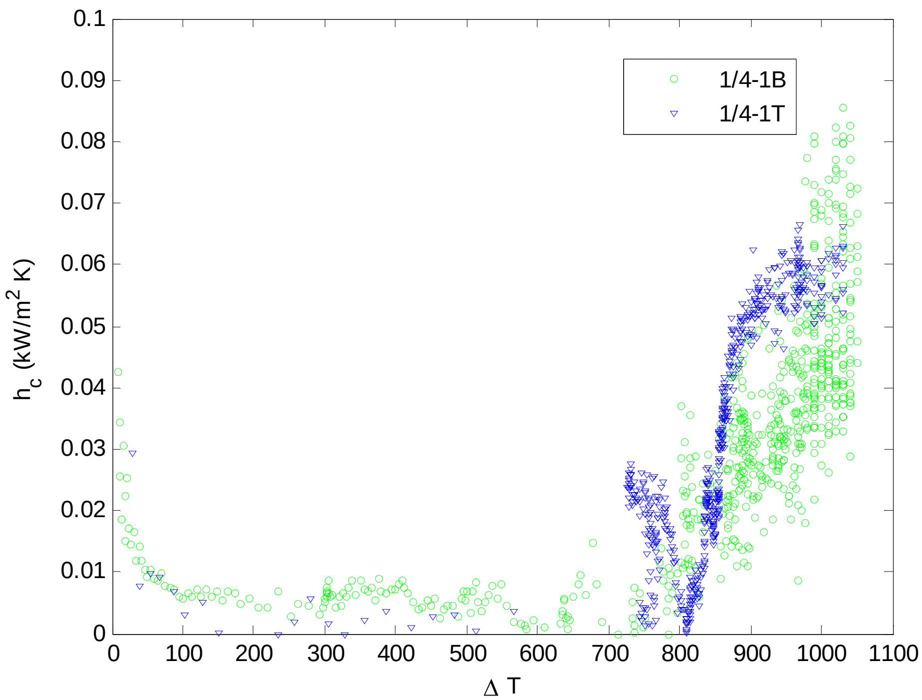

Figure 5.48: 1/4 Scale Large Fire – Convective Heat Transfer Coefficient Before Extinction

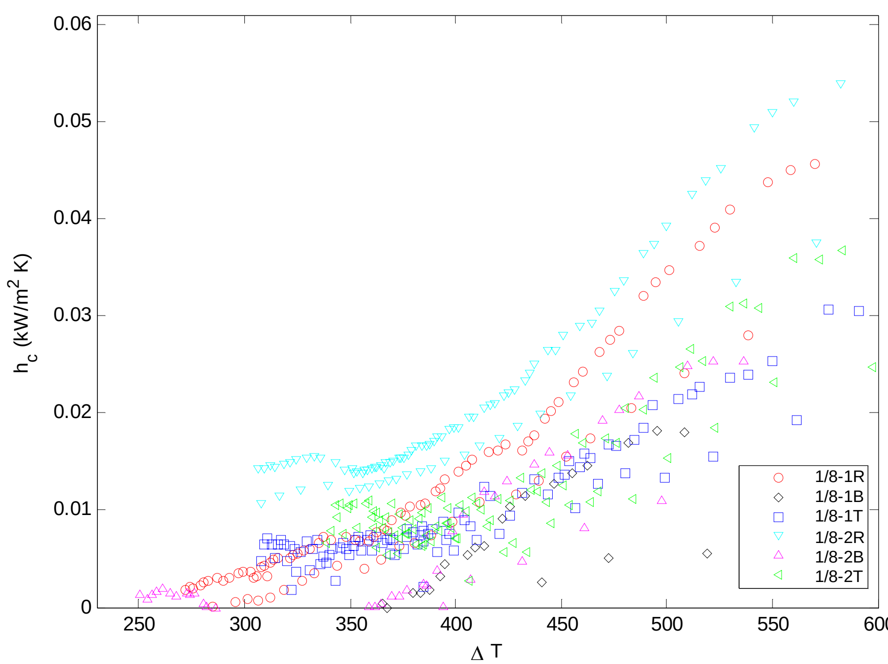

Figure 5.49: 1/8 Scale Small Fire – Convective Heat Transfer Coefficient After Extinction

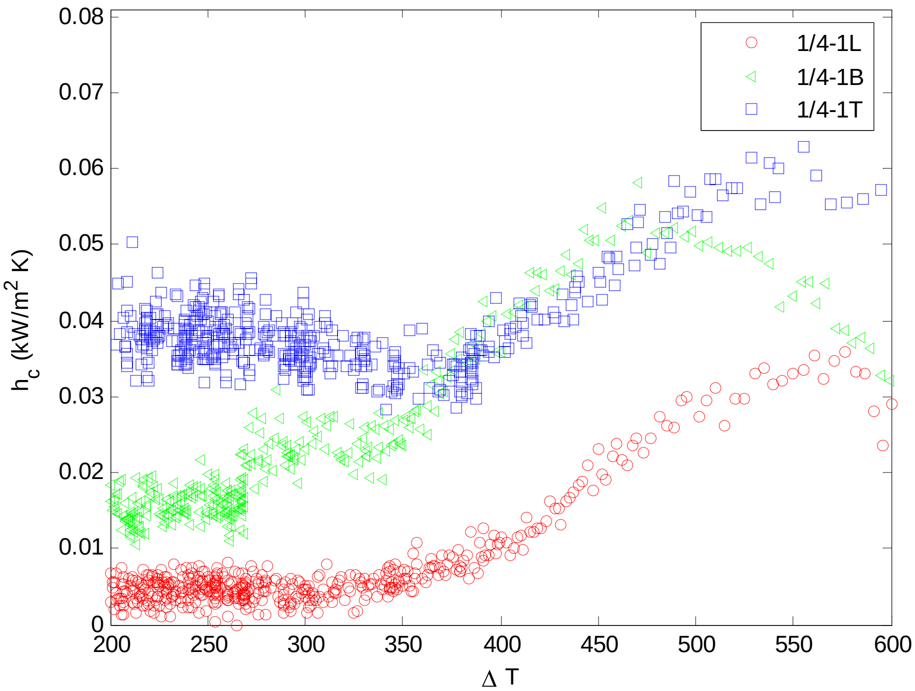

Figure 5.50: 1/4 Scale Small Fire – Convective Heat Transfer Coefficient After Extinction

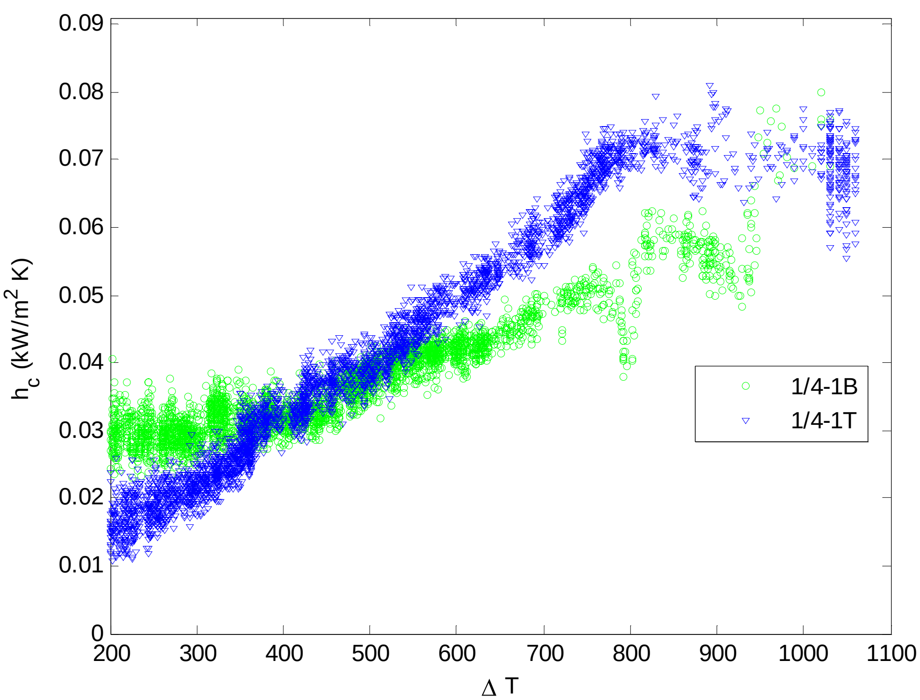

Figure 5.51: 1/4 Scale Large Fire – Convective Heat Transfer Coefficient After Extinction

Fig. 5.53 and Fig. 5.54 below plot the dimensionless convective heat transfer coefficient against dimensionless temperature for all the fires before and after extinction. Dimensionless convective heat transfer coefficient is calculated as:

$$h^* = \frac{h_c}{\rho_\infty c_p (gl)^{1/2}} \tag{5.14}$$

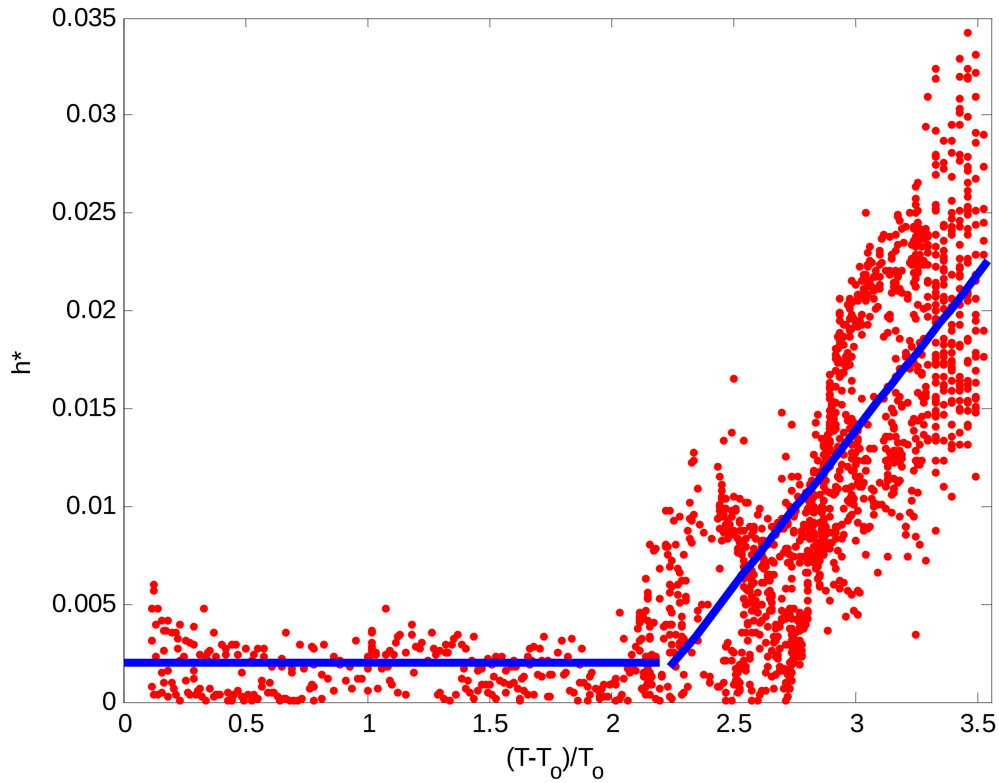

Figure 5.52: Dimensionless Convective Heat Transfer Coefficient Correlation with Temperature Rise – Before Extinction

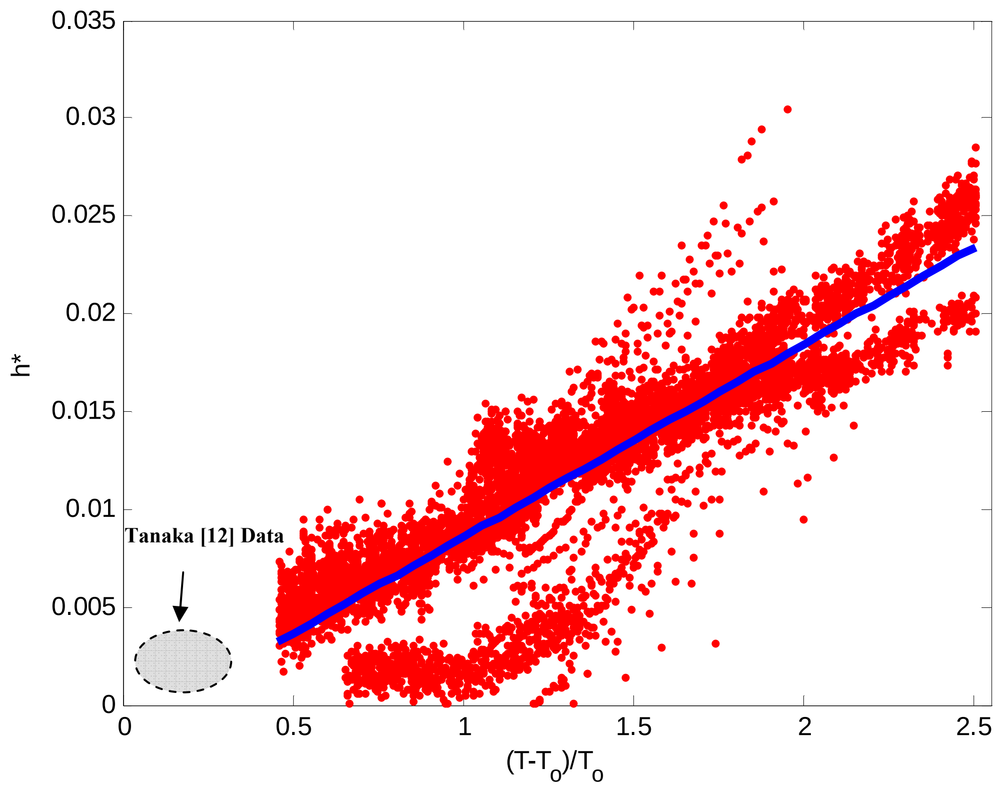

Figure 5.53: Dimensionless Convective Heat Transfer Coefficient Correlation with Temperature Rise – After Extinction

In the above plots it can be clearly seen that convective heat transfer coefficient correlates well with temperature. Data from Tanaka and Yamada [12] is very limited due to the temperature range within which their experiments were conducted, as illustrated in Fig. 5.53. Best fit lines through the data points are then used to give the correlations for the before and after extinction convective heat transfer coefficient data. For the before extinction case the convective coefficient is constant during the low temperature stages of the fires after which it follows a positively sloped linear relationship with temperature. This positively sloped linear temperature relation is also seen in the after extinction case.

The correlation for the before extinction case is:

$$\frac{h_c}{\rho_\infty c_p (gl)^{1/2}} = \begin{cases} 2.03\times 10^{-3} & \dfrac{\Delta T}{T_\infty} < 2 \\ 16.00\times 10^{-3}\dfrac{\Delta T}{T_\infty} & \dfrac{\Delta T}{T_\infty} \geq 2 \end{cases} \tag{5.15}$$

For the after extinction case the correlation is:

$$\frac{h_c}{\rho_\infty c_p (gl)^{1/2}} = 9.87\times 10^{-3}\frac{\Delta T}{T_\infty} \tag{5.16}$$

6. CONCLUSION

The objective laid out for this study was to investigate the scaling of convection and radiation within compartment fires utilizing a novel scaling methodology introduced by Quintiere [4] and Perricone [3].

An outline of the results obtained by Perricone [3] was present from which a number of conclusions can be drawn. Firstly, Perricone [3] demonstrated that compartment temperature, mass loss rate and species concentrations have been successfully scaled. Secondly, it has also been demonstrated that wood crib fires provide highly repeatable test conditions. There are on occasion slight variations between identical repeat tests which can be accounted for by the inconsistent ignition of the wood crib.

A novel metal plate sensor was designed in order to measure and differentiate convection and radiation heat flux within the compartment fires. These sensors were placed in homologous locations between scales to measure the upper layer, lower layer and ceiling heat flux. The metal plate sensors were then shown to have successfully differentiated convection and radiation heat flux in the compartment fires. The metal plate sensors were also successful in obtaining convective heat transfer coefficient data.

Analyzing the scaled data from the 1/8 and 1/4 scale experiments presented a number of conclusions about the scaling methodology used. Firstly, gas temperature scaling results for the small and large fires were generally well scaled. There was, though, a notable difference in the peak temperatures measured between the scaled 1/8 and 1/4 wall and gas temperature data. Secondly, radiation heat flux to the compartment walls was shown to scale using the optically thick emissivity criteria. Finally, convection heat flux to the compartment walls was demonstrated to scale with advected enthalpy.

Finally, a new correlation for the convective heat transfer coefficient in compartment fires was presented. The convective heat transfer coefficient was shown to correlate with the temperature rise within the compartment for both the before and after extinction cases.

REFERENCES

1. Alpert, R. L., *Pressure Modeling of Transient Crib Fire,* Combustion Science and Technology, 1977. **15** (1-2), p. 11-20.

2. Gross, A. F., Robertson, D., *Experimental Fires in Enclosure,* Combustion Institute-Symposium on Combustion, 1965. p. 931-942.

3. Perricone, J., *Scale Modeling of the Transient Behavior of Wood Crib Fires in Enclosures*, Masters Thesis, University of Maryland, 2005

4. Quintiere, J. G., *Fundamentals of Fire Phenomena*, Wiley, 2006

5. Incropera, F. P., DeWitt, D. P., *Fundamentals of Heat and Mass Transfer*, Fourth Edition, Wiley, 1996

6. White, F. M., *Heat and Mass Transfer*, Addison-Wesley Series in Mechanical Engineering, 1988

7. Quintiere, J. G., *Engineering Guide to Fire Exposures to Structural Elements*, Ballot Draft, Society of Fire Protection Engineers, 2003

8. Gross, D., *Experiments on the Burning of Cross Piles of Wood*, Journal of Research, National Bureau of Standards –C, Engineering and Instrumentation, 1962, 66C (2), p. 99-105

9. Block, J., *A Theoretical and Experimental Study of Non-Propagating Free-Burning Fires*, Thirteenth Symposium (International) on Combustion, 1971. Pittsburgh, Pennsylvania

10. Heskestad, G., *Modeling of Enclosure Fires.* Journal of Fire and Flammability, 1975. 6 (3): p. 253-273

11. Croce, P. A., *Modeling of Vented Enclosure Fires Part I. Quasi-Steady Wood-Crib Source Fire*. 1978, Factory Mutual Research Corporation: Norwood, Massachusetts

12. Tanaka, T., Yamada, S., *Reduced Scale Experiments for Convective Heat Transfer in the Early Stages of Fire*, Int. J. Eng. Performance-Based Fire Codes, 1999, **1**(3), 196-203

13. Tofilo, P., Delichatsios, M. A., Silcock, G. W. H., *Effective of Fuel Sootiness on the Heat Fluxes to the Walls in Enclosure Fires*, 8th International Symposium on Fire Safety Science, 2005

14. Harmathy, T. Z., *A New Look at Compartment Fires, Parts I and II.* Fire Technology, 1972. **8** (196)

15. Gross, A. F. and Robertson, D., *Fire Load, Fire Severity and Fire Endurance*. 1970, American Society for Testing and Materials. p. 3-29

16. Harmathy, T. Z., *Properties of Building Materials at Elevated Temperatures*. 1983, National Research Council of Canada, Division of Building Research: Ottawa, Canada.1970, Ministry of Technology and Fire Offices' Committee Joint Fire Research Organization: Borehamwood, England

17. Zukoski, E. E., Kubota, T., *An Experimental Investigation of the Heat Transfer from a Buoyant Gas Plume to a Horizontal Ceiling – Part 2 Effects of Ceiling Layer*, National Bureau of Standards (U.S.), NBS-GCR-77-98, 1975